Magnetohydrodynamic stability analysis of non-axisymmetric tokamak plasmas using the linear visco-resistive stability code CASTOR3D

Jonas Puchmayr

München 2023

Magnetohydrodynamic stability analysis of non-axisymmetric tokamak plasmas using the linear visco-resistive stability code CASTOR3D

Jonas Puchmayr

Dissertation
an der Fakultät für Physik
der Ludwig-Maximilians-Universität
München

vorgelegt von
Jonas Puchmayr
aus Heilbronn

München, den 20.12.2023

Erstgutachter: Prof. Dr. Hartmut Zohm
Zweitgutachter: Prof. Dr. Chris Hegna
Tag der mündlichen Prüfung: 08.02.2024

Contents

Zusammenfassung

In Tokamak Plasmen im Regime hohen Einschlusses (H-Mode) ist der erreichbare Druckgradient typischerweise durch das Auftreten von sogenannten "Edge Localized Modes" (ELMs), welche den explosionsartigen quasi-periodischen Ausstoß von Energie und Teilchen beschreiben, begrenzt. Da ELMs voraussichtlich erheblichen Schaden an den Wandkomponenten von zukünftigen Fusionsanlagen anrichten, ist es von großer Wichtigkeit die Methoden zur Abschwächung und Unterdrückung von ELMs zu verstehen. Experimentelle Beobachtungen haben gezeigt, dass ELMs durch das Anlegen eines nicht-axialsymmetrischen (3D) magnetischen Störfelds (MP Feld) unterdrückt werden können. Die Entstehung von ELMs wird typischerweise gut durch das Anwachsen randlokalisierter magnetohydrodynamischer (MHD) Instabilitäten beschrieben. Dies schafft den Rahmen für die Vorhersage der Stabilität gegenüber ELMs. Bisherige Arbeiten haben die MHD-Stabilität im Grenzbereich lokaler Instabilitäten oder kleiner MP Felder untersucht. In dieser Arbeit wird der lineare Stabilitätscode CASTOR3D, der keine dieser Einschränkungen hat, verwendet, um den Einfluss von MP Feldern auf die MHD-Stabilität zu untersuchen.

Zu diesem Zweck wird das CASTOR3D Framework für die Stabilitätsanalyse von randlokalisierten Instabilitäten optimiert. Die Menge der Fourier-Harmonischen, welche zur Beschreibung der randlokalisierten Moden nötig ist, wird reduziert. Dies ermöglicht die Untersuchung von Instabilitäten mit mittlerer bis hoher toroidaler Modenzahl mit CASTOR3D. Zudem wird die Berechnung von hochaufgelösten Gleichgewichtsgrößen und Koordinatentransformationen durch verbesserte Parallelisierung und die Verwendung schneller Fouriertransformationen ermöglicht. Weiterhin wird die intuitive Energiezerlegung für ideale MHD-Instabilitäten auf resistive Moden erweitert und die physikalischen und phasengemittelten Energieterme werden in den CASTOR3D Code implementiert. Die optimierte Version von CASTOR3D wird dann zur Untersuchung verschiedener Effekte, welche durch die MP Felder ausgelöst werden, verwendet. Diese Effekte beinhalten die helikale Modenlokalisierung, das Festsetzen von Moden an bestimmte Positionen in rotierenden Plasmen ("Mode Locking") und die Destabilisierung durch MP Felder.

Zwei unterschiedliche Arten von Modenlokalisierung oder Mode Locking werden eingeführt: Striktes Locking und Quasi-locking von Instabilitäten. Strikt gelockte Moden werden durch nicht-entartete Eigenwertpaare beschrieben und ihre Position ist unabhängig von der beliebigen Phase der linearen MHD-Lösung. Quasi-gelockte Moden werden durch entartete Eigenwerte beschrieben und weisen, in Abhängigkeit von der Lösungsphase, eine beliebige Position unter einer Einhüllenden auf. Die schnell wachsenden strikt gelockten Moden oder die Einhüllende der quasi-gelockten Moden sind helikal in energetisch vorteilhaften Regionen lokalisiert, während die langsam wachsenden strikt gelockten Moden in energetisch unvorteilhaften Regionen lokalisiert sind. In rotierenden Plasmen rotieren strikt gelockte Moden erst oberhalb einer kritischen Rotationsgeschwindigkeit des Plasmas, wohingegen quasi-gelockte Moden bei jeglicher Plasmarotation nahezu gleichförmig unterhalb ihrer Einhüllenden durchrotieren. Ein Vergleich der von der linearen MHD vorhergesagten Lokalisierung mit experimentellen Messungen zeigt exzellente Übereinstimmung.

Es wird erstmals gezeigt, dass die lineare MHD-Stabilitätsanalyse eine Reduzierung des kritischen Drucks in der Plasmarandregion aufgrund von MP Feldern vorhergesagt. Die vorhergesagte Destabilisierung stimmt gut mit experimentellen Beobachtungen überein. Erstmals werden gekoppelte Ballooning Moden hoher Modenzahl in realistischen magnetisch gestörten Tokamak Plasmen beschrieben. Wie im axialsymmetrischen Fall, werden die Instabilitäten hoher Modenzahl stark durch ionen-diamagnetische Drifteffekte stabilisiert. Zudem wird gezeigt, dass sich eine vereinfachte Erklärung für die Destabilisierung durch MP Felder aus der Lokalisierung der Moden in energetisch vorteilhaften Regionen im 3D Plasma ergibt.

Abstract

The achievable pressure gradient in the edge region of H-mode (high confinement mode) tokamak plasmas is typically limited by the occurrence of type-I Edge Localized Modes (ELMs), which are large quasi-periodic bursts of particles and energy. Since these bursts are projected to cause substantial damage to the plasma-facing components of future fusion devices, it is important to understand methods which are able to mitigate or suppress them. Experimental observations have shown that ELMs can be mitigated or suppressed by the application of external non-axisymmetric (3D) magnetic perturbation (MP) fields. The onset of ELMs is typically well-described by the growth of edge localized magnetohydrodynamic (MHD) instabilities, providing a framework for the predictive stability analysis. While previous work studied MHD stability of 3D tokamak plasmas in the limits of local instabilities or small MP fields, in this thesis the linear MHD stability code CASTOR3D, which has none of these limitations, is used to study the impact of MP fields on MHD stability.

For this purpose, the CASTOR3D framework is optimized for the stability analysis of edge localized instabilities. The set of Fourier harmonics required to describe edge localized instabilities is reduced, enabling the study of instabilities of intermediate to high toroidal mode numbers n. Furthermore, improvements to the parallelization and the implementation of Fast Fourier Transforms enable the calculation of high-resolution equilibrium quantities and coordinate transformations. In addition, the intuitive energetic decomposition of ideal MHD modes is extended to resistive plasma perturbations and the physical and phase-averaged energy terms are implemented into the CASTOR3D code. The optimized CASTOR3D code is applied to study the effect of MP fields on MHD stability, investigating several phenomena such as the helical localization of modes, the locking of modes to a certain position in rotating plasmas or the destabilization due to MP fields.

Two distinct types of mode localization or mode locking are introduced: strict locking and quasi-locking of instabilities. Strictly locked modes correspond to pairs of non-degenerate eigenvalues and there is no change in their position for any value of the arbitrary phase of the linear MHD solution. Quasi-locked modes correspond to degenerate eigenvalues and their precise localization varies beneath an envelope depending on the solution phase. The fast growing strictly locked modes or the envelope of quasi-locked modes are helically localized in an energetically favourable region, while slow growing strictly locked modes are localized in an energetically unfavourable region. Furthermore, in rotating plasmas, strictly locked modes are only rotating if the plasma rotation exceeds a critical threshold whereas quasi-locked modes start rotating beneath their envelope in a nearly uniform motion at any finite value of the plasma rotation. The localization predicted by linear MHD is compared to experimental measurements, showing excellent agreement between the measured and predicted localization.

It is shown for the first time that linear MHD predicts a decrease of the critical pedestal top pressure due to the application of MP fields. The predicted destabilization is in good agreement with experimental observations. For the first time, coupled high-n ballooning modes are described by linear MHD in realistic magnetically perturbed tokamak plasmas. Similar to the axisymmetric case, these high-n instabilities are shown to be strongly stabilized by ion diamagnetic drift effects. Furthermore, it is demonstrated that the localization of the MHD instabilities in energetically favourable regions of the non-axisymmetric tokamak plasma yields a simplified explanation of the destabilization due to MPs.

1 Introduction

The global energy demand is projected to increase over the next decades [1]. In addition, the contributions of greenhouse gas emitting energy sources to the energy mix must be gradually replaced by clean energy sources over the next decades, in order to counteract man-made climate change and keep global warming below 2 °C [2]. Currently, fossil fuels cover about 80% of the global primary energy consumption [3]. One solution to reach these goals would be to replace fossil fuels mainly by solar, wind and nuclear fission power. However, the process of nuclear fission bears the risk of catastrophic uncontrolled chain-reactions and creates long-living radioactive waste that has to be stored safely for tens of thousands of years, motivating research which enables other reliable sources of affordable clean energy. One candidate for a future clean energy source is nuclear fusion, which is the process providing energy to the stars in our universe.

1.1 Nuclear fusion

The dominant fusion process in stars similar to our sun is the proton-proton reaction, where hydrogen fuses to helium at high temperatures and densities. The proton-proton reaction has an extremely small reaction rate, since it involves the weak interaction, which ensures that stars burn for billions of years [4]. However, because of the low reaction rate, the proton-proton reaction is not self-sustained for temperatures and densities achievable in a reactor on Earth. For this reason, fusion reactors have to utilize other fusion processes with higher reaction rates such as the fusion of deuterium and tritium [5]

$$ {}^{2}_{1}\mathrm{D} + {}^{3}_{1}\mathrm{T} \rightarrow {}^{4}_{2}\mathrm{He}\ (3.5\mathrm{MeV}) + {}^{1}_{0}\mathrm{n}\ (14.1\mathrm{MeV}) \tag{1.1} $$

which has the highest reaction rate at reasonable temperatures that is about 24 orders of magnitude larger than the reaction rate of the proton-proton reaction [6]. In order to be self-sustained, the power gained from the fusion process P_α must exceed the energy losses P_{loss} of the system. Assuming an equal mixture of deuterium and tritium, the condition $P_\alpha \geqslant P_{\mathrm{loss}}$ results in the ignition threshold for the "triple product" [5]:

$$ n_e T \tau_E \geqslant L(T) \qquad \text{with} \qquad L(T) = \frac{12 T^2}{E_\alpha \, \overline{\sigma v}(T)} \tag{1.2} $$

where n_e is the electron density, T is the temperature, τ_E is the energy confinement time, which describes the timescale on which energy leaves the system, and $L(T)$ is the ignition threshold, above which the fusion process is self-sustained. The ignition threshold depends on the energy created from the fusion process which remains in the system $E_\alpha = 3.5$ MeV as well as the temperature-dependent reaction rate $\overline{\sigma v}(T)$ of the deuterium-tritium reaction. The remaining 14.1 MeV are carried out of the fusion domain by the neutron. The primary energy outcome is high-grade heat which can be used for electricity production. The ignition threshold for the deuterium-tritium reaction has a minimum of $L \approx 5 \cdot 10^{21}$ keV s m^{-3} at a temperature of $T \approx 15$ keV [7]. For this reason, in order to achieve a self-sustained fusion reaction, the deuterium-tritium mixture must be confined at temperatures of about 15 keV. At these temperatures both hydrogen isotopes are fully ionized, forming a plasma, i.e. a gas of charged particles. Since charged particles gyrate around magnetic field lines, the plasma can be confined using magnetic fields, which is the fundamental concept of Magnetic confinement fusion (MCF). For typical densities in a MCF reactor of $n_e \approx 10^{20}\mathrm{m}^{-3}$, the "triple product" yields a requirement on the energy confinement time $\tau_E \sim$ s [5].

1.2 Tokamaks

Over the last decades, the "triple product" of MCF devices improved by orders of magnitude, gradually approaching the ignition threshold [8]. There are two prevailing MCF reactor concepts, tokamaks and stellarators, both featuring a toroidal field line topology, which means that the magnetic field lines are embedded in torus-shaped flux surfaces. Stellarators are characterized by their winding three-dimensional flux surface geometry and generate the confining magnetic field only by external coils. In contrast, tokamaks, which are the subject of this thesis, are typically axisymmetric by design and generate the poloidal component of the magnetic field by inducing a toroidal current in the plasma.

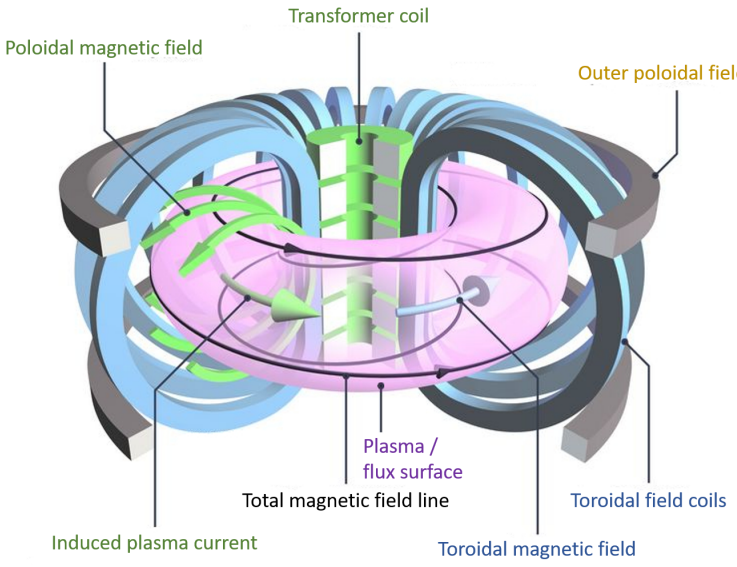

Figure 1.1: Structure of a tokamak device. *Source: EUROfusion (adapted).*

The structure of a tokamak device is shown in figure 1.1. The toroidal field is generated by the toroidal field coils. However, in a purely toroidal field the curvature and the gradient of the magnetic field $\boldsymbol{B}$ would result in a drift motion $\boldsymbol{v_D} \sim \boldsymbol{B} \times \boldsymbol{\nabla} B / q_{\mathrm{el}}$ of the gyrating particles, where q_{el} is the electric charge of the particle [5]. Since the direction of the drift is given by the sign of the charge, this drift motion leads to a separation of positive and negative charges, generating an electric field $\boldsymbol{E}$. The electric field results in a subsequent drift motion $\boldsymbol{v_D} \sim \boldsymbol{E} \times \boldsymbol{B}$, which is independent of the charge of the particles and causes the particles to leave the confined plasma volume [5]. In order to reduce this particle loss, a transformer coil in the center of the tokamak device induces a toroidal plasma current which generates a poloidal magnetic field. The superposition of the toroidal and poloidal magnetic fields results in helical field lines, which are embedded in nested torus-shaped flux surfaces [9]. The helicity of the field lines leads to a cancellation of the $\boldsymbol{\nabla} B$-drift motion if a charged particle traversed once around the torus poloidally [9]. The remaining effect of the drift motion results in a small displacement of the drift orbits [9]. The twisting of the magnetic field for each flux surface is described by the safety factor q, defined as the number of toroidal turns per poloidal turn of a field line. Besides the toroidal field coils and the transformer coil, there are usually multiple poloidal field coils. These coils generate vertical magnetic fields used to position the plasma and modify the shape of the flux surfaces [5].

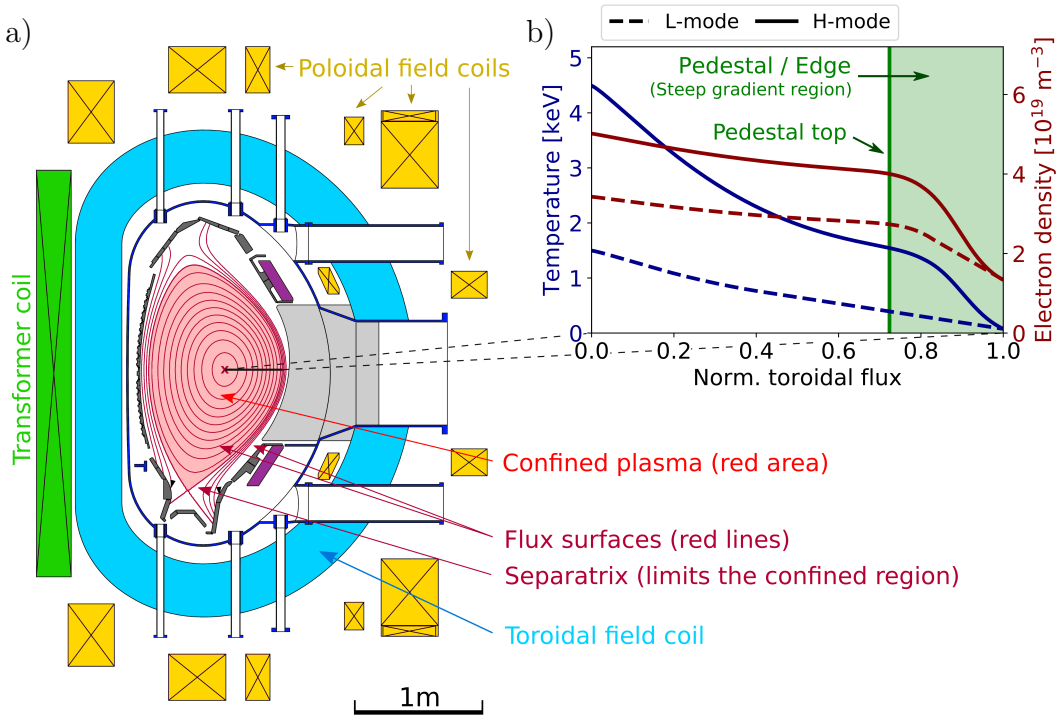

Figure 1.2: a) Toroidal cut of ASDEX Upgrade including the transformer, toroidal and poloidal field coils and a plasma cross-section. Flux surfaces embedding the magnetic field lines are shown in dark red. b) Profiles of density and temperature for two different confinement regimes (L- and H-mode). *Source: Cut of ASDEX Upgrade taken from the ASDEX Upgrade database (adapted).*

The toroidal cut, i.e. the cross-section at a fixed toroidal angle, of the ASDEX Upgrade (AUG) tokamak, located at the Max Planck Institute for Plasma Physics in Garching, is shown in figure 1.2a. In the confined plasma region (red area), flux surfaces (red lines) form closed contours. For this reason, the magnetic field lines of the confined region have no contact to wall components of the device. Outside the confined region, flux surfaces and magnetic field lines touch the wall components. This region, called the scrape-off layer, creates a barrier between the wall components of the device and the confined region, which contains the hot fusion plasma. The scrape-off layer is separated from the confined region by the so-called separatrix.

Because of the high temperatures in fusion plasmas, the mean free path of the charged particles parallel to the magnetic field lines usually exceeds the system size by orders of magnitude [10]. This means that particles in the confined region travel around the toroidal direction thousands of times before they are deflected by collisions. The mean free path perpendicular to the field lines is bound by the gyro-radius. The toroidal magnetic field in tokamaks is strong enough that the gyro-radius and, therefore, the perpendicular mean free path are much smaller than the system size. For this reason, gradients of thermodynamic quantities can only be sustained perpendicular to the flux surfaces, which embed the magnetic field lines [11]. The nested flux surfaces can be labeled by the toroidal or poloidal magnetic flux enclosed by those flux surfaces [9]. The poloidal or toroidal flux is defined as the magnetic flux through a toroidal or poloidal surface enclosed by a specific flux surface, which is illustrated in figure 1.3. This allows the thermodynamic quantities to be expressed as profiles of the magnetic flux. Density and temperature profiles of the confined region are shown in figure 1.2b for two different confinement regimes. The normalized

toroidal flux increases from 0 at the magnetic axis (red cross) to 1 at the separatrix. Several other quantities can be expressed as a function of the magnetic flux such as the safety factor q and the toroidal current I.

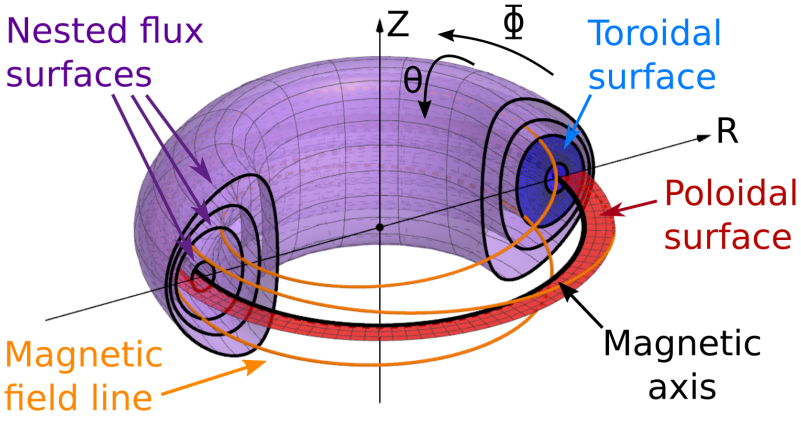

Figure 1.3: Nested flux surfaces (purple) and cylindrical coordinates (R, Φ, Z) for a tokamak plasma. The orange line indicates a magnetic field line. The blue and red surfaces represent a toroidal and poloidal surface corresponding to the flux surface embedding the orange field line. On each flux surface, a local set of angle coordinates (Φ, θ) can be defined, where θ is the poloidal angle.

There are multiple confinement regimes featuring different radial transport behaviour in tokamak plasmas. The most common of these regimes are the low confinement mode (L-mode) and the high confinement mode (H-mode) [12]. The transport properties and thermodynamic gradient lengths in L-mode are nearly constant across the confined region, resulting in peaked but relatively flat density and temperature profiles as shown in figure 1.2b. In order to access the H-mode regime, a certain heating power threshold must be exceeded [12]. Then, a transport barrier forms at the edge of the confined plasma region. This region of self-organized suppression of turbulent transport results in the formation of steep temperature and density gradients. Since the transport in the core plasma is nearly unaffected during the transition from L-mode to H-mode, the gradient length of the temperature profile, $T/\nabla T$, remains roughly unchanged, which is known as profile stiffness [11, 13]. Consequently, the core profiles seem to be lifted up by the steep edge gradients as if they were on a pedestal. For this reason, the steep gradient region at the edge of H-mode tokamak plasmas is called pedestal. The transport barrier at the pedestal of H-mode plasmas leads to an increase of the energy confinement time by about a factor of 2 compared to L-mode, which makes the H-mode a favorable regime for reaching ignition [12].

1.3 Mitigation and suppression of edge localized modes

While the H-mode grants increased energy and particle confinement, the steep gradients in the pedestal of H-mode tokamak plasmas can eventually drive edge localized plasma instabilities [14]. If the gradients in the pedestal exceed a critical threshold, massive quasi-periodic bursts of energy and particles, called type-I Edge Localized Modes (ELMs), are triggered. Each burst, ejecting particles and energy from the confined region, causes a reduction of the gradient below the critical threshold. After a burst, the gradients are slowly restored by transport mechanisms until they once again exceed the critical threshold, triggering the next burst. These bursts limit

the achievable pedestal top pressure and are projected to cause severe damage to the plasma-facing components of future fusion devices such as ITER [15]. For this reason, it is important to understand the conditions at which ELMs are triggered as well as methods which are able to mitigate or suppress ELMs. The onset of type-I ELMs is typically well-described by the growth of edge localized magnetohydrodynamic (MHD) instabilities [16, 17]. This allows for the predictive analysis of ELM stability using MHD, which is a fluid description of the plasma and further discussed in chapter 2.

Experimental observations have shown that ELMs can be mitigated [18, 19] or suppressed [20, 21] by the application of external non-axisymmetric magnetic perturbation (MP) fields. This technique is foreseen for the suppression of ELMs in the ITER tokamak, which is currently under construction in Cadarache, France. In the case of ELM suppression, the plasma enters a stationary state with no ELM bursts [20, 21]. In the case of ELM mitigation, large ELMs are replaced by smaller but more frequent ELM bursts [18, 19], decreasing the peak energy fluence onto the plasma-facing components by an MP-induced reduction of the pedestal top pressure [22].

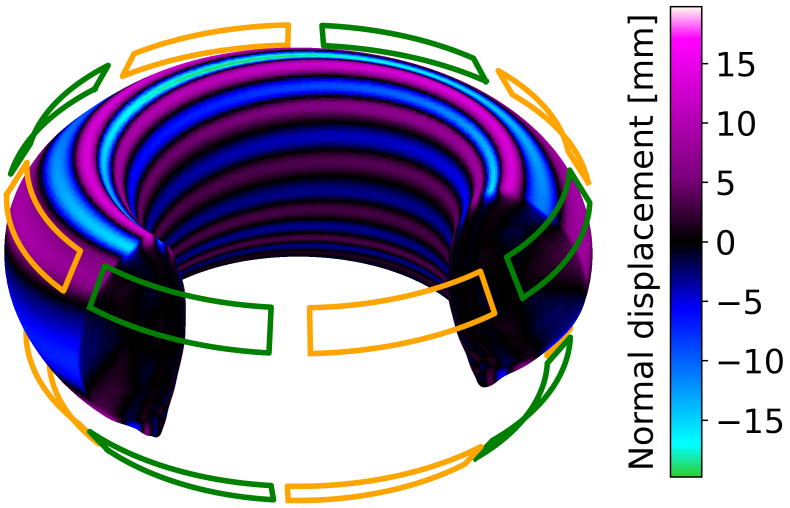

Figure 1.4: Corrugation (normal displacement) of the flux surfaces in the confined plasma volume of an ASDEX Upgrade plasma and the 16 MP coils generating the non-axisymmetric perturbation field.

The application of MP fields intentionally breaks the axisymmetry of the tokamak configuration. The plasma responds to the externally applied MP field by forming non-axisymmetric helically corrugated flux surfaces [23, 24]. Figure 1.4 shows the MP coils, which generate the MP field, as well as the corresponding corrugation of the flux surfaces for an AUG plasma. The corrugation quickly decays towards the magnetic axis as the plasma attempts to shield the externally applied perturbation. It has been demonstrated empirically that the application of MP fields results in augmented transport, causing a decrease of the pedestal density and pressure gradients [21, 25, 26]. Furthermore, evaluating the ELM onset for a range of experiments (discharges) with applied MP fields shows that the perturbation fields lead to a reduction of the MHD stability threshold, meaning the critical pedestal top pressure above which ELMs occur [21, 27]. It is proposed that, in order to achieve ELM suppression, the augmented transport has to keep the pressure gradient below the reduced stability threshold. This highlights the importance of understanding the effect of MP fields on both MHD stability, which is subject of this thesis, and transport for the extrapolation of ELM suppression to future tokamak devices.

1.4 Focus of this thesis

Previous work studied MHD stability of magnetically perturbed tokamak plasmas in the limits of local instabilities or small MP fields [28, 29, 30, 31]. In the frame of this PhD thesis work, the linear MHD code CASTOR3D [32, 33, 34], which has none of these limitations, has been optimized for the analysis of edge localized instabilities in tokamaks. Then, the optimized code was applied to study the effect of symmetry-breaking by MP fields on MHD stability. The theory of MHD, edge localized instabilities and the predictive modelling tools are discussed in chapter 2. Chapter 3 summarizes the extensions and optimizations of the COTRANS and CASTOR3D codes. In chapter 4, an energy decomposition for resistive plasma perturbations is derived, the ideal and resistive terms of the energy decomposition are implemented into the CASTOR3D code and the implemented energy terms are verified for a numerical test case. Results on the helical localization and mode locking of MHD instabilities in non-axisymmetric tokamak plasmas are presented in chapter 5. The numerically predicted localization is in good agreement to experimental measurements. Furthermore, the helical structure of the energetically favourable regions, maximizing the growth rate of MHD instabilities, is revealed. In chapter 6, the numerically predicted reduction of the MHD stability threshold by MP fields is shown. The predicted shift of the marginally stable pedestal top pressure is in good agreement with experimental findings. In the case of an ELM mitigation discharge carried out on ASDEX Upgrade, an increase in the growth rate of MHD instabilities is found. If the pressure gradient is reduced, the MHD instabilities vanish, corresponding to an ELM suppression discharge. Finally, the results of this thesis are summarized in chapter 7.

2 Magnetohydrodynamics (MHD)

The theory of Magnetohydrodynamics (MHD) yields a fluid description of the plasma. Similar to conventional hydrodynamics, the MHD equations are obtained from the moments of the kinetic equation [10]. MHD additionally considers electromagnetic forces between the charged particles. The fluid description is based on the assumption that the mean free path of particles is smaller than the dimensions of a fluid element [35]. In fusion plasmas, this assumption is usually fulfilled perpendicular to the field lines since particles are bound by the gyro-motion. However, the mean free path parallel to the field lines exceeds the system size typically by orders of magnitude. For this reason, MHD can only accurately describe the dynamics perpendicular to the field lines [35].

In principle, MHD provides a separate set of fluid equations for each particle species. If there is mainly one ion species, the equations for electrons and ions can be combined [35]. For this purpose, it is assumed that the electron mass can be neglected and that the plasma is quasi-neutral. Quasi-neutrality means that the ion and electrons densities, n_i and n_e, are approximately equal, such that no macroscopic electric fields are present on scales greater than the Debye length. As a result, the single-fluid MHD equations, obtained from the first two moments of the kinetic equation, read [35, 36, 34]:

$$\text{Continuity} \qquad \partial_t \rho + \boldsymbol{\nabla} \cdot (\rho \boldsymbol{v}) = 0 \tag{2.1}$$

$$\text{Force balance} \qquad \rho(\partial_t + \boldsymbol{v} \cdot \boldsymbol{\nabla})\boldsymbol{v} = -\boldsymbol{\nabla} p - \boldsymbol{\nabla} \cdot \boldsymbol{\Pi} + \boldsymbol{j} \times \boldsymbol{B} \tag{2.2}$$

$$\text{Ohm's law} \qquad \boldsymbol{E} + \boldsymbol{v} \times \boldsymbol{B} = \eta \boldsymbol{j} \tag{2.3}$$

together with the Maxwell equations

$$\partial_t \boldsymbol{B} = -\boldsymbol{\nabla} \times \boldsymbol{E} \ , \qquad \boldsymbol{\nabla} \times \boldsymbol{B} = \mu_0 \boldsymbol{j} \ , \qquad \boldsymbol{\nabla} \cdot \boldsymbol{B} = 0 \tag{2.4}$$

where ρ is the mass density, $\boldsymbol{v}$ is the center-of-mass velocity, p is the isotropic pressure, $\boldsymbol{\Pi}$ is the an-isotropic component of the pressure tensor, j is the current density and η is the resistivity. In addition, a fourth equation, $\boldsymbol{\nabla} \cdot \boldsymbol{j} = 0$, is obtained from the derivation of the single-fluid MHD equations, which is naturally fulfilled by equation 2.4. In equation 2.3, the Hall term and electron diamagnetic drift are neglected. This is justified if the velocity of the observed MHD phenomena is of the order of the ion thermal velocity [35]. Finally, the MHD equations 2.1 to 2.4 must be closed by assumptions on the higher moments of the kinetic equations. Assuming adiabatic processes and neglecting resistive heating, one obtains [37]:

$$(\partial_t + \boldsymbol{v} \cdot \boldsymbol{\nabla})(p \rho^{-\Gamma}) = 0 \tag{2.5}$$

where Γ is the adiabatic coefficient, which is $\Gamma = 5/3$ for a mono-atomic gas. The an-isotropic part of the pressure tensor can be approximately split into a parallel $\boldsymbol{\Pi}_\parallel$ and a cross-component $\boldsymbol{\Pi}_\wedge$, which describe parallel viscosity and gyro-viscosity, respectively [36, 34]:

$$\boldsymbol{\nabla} \cdot \boldsymbol{\Pi}_\parallel \approx \mu_\parallel \Delta_\parallel \boldsymbol{v} \ , \quad \boldsymbol{\nabla} \cdot \boldsymbol{\Pi}_\wedge \approx \rho(\boldsymbol{v}_{\boldsymbol{i}}^* \cdot \boldsymbol{\nabla})\boldsymbol{v} \quad \text{with} \quad \boldsymbol{v}_{\boldsymbol{i}}^* = \frac{m_i}{e} \frac{\alpha_T}{\rho} \frac{\boldsymbol{B} \times \boldsymbol{\nabla} p}{\boldsymbol{B}^2} \tag{2.6}$$

where $\mu_\parallel$ is the parallel viscosity coefficient, $\Delta_\parallel$ is the parallel Laplace operator, $\boldsymbol{v}_{\boldsymbol{i}}^*$ is the ion diamagnetic drift velocity, m_i is the ion mass and e is the elementary charge. Since the ion pressure gradient is not determined by single-fluid MHD, it is replaced by the ratio $\alpha_T \in [0, 1]$ between ion pressure and total pressure. A common choice is to assume equal electron and ion pressure, which means $\alpha_T = 0.5$. However, other ratios of the pressure gradient can be studied by varying α_T.

2.1 Boundary conditions

At the plasma-vacuum interface, several boundary conditions must be satisfied [38]:

$$\left[\!\left[p + \frac{\boldsymbol{B}^2}{2\mu_0} \right]\!\right] = 0 \tag{2.7}$$

$$\boldsymbol{n} \times [\![\boldsymbol{E}]\!] = (\boldsymbol{n} \cdot \boldsymbol{v})[\![\boldsymbol{B}]\!] \tag{2.8}$$

$$\boldsymbol{n} \cdot [\![\boldsymbol{B}]\!] = 0 \ , \ \boldsymbol{n} \times [\![\boldsymbol{B}]\!] = \mu_0 \boldsymbol{K} \tag{2.9}$$

where $\boldsymbol{n}$ is the surface normal vector pointing into the vacuum region, $\boldsymbol{K}$ is a surface current and $[\![\dots]\!]$ denotes the jump of the enclosed quantity across the interface. In the following, surface currents are neglected, since they cannot be sustained in the presence of finite resistivity. In the absence of surface currents $\boldsymbol{K} = 0$, all components of the magnetic and electric field must be continuous across the plasma-vacuum interface. Then, according to the pressure balance 2.7, the pressure must vanish at the boundary.

2.2 MHD equilibrium

In order to study the MHD stability of tokamak plasmas, it is useful to search for stationary solutions of the MHD equations. A stationary state, or MHD equilibrium, is reached if the explicit time-dependence of all fluid quantities vanishes, i.e. $\partial_t \to 0$. Then, the force balance equation 2.2 becomes:

$$\boldsymbol{j} \times \boldsymbol{B} = \boldsymbol{\nabla} p \quad \Rightarrow \quad (\boldsymbol{\nabla} \times \boldsymbol{B}) \times \boldsymbol{B} = \mu_0 \boldsymbol{\nabla} p \tag{2.10}$$

In equation 2.10, it is assumed that the dynamic pressure $\rho(\boldsymbol{v} \cdot \boldsymbol{\nabla})\boldsymbol{v}$ is negligible, which is justified for small Mach numbers [35, 39], and that the equilibrium pressure is isotropic. For axisymmetric systems, the stationary force balance equation can be rewritten in terms of the poloidal fluxes, which results in a scalar partial differential equation, the so-called Grad-Shafranov equation. For this purpose, the MHD equations are expressed in cylindrical coordinates (R, Φ, Z). Then, the Grad-Shafranov reads [35]:

$$4\pi^2 F F' + (2\pi R)^2 \mu_0 p' = 2\pi R \mu_0 j_\Phi = -\Delta^* \psi \quad \text{with} \quad F(\psi) = R B_\Phi \tag{2.11}$$

and the poloidal flux

$$\psi(R, Z) = 2\pi \int_0^R B_Z(R, Z) R \ \mathrm{dR} - 2\pi \int_0^{R_M} B_Z(R, Z_M) R \ \mathrm{dR} \tag{2.12}$$

where B_Φ is the toroidal magnetic field, B_Z is the vertical component of the magnetic field, j_Φ is the toroidal current density, $\Delta^* \equiv R\partial_R(1/R \cdot \partial_R) + \partial_Z^2$ is the Stokes operator in cylindrical coordinates and (R_M, Z_M) is the location of the magnetic axis. The prime denotes a derivative with respect to the poloidal flux. The integration surfaces of the poloidal flux as defined in equation 2.12 as well as the cylindrical coordinates are illustrated in figure 1.3 on page 4.

The stationary force balance can also be obtained from a variational principle based on the energy stored in the plasma [40]:

$$W = \int \frac{\boldsymbol{B}^2}{2\mu_0} + \frac{p}{\Gamma - 1} \ \mathrm{dV} \tag{2.13}$$

where the integral is taken over the plasma volume. Numerical solutions of the force balance for non-axisymmetric systems are found by minimizing the plasma energy 2.13 for given pressure and safety factor profiles and total toroidal flux. The safety factor profile can be replaced by the toroidal current profile. In addition, either the vacuum magnetic field or the shape of the plasma boundary must be specified as boundary conditions.

In order to obtain MHD equilibria of tokamak discharges, they must be reconstructed from experimental measurements. The equilibrium reconstruction code CLISTE [41] determines a solution of the Grad-Shafranov equation which minimizes the least square error with respect to several measurements. These measurements include magnetic data, kinetic profiles and information on the safety factor. The resulting equilibrium reconstruction yields the pressure and safety factor profiles and the shape of the plasma boundary defining the MHD equilibrium which corresponds to the experimental measurements. For this purpose, the source profiles p' and FF' are parameterized and their free parameters are varied during the minimization.

While such an interpretative equilibrium reconstruction results in an MHD equilibrium from magnetic measurements, the resolution and quality of the resulting equilibrium are typically not sufficient to perform a stability analysis. In order to study the MHD stability of an equilibrium obtained from equilibrium reconstruction, the quality of the equilibrium must be increased by further minimizing the residual forces. In addition, the coordinate transformation to coordinate systems which are suitable for stability analysis (see section 2.3.5) requires a high radial resolution. For this reason, high-resolution equilibria must be calculated from the reconstructed pressure and safety factor profiles in order to study the stability of the equilibrium. In this thesis, the NEMEC [40, 42] and GVEC [43] codes, which are based on the minimization of the plasma energy 2.13, are used to calculate the high-quality equilibrium solutions of non-axisymmetric plasmas. The NEMEC code is capable of calculating non-axisymmetric free-boundary equilibria, meaning that the vacuum magnetic field, generated by the coils, can be prescribed. The plasma boundary is then self-consistently determined such that the pressure balance 2.7 is fulfilled. Both codes, GVEC and NEMEC, can calculate fixed-boundary equilibria, for which the shape of the plasma boundary is prescribed. The GVEC code makes use of advanced numerical methods and is based on a Galerkin approach, showing better equilibrium convergence properties compared to NEMEC. In this thesis, NEMEC is used to calculate free-boundary equilibria in order to determine the shape of the plasma boundary if the coil currents are prescribed. This provides the shape of the plasma boundary required for the calculation of fixed-boundary equilibria. The GVEC code is used to calculate refined fixed-boundary equilibria based on the shape of the plasma boundary.

Finally, the use of CLISTE for the reconstruction of non-axisymmetric tokamak equilibria must be discussed. Since the CLISTE code is based on the Grad-Shafranov equation, it is in principle restricted to the reconstruction of axisymmetric equilibria. However, it has been shown that the reconstructed source profiles of non-axisymmetric tokamak plasmas are nearly unaffected by the applied MP fields [44]. Furthermore, there is excellent agreement between the measured corrugation and the corrugation of non-axisymmetric equilibria calculated with the NEMEC code based on profiles obtained from CLISTE [24]. This verifies the corrugation or plasma response to MP fields determined by NEMEC and justifies the use of CLISTE to reconstruct the source profiles of magnetically perturbed tokamak equilibria.

2.3 MHD stability

The stability of an equilibrium is determined by its response to small perturbations. If the plasma tends to amplify the initial perturbation, the equilibrium is considered to be unstable and the perturbation is called an instability. If the equilibrium tends to restore itself, it is considered to be stable. One approach to study the stability of an equilibrium is to add some small random noise and evolve the fluid quantities in time. Typically, numerically calculated equilibria already have a finite force imbalance such that no additional noise is required. While this approach yields the non-linear dynamics of instabilities, its numerical implementation requires high amounts of computing time. A different approach to obtain the response of the plasma to small perturbations is to linearize the MHD equations with respect to the equilibrium solution, which yields information on the initial response of the plasma to a perturbation. This results in an eigenvalue problem, where the spectrum contains all possible instabilities and which usually requires less computing time for its numerical solution.

2.3.1 Linear MHD

In order to linearize the MHD equations, all fluid variables $f = f_0 + f_1$ are split into an equilibrium component f_0, which obeys the stationary MHD equations, and a small perturbation $f_1 \sim \mathcal{O}(\epsilon f_0)$ with $\epsilon \ll 1$. This approach allows terms of second or higher order in the perturbation scale ϵ to be neglected. Since the resulting system of partial differential equations for the perturbed quantities is linear in time, an exponential ansatz for the time-dependence of the perturbations $f_1(\boldsymbol{r}, t) = f_1(\boldsymbol{r})e^{\lambda t}$ is made, where $\lambda = \gamma + i\omega$ contains the growth rate γ and the oscillation frequency ω of the perturbation. Then, the linearization of the MHD equations 2.1 to 2.3 and 2.5 yields [34]:

$$\lambda\rho_1 = -\boldsymbol{v}_0 \cdot \boldsymbol{\nabla}\rho_1 - \boldsymbol{v}_1 \cdot \boldsymbol{\nabla}\rho_0 - \rho_1 \boldsymbol{\nabla} \cdot \boldsymbol{v}_0 - \rho_0 \boldsymbol{\nabla} \cdot \boldsymbol{v}_1 \tag{2.14}$$

$$\begin{aligned}\rho_0\lambda\boldsymbol{v}_1 = &-\rho_1(\boldsymbol{v}_0 \cdot \boldsymbol{\nabla})\boldsymbol{v}_0 - \rho_0(\boldsymbol{v}_1 \cdot \boldsymbol{\nabla})\boldsymbol{v}_0 - \rho_0(\boldsymbol{v}_0 \cdot \boldsymbol{\nabla})\boldsymbol{v}_1 \\ &+ \rho_1(\boldsymbol{v}^*_{\boldsymbol{i},0} \cdot \boldsymbol{\nabla})\boldsymbol{v}_0 + \rho_0(\boldsymbol{v}^*_{\boldsymbol{i},1} \cdot \boldsymbol{\nabla})\boldsymbol{v}_0 + \rho_0(\boldsymbol{v}^*_{\boldsymbol{i},0} \cdot \boldsymbol{\nabla})\boldsymbol{v}_1 \\ &+ (\boldsymbol{\nabla} \times (\boldsymbol{\nabla} \times \boldsymbol{A}_1)) \times \boldsymbol{B}_0/\mu_0 + (\boldsymbol{\nabla} \times \boldsymbol{B}_0) \times (\boldsymbol{\nabla} \times \boldsymbol{A}_1)/\mu_0 \\ &- \boldsymbol{\nabla}(\rho_0 T_1)/m_i - \boldsymbol{\nabla}(\rho_1 T_0)/m_i + \mu_\parallel \Delta_\parallel \boldsymbol{v}_1\end{aligned} \tag{2.15}$$

$$\lambda T_1 = -\boldsymbol{v}_1 \cdot \boldsymbol{\nabla} T_0 - \boldsymbol{v}_0 \cdot \boldsymbol{\nabla} T_1 - (\Gamma - 1) T_1 \boldsymbol{\nabla} \cdot \boldsymbol{v}_0 - (\Gamma - 1) T_0 \boldsymbol{\nabla} \cdot \boldsymbol{v}_1 \tag{2.16}$$

$$\lambda \boldsymbol{A}_1 = \boldsymbol{v}_1 \times \boldsymbol{B}_0 + \boldsymbol{v}_0 \times (\boldsymbol{\nabla} \times \boldsymbol{A}_1) - \eta(\boldsymbol{\nabla} \times (\boldsymbol{\nabla} \times \boldsymbol{A}_1))/\mu_0 \tag{2.17}$$

with

$$\begin{aligned}\boldsymbol{v}^*_{\boldsymbol{i},1} = &-\alpha_T \frac{m_i}{e} \frac{\rho_1}{\rho_0^2} \frac{\boldsymbol{B}_0 \times \boldsymbol{\nabla} p_0}{\boldsymbol{B}_0^2} + \alpha_T \frac{m_i}{e} \frac{1}{\rho_0} \frac{(\boldsymbol{\nabla} \times \boldsymbol{A}_1) \times \boldsymbol{\nabla} p_0}{\boldsymbol{B}_0^2} \\ &+ \alpha_T \frac{m_i}{e} \frac{1}{\rho_0} \frac{\boldsymbol{B}_0 \times (T_0 \boldsymbol{\nabla}\rho_1 + T_1 \boldsymbol{\nabla}\rho_0 + \rho_0 \boldsymbol{\nabla} T_1 + \rho_1 \boldsymbol{\nabla} T_0)}{\boldsymbol{B}_0^2} \\ &- \alpha_T \frac{m_i}{e} \frac{1}{\rho_0} \frac{2\boldsymbol{B}_0 \cdot (\boldsymbol{\nabla} \times \boldsymbol{A}_1)}{\boldsymbol{B}_0^4} (\boldsymbol{B}_0 \times \boldsymbol{\nabla} p_0)\end{aligned} \tag{2.18}$$

where the resistivity η and the parallel viscosity $\mu_\parallel$ are free parameters, which must be determined from kinetic models. In the linearized MHD equations, the magnetic field perturbation is expressed as the curl of a vector potential $\boldsymbol{A}_1$, which implicitly

fulfills $\boldsymbol{\nabla} \cdot \boldsymbol{B}_1 = 0$. Furthermore, the MHD temperature T, defined as the sum of electron and ion temperature, is related to the isotropic pressure by the ideal gas law $p = nT = \rho T/m_i$. The thermodynamic temperatures of the ions T_i and electrons T_e can be derived from the MHD temperature by the relations $T_i = \alpha_T T$ and $T_e = (1 - \alpha_T)T$, where α_T was defined as the ratio of ion and electron temperature or pressure. In equation 2.17, which is the linearized Ohm's law, the Weyl gauge

$$\boldsymbol{E}_1 = -\partial_t \boldsymbol{A}_1 = -\lambda \boldsymbol{A}_1 \tag{2.19}$$

has been used [34]. In general, the Weyl gauge is incomplete since it allows for transformations $\boldsymbol{A}(\boldsymbol{r}, t) \rightarrow \boldsymbol{A}(\boldsymbol{r}, t) + \boldsymbol{\nabla}\varphi(\boldsymbol{r})$ where φ is an arbitrary time-independent potential. However, $\boldsymbol{A}_1$ in equation 2.17 represents the time-dependent part of the vector potential, i.e. $\boldsymbol{A}_1(\boldsymbol{r}, t) = \boldsymbol{A}_1(\boldsymbol{r})e^{\lambda t}$, which is completely fixed by the Weyl gauge.

2.3.2 The CASTOR3D code

The CASTOR3D code [32, 33, 34] solves the linear MHD equations defined in equations 2.14 to 2.17 in general right-handed curvilinear coordinates $(s, v, u) \in [0, 1]^3$, where s, v and u are the radial, toroidal and poloidal coordinates, respectively. The plasma part of CASTOR3D has been developed based on the axisymmetric resistive MHD stability code CASTOR [37], while the vacuum part has been substituted by integration of the STARWALL code [45]. In order to solve the MHD equations numerically, the linear equation system is transformed to a discrete eigenvalue problem. The system of linearized MHD equations is of the form

$$\lambda \mathcal{S} \boldsymbol{\chi} = \mathcal{R} \boldsymbol{\chi} \tag{2.20}$$

where $\boldsymbol{\chi} = (\rho_1, \boldsymbol{v}_1, T_1, \boldsymbol{A}_1)$ is the eigenvector, $\mathcal{S}$ is a diagonal matrix and $\mathcal{R}$ contains differential operators and equilibrium quantities. Similar to the CASTOR code [37], the fluid quantities contained in the physical eigenvector $\boldsymbol{\chi}$ are, without loss of generality, expressed as [32]:

$$\begin{aligned} \rho_1 &= \frac{1}{s}\widehat{\rho} \quad , \qquad \boldsymbol{v}_1 = \frac{R^2}{\sqrt{g}}\widehat{v}^s \boldsymbol{r}_{,s} + \frac{R^2}{i\sqrt{g}}\widehat{v}^u \boldsymbol{r}_{,u} + \frac{qR^2}{i\widehat{f}}\widehat{v}^v \boldsymbol{B}_0 \\ T_1 &= \frac{1}{s}\widehat{T} \quad , \qquad \boldsymbol{A}_1 = -i\widehat{A}_s \boldsymbol{\nabla} s + \widehat{A}_u \boldsymbol{\nabla} u + \widehat{A}_v \boldsymbol{\nabla} v \end{aligned} \tag{2.21}$$

where $\sqrt{g}$ is the Jacobian and $\widehat{f} = \partial_s \phi$ is the derivative of the toroidal flux ϕ. The vector $\widehat{\boldsymbol{\chi}} = (\widehat{\chi}_f)_{f=1\ldots8} = (\widehat{\rho}, \widehat{v}^s, \widehat{v}^u, \widehat{v}^v, \widehat{T}, \widehat{A}_s, \widehat{A}_u, \widehat{A}_v)$ is the projected eigenvector and yields a coordinate representation of the physical eigenvector. The ansatz for the eigenfunctions $\widehat{\chi}_f$ is based on a Fourier decomposition in the periodic coordinates u and v and a radial discretization using Hermite polynomials [32]:

$$\widehat{\chi}_f = \sum_{m,n,j,k} \left(c^{m,n}_{f,j,k} H^j_{f,k} e^{2\pi i(mu+nv)} + \bar{c}^{m,n}_{f,j,k} H^j_{f,k} e^{-2\pi i(mu+nv)} \right) \tag{2.22}$$

where m is the poloidal mode number, n is the toroidal mode number, j is the radial grid point, $H^j_{f,k}$ is the k-th Hermite polynomial with $k \in \{1, 2\}$ as defined in [37]. In order to avoid summing each Fourier harmonic twice in equation 2.22, the toroidal harmonics are defined to be either positive $n \geqslant 0$ or negative $n \leqslant 0$. The degree of the Hermite polynomials is cubic for $\widehat{v}^s$, $\widehat{A}_u$ and $\widehat{A}_v$ and quadratic for all other perturbed quantities. The coefficients $c^{m,n}_{f,j,k}$ and $\bar{c}^{m,n}_{f,j,k}$ are the complex and

complex-conjugate coefficients. The splitting into complex and complex-conjugate exponential functions can also be interpreted as a splitting into positive and negative toroidal mode numbers, since the summation in equation 2.22 is restricted to either positive or negative n. In the context of an oscillating mode, i.e. $\boldsymbol{\chi} \sim e^{i\omega t}$ with $\omega \neq 0$, the positive and negative harmonics can be seen to describe left-traveling and right-traveling waves. Since the ansatz 2.22 is based on a Fourier decomposition in the periodic coordinates, it cannot be applied to plasma volumes that extend across the separatrix. For this reason, the plasma volume is assumed to be bounded by a closed flux surface which is located close to the separatrix, the so-called Last Closed Flux Surface (LCFS). The LCFS is usually chosen to be located at a poloidal flux of $\psi \geqslant 0.99\psi_{\text{sep}}$, where ψ_{sep} is the poloidal flux at the separatrix.

Equation 2.20 can be transformed to the weak form by multiplication with appropriate test functions, using the same radial and poloidal discretization as in 2.22 as described in [32]. Finally, inserting the ansatz 2.21, using the poloidal and toroidal Fourier decomposition of the equilibrium quantities and integrating over the plasma volume yields a non-hermitian matrix eigenvalue problem of the form [32]:

$$\lambda \mathcal{B}\boldsymbol{x} = \mathcal{A}\boldsymbol{x} \quad \text{with} \quad \boldsymbol{x} = (\{c^{m,n}_{f,j,k}, \bar{c}^{m,n}_{f,j,k}\}) \tag{2.23}$$

where $\boldsymbol{x}$ is the coefficient eigenvector. The two sparse block-tridiagonal square matrices $\mathcal{A}$ and $\mathcal{B}$, which are structured as shown in figure 2.1, have $N_{\text{mat}} = 32 N_j N_{mn}$ rows or columns representing the perturbation in the plasma volume, where N_j is the number of radial discretization points and N_{mn} is the number of Fourier harmonics (m, n). In addition, the matrices can be extended to include the coupling of the plasma to response currents in resistive and ideal wall or coil structures (blue, green and purple blocks in figure 2.1) [32]. If the $(m, n) = (0, 0)$ harmonic is not contained in the spectrum of the perturbation and if there are no resistive wall or coil structures, it is possible to solve the external part of the matrix separately [32, 46]. In conclusion, the CASTOR3D code calculates the matrix elements of $\mathcal{A}$ and $\mathcal{B}$ and solves the eigenvalue problem 2.23.

2.3.3 Mode coupling

The matrix elements X of the eigenvalue problem 2.23 are of the form [32]:

$$X^{\widetilde{j},\widetilde{k},\widetilde{f},\widetilde{m},\widetilde{n}}_{j,k,f,m,n} = \sum_{M,N} C_{M,N,j,\widetilde{j},\ldots} \int_0^1 \int_0^1 e^{-2\pi i(\widetilde{m}u + \widetilde{n}v)} e^{2\pi i(Mu+Nv)} e^{2\pi i(mu+nv)} \,\mathrm{du}\,\mathrm{dv} \tag{2.24}$$

where (M, N) are the poloidal and toroidal equilibrium harmonics. Indices and mode numbers corresponding to the test function are denoted by a tilde. The matrix element X is related to the complex or complex conjugate coefficients $c^{m,n}_{f,j,k}$ and $\bar{c}^{m,n}_{f,j,k}$ by the sign of the toroidal harmonics n and $\widetilde{n}$. As discussed earlier, the splitting into positive and negative toroidal harmonics is equivalent to the splitting into complex and complex-conjugate exponential functions, but allows the structure of all matrix elements to be summarized in a single equation. In equation 2.24, the quantity C contains the equilibrium Fourier coefficients, including the ansatz 2.21, as well as the Hermite polynomials and has been integrated over the radial coordinate. The structure of the matrix elements implies that only elements where

$$m - \widetilde{m} = M \quad \text{and} \quad n - \widetilde{n} = N \tag{2.25}$$

can be non-zero. This means that two different perturbation Fourier harmonics (m, n) and $(\widetilde{m}, \widetilde{n})$ can only couple if there is a finite contribution of an equilibrium

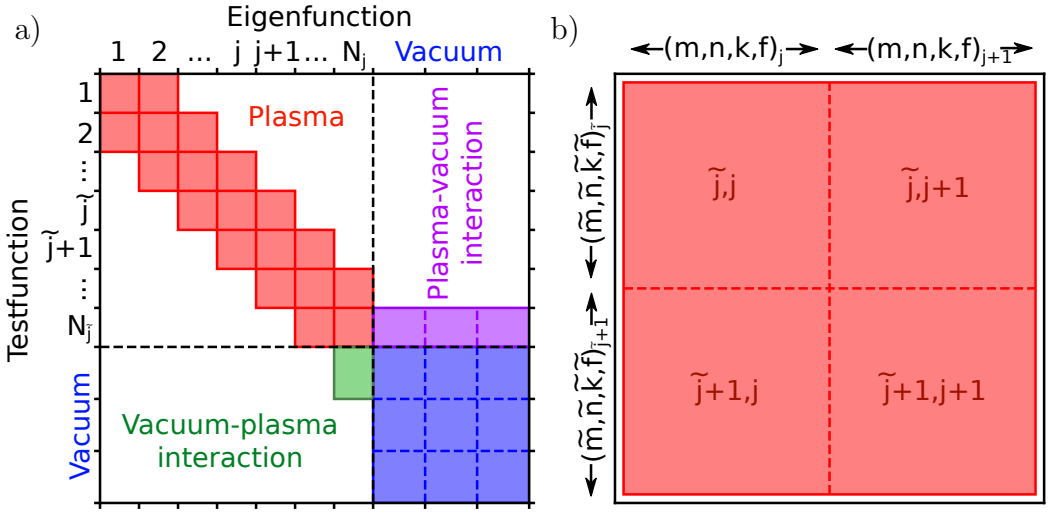

Figure 2.1: a) Structure of the matrices $\mathcal{A}$ and $\mathcal{B}$ with plasma-vacuum interaction including wall and coil structures as described in [32]. The purple block is only included in matrix $\mathcal{A}$ while the green block is only included in matrix $\mathcal{B}$. b) Structure of a plasma-volume block. Each of the 4 subblock contains rows and columns for the Fourier harmonics, complex and complex-conjugate coefficients, Hermite polynomials and physical quantities.

harmonic (M, N) which fulfills equation 2.25. In the following, a range of conclusions is deduced from equations 2.22, 2.24 and 2.25.

In the case of axisymmetry, i.e. $N = 0$ is the only toroidal equilibrium harmonic, the toroidal mode numbers n are completely decoupled. This means that there is no change in growth rate and energy connected to the coupling of toroidal harmonics. For this reason, the stability for each toroidal mode number n can be analyzed independently in an axisymmetric plasma and n can be used to label the instabilities. Moreover, the two decoupled equation systems corresponding to the complex or complex conjugate coefficients $c^{m,n}_{f,j,k}$ and $\bar{c}^{m,n}_{f,j,k}$ are equivalent, which results in pairs of degenerate eigenvalues λ_1 and λ_2. In this context, the term degenerate means $\lambda_1 = \lambda_2^*$ and the corresponding eigenvectors describe exactly the same physical perturbation. This can be seen by relating the solutions of the complex and complex-conjugate equation systems. Expressing a solution $\boldsymbol{\chi}^{(1)}$ of the complex equation system with growth rate λ_1 and Fourier coefficients $\boldsymbol{\chi}^{(1)}_{m,n}$ in terms of the complex conjugate Fourier harmonics results in:

$$\begin{aligned}\boldsymbol{\chi}^{(1)}(\boldsymbol{r},t) &= \sum_{n\geqslant 0,m} \boldsymbol{\chi}^{(1)}_{m,n} e^{2\pi i(mu+nv)} e^{\lambda_1 t} = \left(\sum_{n\geqslant 0,m} \left(\boldsymbol{\chi}^{(1)}_{m,n}\right)^* e^{-2\pi i(mu+nv)} e^{\lambda_1^* t} \right)^* \\ &= \left(\sum_{n\geqslant 0,m} \boldsymbol{\chi}^{(2)}_{m,n} e^{-2\pi i(mu+nv)} e^{\lambda_2 t} \right)^* = \left(\boldsymbol{\chi}^{(2)}\right)^* (\boldsymbol{r},t) \end{aligned} \tag{2.26}$$

with

$$\boldsymbol{\chi}^{(2)}_{m,n} = \left(\boldsymbol{\chi}^{(1)}_{m,n}\right)^* \quad \text{and} \quad \lambda_2 = \lambda_1^* \tag{2.27}$$

Clearly, if $\left(\boldsymbol{\chi}^{(2)}\right)^*$ solves the MHD equations, $\boldsymbol{\chi}^{(2)}$ yields an equivalent solution of the MHD equations. This implies that $\boldsymbol{\chi}^{(2)}$ with growth rate $\lambda_2 = \lambda_1^*$ and coefficients $\boldsymbol{\chi}^{(2)}_{m,n}$ is a solution of the complex-conjugate equation system. In conclusion, every

solution in the complex equation system is related to a degenerate solution in the complex-conjugate equation system.

Consequently, as will be further discussed in chapter 5, pairs of degenerate eigenvalues are also found in non-axisymmetric plasmas if there is no or negligible coupling between positive and negative toroidal harmonics. As in the case of axisymmetry, the decoupling of positive and negative toroidal harmonics results in two equivalent decoupled equation systems. The degenerate solutions can be omitted by only considering the contributions related to one of the two equation systems, i.e. restricting equation 2.22 to $c^{m,n}_{f,j,k}$, which halves the size of the eigenvalue problem.

If there are finite contributions of equilibrium Fourier harmonics with $N \neq 0$, toroidal perturbation harmonics n can couple together to form instabilities. For a system with toroidal periodicity N_P, equation 2.25 implies that the toroidal harmonics can be grouped into $\lfloor (N_P+1)/2 \rfloor$ toroidal mode families, where only toroidal harmonics of the same mode family can couple together [47]. In the case of a system with periodicity $N_P = 2$, there are two mode families $\mathcal{N}_1 = \{1, 3, 5, 7, \dots\}$ and $\mathcal{N}_2 = \{0, 2, 4, 6, \dots\}$. Since the toroidal Fourier harmonics in a mode family couple together, instabilities cannot be described by a single toroidal Fourier harmonic n [47]. However, especially in the case of weakly non-axisymmetric equilibria, there is usually a dominant toroidal Fourier harmonic n^*, which will be used to label the instabilities. Furthermore, in the non-axisymmetric case, the eigenvalue pair λ_1 and λ_2 related to an instability n^* can become non-degenerate by the coupling of negative and positive toroidal Fourier harmonics. In this case, the two related instabilities are distinguished into a "fast" and "slow" solution by their growth rate.

Finally, equation 2.25 yields a necessary requirement for mode coupling. However, for the formation of instabilities, harmonics which fulfill equation 2.25 might not couple if the coupling is energetically unfavourable. The arguments for toroidal mode coupling hold also for the poloidal Fourier harmonics. For a toroidal plasma, especially with shaped plasma cross-section (e.g. by elongation, triangularity, ...), there is a broad range of poloidal harmonics in the Fourier decomposition of the equilibrium quantities, required to encode the effects of finite aspect ratio and shaping. For this reason, the spectrum of instabilities usually contains many coupled poloidal Fourier harmonics.

2.3.4 Energy functional

Since the linearized MHD equations as defined in equations 2.14 to 2.17 take various physics phenomena into account, they are extremely complex and can only be solved numerically. Valuable insight into MHD stability can be obtained by neglecting several of these phenomena. In the case of flow-free ideal MHD, i.e. neglecting resistivity, viscosity, gyro-viscosity and equilibrium flows, the eigenvalue problem is reduced to a single equation [35]:

$$\rho_0 \lambda^2 \boldsymbol{\xi} = \boldsymbol{\nabla}(\boldsymbol{\xi} \cdot \boldsymbol{\nabla} p_0) + \boldsymbol{\nabla}(p_0 \Gamma (\boldsymbol{\nabla} \cdot \boldsymbol{\xi})) + \frac{1}{\mu_0}(\boldsymbol{\nabla} \times \boldsymbol{B}_0) \times \boldsymbol{B}_1 + \frac{1}{\mu_0}(\boldsymbol{\nabla} \times \boldsymbol{B}_1) \times \boldsymbol{B}_0 \quad (2.28)$$

with

$$\boldsymbol{B}_1 = \boldsymbol{\nabla} \times (\boldsymbol{\xi} \times \boldsymbol{B}_0) \quad (2.29)$$

where the plasma displacement $\boldsymbol{\xi}$ is defined by $\boldsymbol{v}_1 = \partial_t \boldsymbol{\xi} = \lambda \boldsymbol{\xi}$. It can be shown that the eigenvalue problem defined in equation 2.28 is self-adjoint, which means that the eigenvalues λ^2 are real-valued and stability is determined by the sign of λ^2 [9].

This allows a variational principle, the so-called energy principle, to be derived from equation 2.28 which is of the form [35]:

$$\delta W(\boldsymbol{\xi}, \boldsymbol{\xi}^*) \equiv -\frac{1}{2} \int \boldsymbol{\xi}^* \cdot \mathcal{F}_{\mathrm{id}} \boldsymbol{\xi} \, \mathrm{dV} = -\frac{\lambda^2}{2} \int \rho_0 \boldsymbol{\xi} \cdot \boldsymbol{\xi}^* \, \mathrm{dV} \equiv -\lambda^2 K(\boldsymbol{\xi}, \boldsymbol{\xi}^*) \tag{2.30}$$

where $\mathcal{F}_{\mathrm{id}}\boldsymbol{\xi}$ is given by the right-hand side of equation 2.28 and represents the force acting on the displaced fluid element. The functional $\delta W(\boldsymbol{\xi}, \boldsymbol{\xi}^*)$ is related to the potential energy of the perturbation $\boldsymbol{\xi}$, while the quantity $-\lambda^2 K(\boldsymbol{\xi}, \boldsymbol{\xi}^*)$ is related to the kinetic energy. Linear ideal MHD stability codes such as CAS3D [48] solve the ideal MHD eigenvalue problem for 3D plasmas in the form of the energy principle 2.30, which corresponds to the weak formulation of equation 2.28. Since the eigenvalue problem of ideal MHD is self-adjoint, instabilities can be found by minimizing the energy functional $\delta W(\boldsymbol{\xi}, \boldsymbol{\xi}^*)$ for a fixed value of the norm $K(\boldsymbol{\xi}, \boldsymbol{\xi}^*)$. The energy functional allows us to analytically study MHD stability and determine stability criteria by minimizing the energy functional with respect to certain sets of test functions. The chosen sets of test functions can be identified with certain classes of instability. Consequently, because of the restriction to certain sets of test functions or classes of instability, the stability criteria are necessary but not sufficient to guarantee stability and the described instabilities are generally not the most unstable ones. In addition, the energy functional can be rewritten into an intuitive form, yielding valuable information on the different energetic drives of the ideal MHD instabilities [35, 38, 49]:

$$\delta W = \delta W_V + \delta W_S + \delta W_{\breve{V}} \tag{2.31}$$

with

$$2\delta W_{\breve{V}} = \int_{\mathrm{Vacuum}} \frac{\|\breve{\boldsymbol{B}}_1\|^2}{\mu_0} \, \mathrm{d}\breve{\mathrm{V}} \tag{2.32}$$

$$2\delta W_S = \oint_{\mathrm{Surface}} |\boldsymbol{n} \cdot \boldsymbol{\xi}|^2 \boldsymbol{n} \cdot \left[\!\left[\boldsymbol{\nabla}(p_0 + \frac{\boldsymbol{B}_0^2}{2\mu_0}) \right]\!\right] \mathrm{dS} \tag{2.33}$$

$$\begin{aligned} 2\delta W_V = \int_{\mathrm{Plasma}} & \underbrace{\frac{\|\boldsymbol{B}_{1,\perp}\|^2}{\mu_0}}_{W_{\mathrm{SHA}}} \underbrace{+ \frac{\boldsymbol{B}_0^2}{\mu_0} \left| \boldsymbol{\nabla} \cdot \boldsymbol{\xi}_\perp + 2(\boldsymbol{\xi}_\perp \cdot \boldsymbol{\kappa}) \right|^2}_{W_{\mathrm{CPA}}} \underbrace{+ \Gamma p_0 |\boldsymbol{\nabla} \cdot \boldsymbol{\xi}|^2}_{W_{\mathrm{SND}}} \\ & \underbrace{- \frac{j_{0,\parallel}}{\|\boldsymbol{B}_0\|} (\boldsymbol{\xi}_\perp^* \times \boldsymbol{B}_0) \cdot \boldsymbol{B}_{1,\perp}}_{W_{\mathrm{CUR}}} \underbrace{- 2(\boldsymbol{\xi}_\perp \cdot \boldsymbol{\nabla} p_0)(\boldsymbol{\xi}_\perp^* \cdot \boldsymbol{\kappa})}_{W_{\mathrm{DP0}}} \, \mathrm{dV} \end{aligned} \tag{2.34}$$

where $\delta W_{\breve{V}}$ is the always positive vacuum contribution, δW_S is the energy connected to jumps of equilibrium quantities across the perturbed plasma-vacuum interface, δW_V is the energy of the plasma volume and vacuum quantities are denoted with an inverted hat (e.g. $\breve{\boldsymbol{B}}_1$). In the absence of equilibrium surface currents, the surface term is strictly zero. The first three terms of the plasma contribution are always positive and related to perpendicular magnetic perturbations, parallel magneto-compressional perturbations and adiabatic compression, respectively [35, 49]. The last two terms are potentially negative, i.e. destabilizing. The first destabilizing term W_{CUR} describes instabilities which are driven by the parallel equilibrium current density $j_{0,\parallel} = \boldsymbol{j}_0 \cdot \boldsymbol{b}$ with $\boldsymbol{b} = \boldsymbol{B}_0/\|\boldsymbol{B}_0\|$, while W_{DP0} describes instabilities which are driven by the pressure gradient in regions of unfavourable curvature $\boldsymbol{\kappa} = (\boldsymbol{b} \cdot \boldsymbol{\nabla})\boldsymbol{b}$, where unfavourable means $\boldsymbol{\kappa} \cdot \boldsymbol{\nabla} p_0 > 0$ [35, 49]. The intuitive formulation of the energy functional allows instabilities to be categorized by their driving mechanisms and to study pressure-gradient and current-density driven modes separately. The energetic decomposition in equations 2.32 to 2.34 is extended to resistive plasmas and further discussed in chapter 3.

2.3.5 Straight field line coordinates

In the limit of infinite aspect ratio, i.e. ignoring the effects of toroidicity, the tokamak can be described as a periodic cylinder with the radial, poloidal and "toroidal" coordinates (r, Φ, θ). Since this configuration features cylindrical symmetry, all Fourier harmonics are completely decoupled. Expressing the energy functional in the periodic cylinder limit reveals that all stabilizing plasma volume contributions to δW vanish on flux surfaces which fulfill

$$q = m/n \tag{2.35}$$

for a certain harmonic (m, n) [35]. These flux surfaces, called resonant surfaces, are particularly prone to instabilities. For a straight cylinder, the magnetic field lines appear straight in the (Φ, θ)-plane. Consequently, the (m, n) harmonic is perfectly aligned with the field lines on the resonant surface, which avoids the strongly stabilizing energy contribution related to the bending of magnetic field lines [35].

While the stability analysis becomes more complex in the case of finite aspect ratio, the stabilizing effect of field line bending remains. Thus, also in the case of finite aspect ratio, it is favourable for instabilities to be approximately aligned with the magnetic field lines [35]. This motivates the introduction of poloidal and toroidal coordinates (Φ_s, θ_s) in which the magnetic field lines appear straight. These coordinates fulfill the condition

$$\frac{\boldsymbol{B} \cdot \boldsymbol{\nabla} \theta_s}{\boldsymbol{B} \cdot \boldsymbol{\nabla} \Phi_s} = \text{const.} \tag{2.36}$$

and are generally called straight field line coordinates. In straight field line coordinates, Fourier harmonics which fulfill the resonance condition 2.35 are aligned with the magnetic field lines and intrinsically minimize field line bending on the resonant surface. For this reason, straight field line coordinates are the natural choice for the Fourier decomposition of MHD instabilities in toroidal geometry.

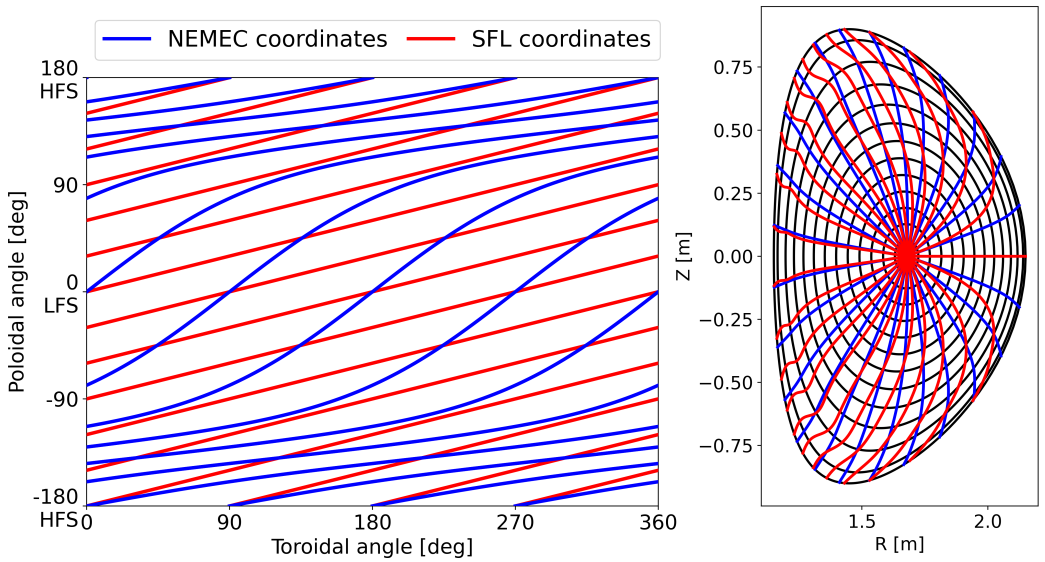

Figure 2.2: Magnetic field lines on an unrolled flux surface (a) as well as lines of constant poloidal angle on a toroidal cross-section (b) are shown for NEMEC coordinates $(\Phi, \theta_{\text{NEM}})$ (blue) and SFL coordinates (Φ, θ^*) (red).

In this thesis, two straight field line coordinate systems are used: 2D straight field line coordinates (SFL) [37] and Boozer coordinates (BZR) [50]. SFL coordinates (Φ, θ^*) are used for axisymmetric plasmas and keep the toroidal angle Φ unchanged. BZR coordinates can be used for axisymmetric and non-axisymmetric plasmas and change both angle coordinates such that also the diamagnetic lines $\boldsymbol{\nabla} s \times \boldsymbol{B}$, which describe the direction of the diamagnetic drift velocity, are straight. Magnetic field lines on an unrolled flux surface as well as lines of constant poloidal angle on a toroidal cross-section are shown for NEMEC coordinates, which are nearly geometric, and SFL coordinates in figure 2.2.

2.3.6 Edge localized instabilities

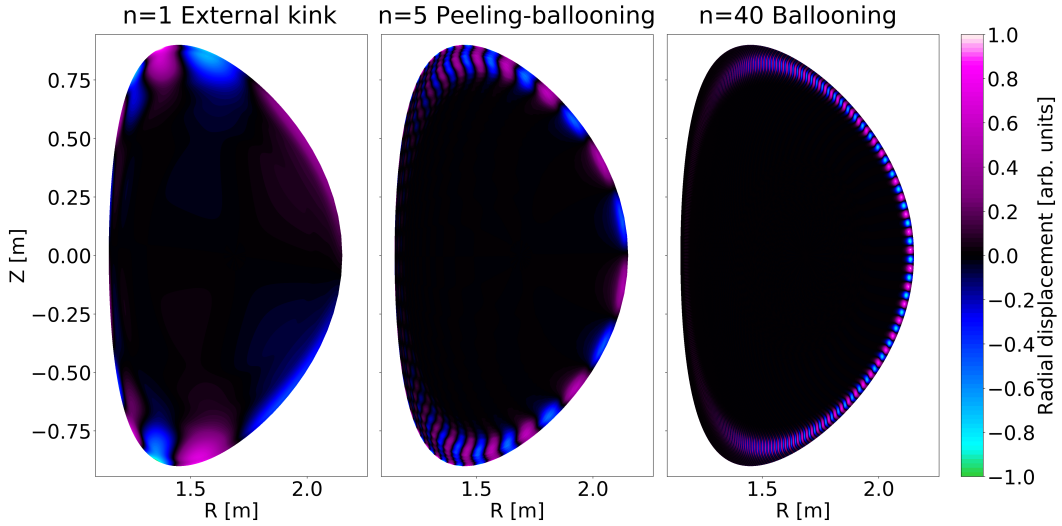

Figure 2.3: Radial displacement of an (a) $n = 1$ external kink, (b) $n = 5$ peeling-ballooning and (c) $n = 40$ ballooning mode.

Expressing the energy functional of ideal MHD in appropriate coordinates and using reasonable test functions, two fundamental classes of edge localized MHD instabilities can be identified. These are the current-density driven external kink/peeling modes and the pressure-gradient driven ballooning modes [35]. These instabilities can couple together and form peeling-ballooning modes. The ELM onset in H-mode tokamak plasmas is typically well-described by the growth of these coupled peeling-ballooning modes [16, 17]. The radial displacement for an external kink, peeling-ballooning and ballooning mode is shown in figure 2.3 on the toroidal plasma cross-section. The radial and poloidal localization increase with increasing toroidal mode number. While kink modes are usually localized at the top and bottom regions of an elongated plasma, ballooning modes are strongly localized at the low-field side, where the field line curvature is unfavourable $\boldsymbol{\kappa} \cdot \boldsymbol{\nabla} p_0 > 0$. In general, the localization of kink modes depends strongly on the shaping of the plasma cross-section.

The typical structures of a low-n and high-n external kink mode are shown in figure 2.4. The amplitude of the harmonics increases towards the vacuum region and the dominating poloidal harmonic has its maximum at the plasma boundary. Since the displacement caused by low-n external kink modes extends over a broad radial region of the plasma, these instabilities are usually very violent. The high-n external kink modes, often called peeling modes, are strongly localized at the plasma bound-

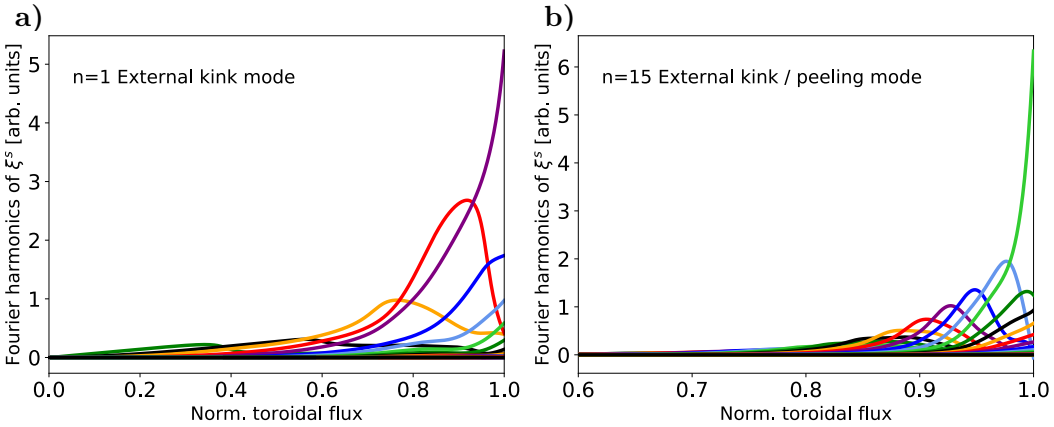

Figure 2.4: Fourier harmonics of the radial displacement for an $n = 1$ external kink mode (a) and an $n = 15$ external kink / peeling mode (b) in straight field line coordinates.

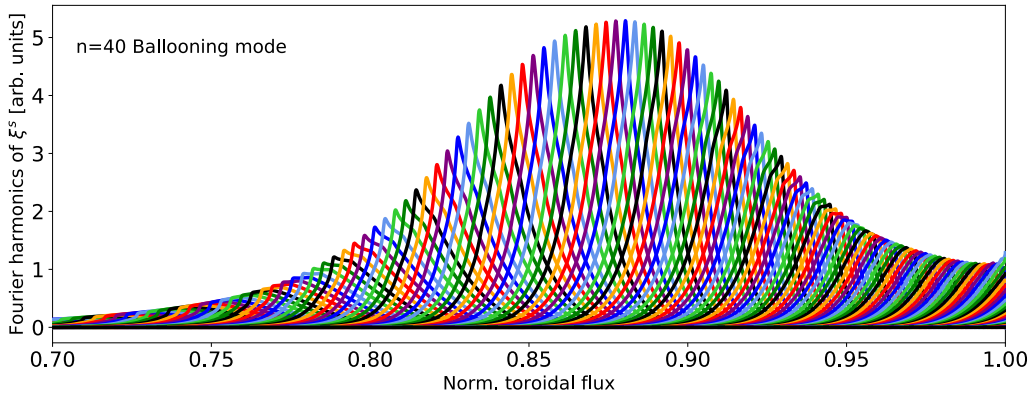

Figure 2.5: Fourier harmonics of the radial displacement for an $n = 40$ ballooning mode in straight field line coordinates.

ary [35]. Each Fourier harmonic that has a resonant surface inside the plasma region is peaked at this resonant surface in agreement with the resonance condition 2.35. The Fourier harmonics which are peaked at the plasma boundary are said to have a resonant surface in the vacuum region.

The pressure-gradient driven ballooning modes are derived from the energy functional in the limit of high toroidal mode number $n \gg 1$ [35]. These modes poloidally localize in the regions of unfavourable curvature by the superposition of many Fourier harmonics. The typical structure of a ballooning mode is shown in figure 2.5. Ballooning modes are localized at the steep-gradient region in the edge. Each Fourier harmonic is strongly radially localized and peaked at its resonant surface.

In the vicinity of the stability threshold of peeling and ballooning modes, both modes can couple together to form peeling-ballooning modes. The Fourier harmonics of a peeling-ballooning mode, shown in figure 2.6a, are similar to those of the ballooning mode but contain a peeling harmonic, which is strongly peaked at the plasma boundary. The stability of the H-mode pedestal can be summarized in the space of pedestal current density and pedestal pressure gradient, which is shown in figure 2.6b [16]. At high pedestal pressure gradient the growth of ballooning modes limits the pedestal, while the pedestal current density is limited by external kink modes. In the region close to both the peeling and the ballooning stability boundaries coupled

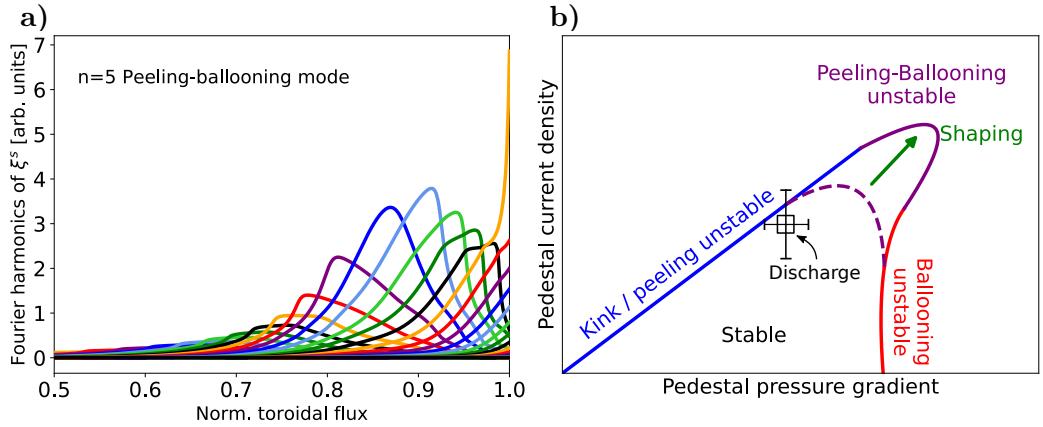

Figure 2.6: a) Fourier harmonics of the radial displacement for an $n = 5$ peeling-ballooning mode in straight field line coordinates. b) Sketch of the peeling-ballooning stability diagram. The line indicates the theoretically predicted stability boundary, while the box with error bars marks a point of operation during a discharge.

peeling-ballooning modes are excited. Shaping of the plasma cross-section can stabilize the peeling-ballooning modes and increase the maximum achievable pedestal pressure gradient as shown schematically in figure 2.6b [16].

2.3.7 Interpretative and predictive stability analysis

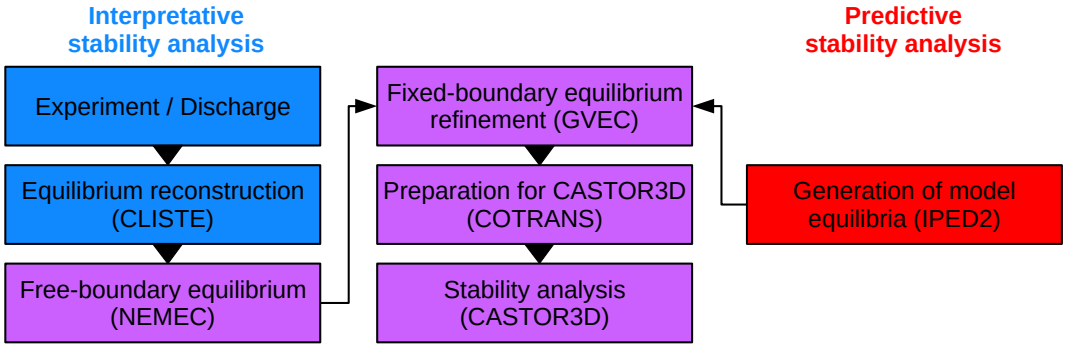

Figure 2.7: Workflow for the predictive and interpretative stability analysis.

The pedestal stability can be analyzed based on experimental equilibria obtained from an equilibrium reconstruction. This method, known as interpretative stability analysis, yields information on the specific instabilities that were observed during a discharge and can be used to verify the results obtained with numerical stability analysis. On the other hand, stability can be analyzed based on modelled equilibria, which are created from a reduced set of parameters. This enables the predictive analysis of MHD stability. In this work, model pressure and safety factor profiles as well as 2D plasma boundaries are generated using the predictive pedestal stability framework IPED2 [51]. IPED2 generates a range of model equilibria with different pedestal top pressures for a set of operational plasma parameters: major and minor plasma radius, elongation and triangularity of the toroidal plasma cross-section, toroidal magnetic field at the axis, plasma current, pedestal top density and the volume-averaged plasma pressure. Analyzing the stability of the generated model equilibria yields the critical pedestal top pressure above which MHD instabilities are triggered for the specified set of operational parameters. The obtained stability

boundary (boundary in figure 2.6b) might then be compared to the operational point of a stable or unstable discharge (box with error bars in figure 2.6b). The workflow for both the predictive and interpretative stability analysis is shown in figure 2.7. For the predictive and interpretative stability analysis a high-resolution equilibrium is calculated using the GVEC code, as described in section 2.2. The COTRANS code, which represents an interface between the equilibrium codes and CASTOR3D, then transforms the equilibrium to straight field line coordinates (SFL or BZR) and calculates the Fourier decomposition of the equilibrium quantities required for the eigenvalue problem 2.23. Finally, the stability of the equilibrium is analyzed using the CASTOR3D code.

3 Extension and optimization of the COTRANS and CASTOR3D codes

In order to study edge localized instabilities in non-axisymmetric tokamak plasmas, several improvements to the CASTOR3D framework were necessary. These improvements, enabling the work presented in this thesis, are discussed in the following.

3.1 Optimization of the COTRANS code

The strongly shaped edge region close to the separatrix in combination with the steep safety factor profile of tokamak plasmas results in strongly non-orthogonal straight field line coordinates, where the poloidal and radial basis vectors are almost parallel, as shown in figure 3.1. Thus, the precise mapping of quantities between the equilibrium coordinate system and straight field line coordinates for realistic tokamak geometries is numerically challenging and typically requires calculation of the transformation with extremely high resolution. Using previous versions of COTRANS, such mappings with several thousands of flux surfaces and hundreds of Fourier harmonics would require days of CPU time for a single equilibrium. For this reason, several sequential parts of COTRANS were parallelized, parts of the previous parallelization were optimized to allow calculations to be scheduled dynamically and numerous Fourier transforms were replaced by Fast Fourier Transform (FFT) algorithms. As a result, the CPU time for the high-resolution mappings could be reduced from hours to seconds or from days to minutes. The speedup is mainly due to the implementation of the FFTs, reducing the computational complexity from $\mathcal{O}(N_M^2 N_N^2)$ to $\mathcal{O}(N_M N_N \log(N_M N_N))$, where N_M and N_N are the numbers of poloidal and toroidal grid points used to map the equilibrium. These improvements required for example unique changes to the 42 routines in which the 383 metric elements for the eigenvalue problem are calculated. Furthermore, the replacement of the Fourier transformation required significant structural changes to major fractions of the code. Finally, the code is carefully tested after any change by benchmarking with previous versions and evaluation of several physical metrics as well as the equilibrium force balance.

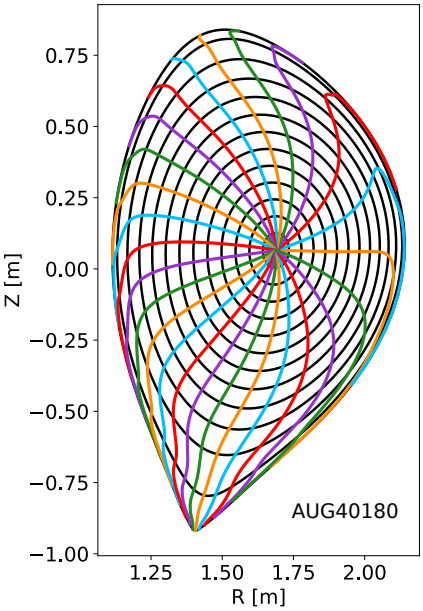

Figure 3.1: Flux surfaces (black) and lines of constant poloidal straight field line angle (colored) for an AUG equilibrium.

3.2 Force balance verification

Since the integrity of the linear MHD equations fundamentally depends on the quality of the force balance, it is crucial to test for the error of the force balance in order to enable an accurate stability analysis. The structure of the instabilities as well as the energetic decomposition, discussed in chapter 4, strongly depend on the local force balance. For this reason, calculations of the (radial) force imbalance

$$\Delta F_{\mathrm{MHD}} = (\boldsymbol{j} \times \boldsymbol{B} - \boldsymbol{\nabla} p) \cdot \boldsymbol{r}_{,s} = \boldsymbol{j} \times \boldsymbol{B} \cdot \boldsymbol{r}_{,s} - \partial_s p \tag{3.1}$$

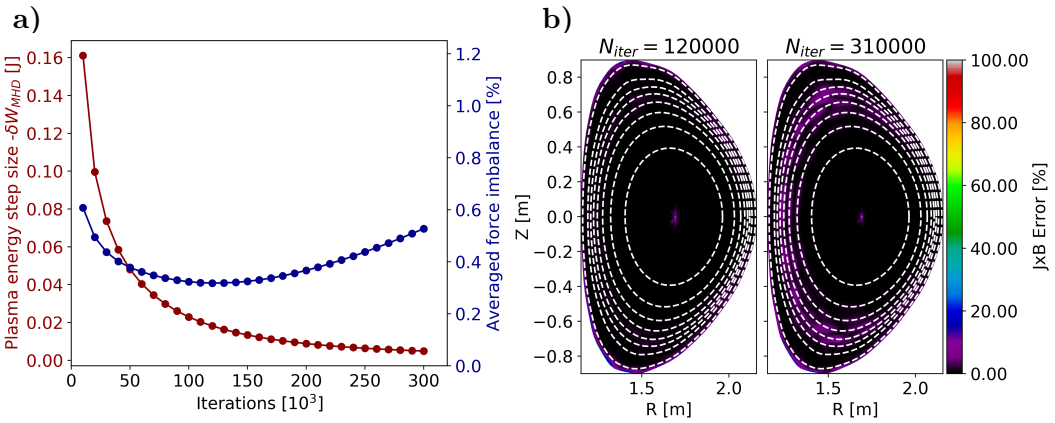

Figure 3.2: a) Step size $-\delta W_{\mathrm{MHD}}$ of the plasma energy 2.13 and average of the absolute values (L1 norm) of the local force imbalance normalized w.r.t. the pressure gradient $\|\Delta F_{\mathrm{MHD}}/\partial_s p\|_1$ over the iterations of the minimization process of a non-axisymmetric equilibrium using GVEC. b) Local force imbalance on a toroidal plasma cross-section after 120000 and 310000 iterations of the equilibrium code. The dashed white lines indicate resonant surfaces with respect to the dominating toroidal harmonic $N = 2$ of the applied MP field.

were implemented at various points of the workflow (after the equilibrium code, after the coordinate transformation and within the stability code itself). The various force imbalance calculations allow the cause of a potential force imbalance to be precisely tracked down to a certain point in the workflow. Firstly, the MHD energy 2.13 or net radial forces $\langle \Delta F_{\mathrm{MHD}} \rangle$, which are the typical metrics used to measure convergence by equilibrium codes, might seem to be well-converged while there are growing local force imbalances, which is demonstrated in figure 3.2. While the plasma energy or net forces might average over local force imbalances in opposite directions, the average of the absolute values (L1 norm) of the local force imbalance normalized w.r.t. the pressure gradient $\|\Delta F_{\mathrm{MHD}}/\partial_s p\|_1$ reveals local violations of the force balance. Local force imbalances during the minimization of the plasma energy might for example be caused by the susceptibility of the equilibrium solution to MHD instabilities. If the equilibrium is strongly unstable to internal instabilities, equilibrium codes that minimize the plasma energy are capable of evolving instability-like perturbations as shown in figure 3.3 (see [52, 53, 54, 55]). Further violations of the force balance might be introduced if the resolution for the coordinate transformation into straight field line coordinates is chosen too low. Finally, the force balance verification in the stability code tests for errors in the Fourier

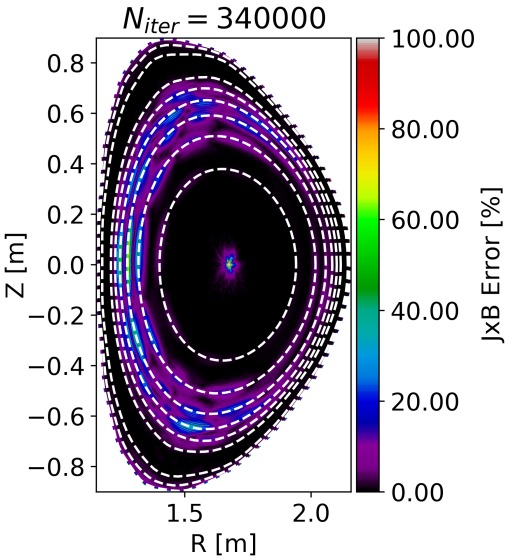

Figure 3.3: Instability-like local force imbalance on a toroidal plasma cross-section of a non-axisymmetric strongly unstable equilibrium after 340000 iterations of energy minimization using the GVEC code. The dashed white lines indicate resonant surfaces with respect to the dominating toroidal harmonic $N = 2$ of the applied MP field.

transformations of the equilibrium quantities performed in CASTOR3D. The implemented force imbalance calculations allow a high-quality of the equilibrium solution throughout the entire workflow of the MHD stability analysis to be maintained. This might save significant amounts of computational resources since corrupted equilibria can be identified early in the workflow.

3.3 Optimization of the eigenvalue problem size

The pedestal stability analysis of non-axisymmetric tokamak plasmas is numerically challenging, since a high radial resolution as well as a large amount of poloidal and toroidal harmonics are required in order to resolve the edge localized instabilities. Since the size of the N_j matrix blocks depends on the amount of poloidal and toroidal harmonics, N_m and N_n, the resolution necessary to describe edge localized instabilities results in a huge eigenvalue problem. The memory required for the factorization of the generally non-hermitian matrix roughly scales with the amount of non-zero matrix elements:

$$\text{Mem} \sim N_j (N_m N_n)^2 \tag{3.2}$$

This is demonstrated for a range of CASTOR3D runs in figure 3.4a. Thus, the memory requirement for the stability analysis rapidly increases with the amount of Fourier harmonics and the available memory sets an upper limit for the observable physical problem size. For this reason, the memory requirement must be minimized in order to study high-n edge localized instabilities. In the following, the minimal amount of Fourier harmonics required to describe edge localized instabilities is discussed and the problem size of the CASTOR3D code is optimized accordingly.

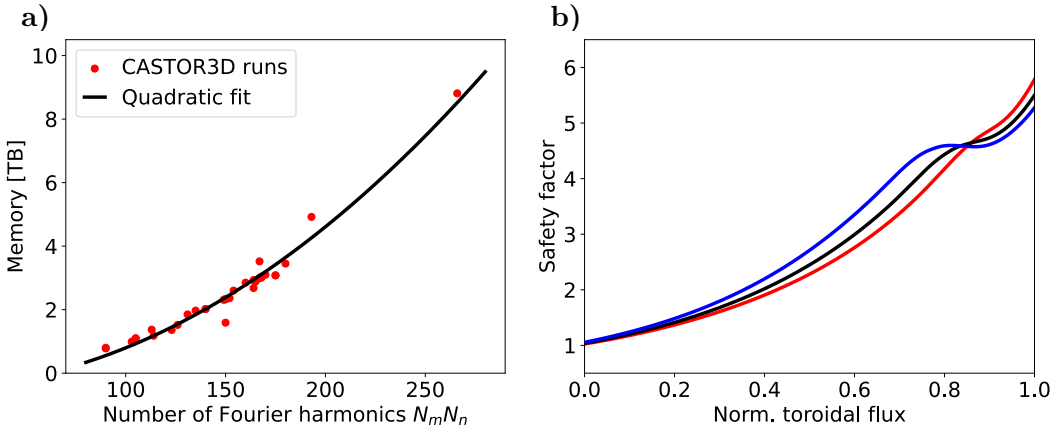

Figure 3.4: a) Memory required to solve the linear eigenvalue problem for $N_j = 251$ flux surfaces and different amounts of Fourier harmonics. b) Typical safety factor profiles for H-mode tokamak plasmas modelled with IPED2.

As discussed in section 2.3.5, in straight field line coordinates, harmonics which fulfill the resonance condition minimize field line bending at their respective resonant surface. For this reason, at a certain radial location s, instabilities consist mainly of harmonics (m, n) which are close to the resonant harmonic, defined by

$$m_{\text{res}}(s) = n\, q(s) \tag{3.3}$$

Thus, for a given toroidal mode number n, a natural choice for the poloidal mode number spectrum $m(s)$ at a certain radial location s is given by

$$m_{\text{res}}(s) - \Delta m \leqslant m(s) \leqslant m_{\text{res}}(s) + \Delta m \tag{3.4}$$

where the range of poloidal mode numbers Δm takes the coupling of poloidal harmonics into account. Since the edge of tokamak plasmas is usually strongly shaped, the range of poloidal mode numbers required to describe edge localized instabilities at a certain flux surface is typically about $\Delta m = 20 - 30$. In comparison to stellarators, tokamak plasmas feature a strong variation of the safety factor across the plasma radius, increasing from values slightly above 1 at the axis to values of about 5 or higher at the LCFS. Typical safety factor profiles for H-mode tokamak plasma are shown in figure 3.4b. The variation of the safety factor is usually strongest near the plasma edge. In previous versions of CASTOR3D, the set of Fourier harmonics (m, n) used in the ansatz for the eigenfunction 2.22 was the same for all flux surfaces. Consequently, according to equation 3.4, a large amount of different poloidal mode numbers N_m is required to describe edge localized instabilities in tokamaks:

$$N_m \approx n\Delta q + 2\Delta m \quad \Rightarrow \quad \text{Mem} \sim (n\Delta q + 2\Delta m)^2 \tag{3.5}$$

where Δq is the variation of the safety factor across the radial extent of the instability. This is no issue for stellarators and for core instabilities in tokamaks, for which there is usually little variation of the safety factor $\Delta q < 1$. However, for edge localized instabilities in tokamaks, for which the variation of the safety factor can be about $\Delta q \approx 4$ or higher, the amount of poloidal harmonics and the memory consumption increase quickly for high toroidal mode numbers. For this reason, as a part of this thesis, the CASTOR3D code was modified to allow the set of Fourier harmonics to be dependent on the flux surface. Consequently, only the harmonics described in 3.4 need to be considered at each flux surface s, reducing the size of the eigenvalue problem according to

$$N_m = 1 + 2\Delta m \quad \Rightarrow \quad \text{Mem} \sim (1 + 2\Delta m)^2 \tag{3.6}$$

which is independent of $n\Delta q$. The Fourier decomposition for an instability calculated with the previous and optimized versions of CASTOR3D is shown in figure 3.5. The Fourier decompositions and growth rates are identical. However, only half the poloidal harmonics and a quarter of the memory are required with the optimized version. In addition, the optimized version omits numerical noise by excluding harmonics that should have vanishing contribution to the Fourier decomposition. The impact of these improvements increases quickly for higher toroidal harmonics.

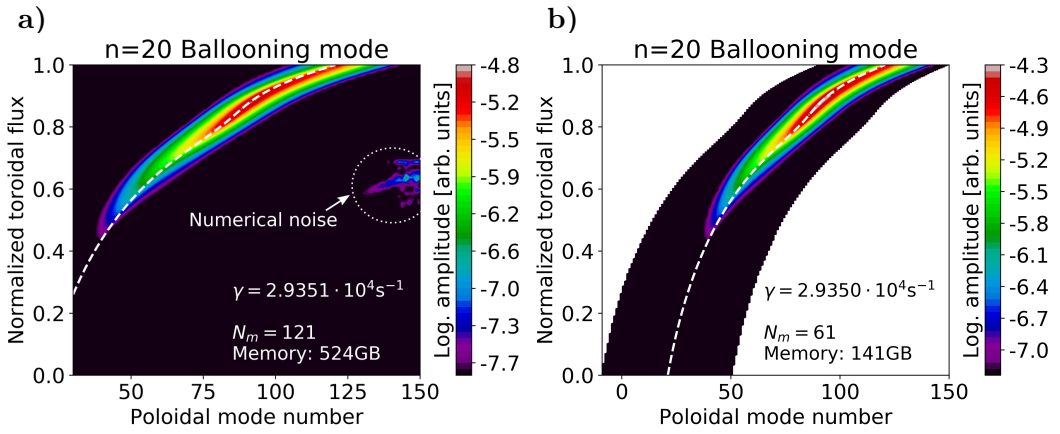

Figure 3.5: Fourier harmonics (logarithmic amplitude) for an $n = 20$ ballooning mode calculated using the original (a) and optimized (b) version of CASTOR3D. The dashed white lines indicate the resonant poloidal harmonics. Only harmonics in the filled (non-white) area of the plot are used for the ansatz 2.22.

Further reduction of the memory can be obtained for high-n edge localized instabilities by omitting a range of flux surfaces in the core. For this reason the possibility to crop the plasma core was implemented in CASTOR3D. This is equivalent to setting the eigenfunctions to zero within the cropped interval. For the instability shown in figure 3.5, one could omit the flux surfaces with a normalized toroidal flux $s < 0.3$. This method must be applied carefully since setting the cutoff too close to the pedestal can impact the instability. In addition, cropping the core plasma only saves a small amount of memory, since typically a low radial resolution is chosen for the core. However, in some cases the small additional reduction might allow further toroidal harmonics to be included or the radial resolution in the region of interest to be increased.

Furthermore, a new radial mesh has been introduced which features grid points at and in between the resonant surfaces for a specific toroidal mode number n. While this grid naturally resolves instabilities in axisymmetric plasmas perfectly using a minimal amount of radial grid points, it is not suitable for non-axisymmetric plasmas since - in this case - multiple toroidal harmonics are coupled together and the grid favors only a single toroidal mode number. This new mesh was used to resolve the ballooning mode shown in figure 2.5 (page 18). For edge localized instabilities in non-axisymmetric plasmas, piece-wise equidistant radial grids, where the resolution in each section is chosen to be roughly proportional to the amount of resonant flux surfaces in the section, seem to be currently the best choice. Both the resonant surface grid and the piece-wise equidistant grid share the property of flattening the safety factor profile. While new radial grids have been implemented in CASTOR3D, previous versions already supported non-uniform grids.

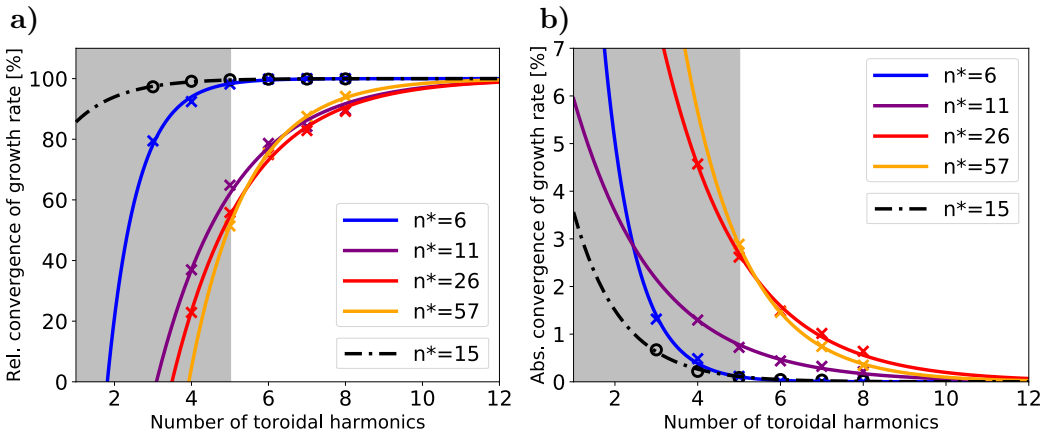

Figure 3.6: Relative convergence γ/γ_∞ (a) and absolute convergence $\gamma_\infty - \gamma$ (b) of the growth rate γ, which has been normalized with respect to the Alfvén time, with an increasing amount of toroidal harmonics for different dominating toroidal mode numbers n^*. The colored crosses belong instabilities close to the stability threshold studied in chapter 6, while the black circles belong to the test equilibrium discussed in chapter 5. The lines indicate exponential convergence fits, defining the limit γ_∞. The gray area indicates the range of toroidal harmonics that could be considered for edge localized instabilities with previous versions of CASTOR3D.

In conclusion, the implementation of local sets of Fourier harmonics and new radial grids provides an efficient description of edge localized instabilities, minimizing the required computational resources. This allows a maximum amount of toroidal harmonics to be considered in the stability analysis and, hence, enables the study of edge localized instabilities in non-axisymmetric tokamak plasmas. This is demonstrated

in figure 3.6, which shows the necessity of improvements allowing for the increase of the amount of toroidal harmonics included in the stability analysis in order to achieve convergence of edge localized instabilities, especially for equilibria close to the stability boundary (colored crosses/lines) or for instabilities of high dominating toroidal mode number n^*. The implementation of the flux-surface dependent Fourier decomposition required structural changes in almost all parts of the code, including for example the reassembly of the Fourier decomposition of the instability from the solution vector or the building of the matrix which describes the eigenvalue problem, since every subblock of the matrix has now a separate Fourier decomposition.

3.4 Further extensions of the CASTOR3D framework

More than 40 physical quantities, which are calculated in general curvilinear coordinates from the eigenfunctions, have been implemented into the diagnostic part of the CASTOR3D code and are available on radial, poloidal and toroidal cross-sections or the full plasma volume. These quantities include the various energy terms, discussed in chapter 4, perturbed current densities as well as perturbed magnetic and electric field components, and yield additional information on the numerically determined instabilities. The newly implemented quantities and visualization routines support the physical interpretation of the eigenfunctions and are the base for the analysis of the localization of instabilities as demonstrated in chapters 5 and 6.

Finally, the CASTOR3D framework was extended by the calculation of the neoclassical resistivity [56], providing a realistic model for the plasma resistivity in tokamak geometry. The implemented neoclassical resistivity has been applied to the interpretative stability analysis of an experimental discharge featuring edge localized resistive MHD instabilities in chapter 6 of *B. Vanovac, J. Puchmayr, et. al. (2023)* [57]. The numerical studies of the resistive edge localized instabilities in Ref. [57] were enabled by the optimizations presented in this chapter and reveal the influence of various physical effects such as parallel viscosity, gyroviscosity and equilibrium flow on growth rates and frequencies of MHD instabilities. While the work in Ref. [57] is focused on axisymmetric tokamak plasmas, studies of axisymmetric plasmas are the base for the analysis of non-axisymmetric tokamak equilibria.

4 Energy decomposition of resistive plasma perturbations

While the MHD stability of fusion plasmas is often well-described by ideal MHD, finite resistivity affects the stability of some equilibria significantly. In addition, there are types of instability that only exist in plasmas with finite resistivity. In the following, the intuitive energy functional of flow-free ideal MHD [38, 49], defined in equations 2.32 to 2.34, is extended to resistive perturbations. Furthermore, the ideal as well as the newly derived resistive contributions to the energetic decomposition are implemented in the CASTOR3D code. The resulting resistive energy functional is not in the form of a solvable eigenvalue problem but is intended to analyze the energetic composition of eigenfunctions which were calculated in advance by solving the linearized MHD equations. The energetic decomposition of the perturbations contributes to their physical interpretation and understanding and allows one to distinguish between e.g. current-density and pressure-gradient driven instabilities. There are also energy principles for resistive MHD [59, 60] which are meant to determine stability criteria or evaluate stability but do not provide information on the different contributions to the perturbed energy.

As discussed in section 2.3.4, the ideal energy principle is based on the minimization of the energy functional δW which represents the potential energy of a perturbation [38]. In general, the definition of a potential energy is not possible for MHD, since the MHD force is not a conservative force and no force potential exists. However, the restriction to linear perturbations causes the work integral to become effectively path-independent and, hence, the obtained energy functional only depends on the current state of the plasma perturbation. For this reason, we will keep the term "potential energy" for the resistive energy functional. Extending the linear ideal MHD equation 2.28 by including finite resistivity results in:

$$\rho_0\lambda^2\boldsymbol{\xi} = \boldsymbol{\nabla}(\boldsymbol{\xi}\cdot\boldsymbol{\nabla}p_0) + \boldsymbol{\nabla}(p_0\Gamma(\boldsymbol{\nabla}\cdot\boldsymbol{\xi})) + \frac{1}{\mu_0}(\boldsymbol{\nabla}\times\boldsymbol{B}_0)\times\boldsymbol{B}_1 + \frac{1}{\mu_0}(\boldsymbol{\nabla}\times\boldsymbol{B}_1)\times\boldsymbol{B}_0 \quad (4.1)$$

$$\boldsymbol{B}_1 = \boldsymbol{\nabla}\times(\boldsymbol{\xi}\times\boldsymbol{B}_0) - \lambda^{-1}\boldsymbol{\nabla}\times(\frac{\eta}{\mu_0}\boldsymbol{\nabla}\times\boldsymbol{B}_1) \quad (4.2)$$

In contrast to ideal MHD, equation 4.1 can no longer be written purely in terms of $\boldsymbol{\xi}$ by inserting 4.2 in 4.1. In order to get an expression for the plasma energy δW, we multiply the displacement $\frac{1}{2}\boldsymbol{\xi}^*$ of the perturbation with the restoring force defined by equation 4.1, which results in an energy density, and integrate the product over the plasma volume V. This is the common approach to derive the general complex energy functional δW. It should be noted that the energy densities related to the complex energy functional are not the physical energy densities of the real perturbation $\boldsymbol{\xi}_r = \mathrm{Re}(\boldsymbol{\xi})$. However, the physical energies and energy densities of δW are easily obtained from the complex energy functional by taking the real part of all complex quantities and all complex-conjugate quantities, separately. This is because the physical work done by the real displacement $\boldsymbol{\xi}_r$ is obtained by its multiplication with the physical restoring force $\mathrm{Re}(\lambda^2\boldsymbol{\xi})$. An example for deducing the physical energy density of the complex functional δW is given at the end of this section.

To form the resistive energy functional, we apply cyclic rotation and integration by parts to the last term of equation 4.1, resulting in:

$$G \equiv \int (\boldsymbol{\nabla} \times \boldsymbol{B}_1) \times \boldsymbol{B}_0 \cdot \boldsymbol{\xi}^* \mathrm{dV} = -\int \boldsymbol{\nabla} \times (\boldsymbol{\xi}^* \times \boldsymbol{B}_0) \cdot \boldsymbol{B}_1 \mathrm{dV} - \oint \boldsymbol{B}_1 \times (\boldsymbol{\xi}^* \times \boldsymbol{B}_0) \cdot \boldsymbol{n} \mathrm{dS} \tag{4.3}$$

Inserting 4.2, integrating by parts and using some vector algebra results in:

$$\begin{aligned} -\frac{G}{\mu_0} = &\int \frac{1}{\mu_0} \|\boldsymbol{B}_1\|^2 + \frac{\eta}{\mu_0^2 \lambda^*} \|\boldsymbol{\nabla} \times \boldsymbol{B}_1\|^2 \mathrm{dV} \\ &+ \oint \frac{\eta}{\mu_0^2 \lambda^*} (\boldsymbol{\nabla} \times \boldsymbol{B}_1^*) \cdot (\boldsymbol{B}_1 \times \boldsymbol{n}) + \frac{1}{\mu_0} (\boldsymbol{B}_1 \cdot \boldsymbol{B}_0)(\boldsymbol{\xi}^* \cdot \boldsymbol{n}) \mathrm{dS} \end{aligned} \tag{4.4}$$

Finally, integration by parts of the pressure-dependent terms in 4.1 yields an expression for the energy functional similar to Bernstein et al. [38]:

$$-\int \rho_0 \lambda^2 \|\boldsymbol{\xi}\|^2 \mathrm{dV} = 2\delta W = 2\delta W_V + 2\delta W_B \tag{4.5}$$

where

$$\begin{aligned} 2\delta W_V &= W_{\mathrm{MAG}} + W_{\mathrm{JXB}} + W_{\mathrm{RCD}} + W_{\mathrm{SND}} + W_{\mathrm{DP,C}} \\ 2\delta W_B &= W^{\mathrm{s}}_{\mathrm{MAG}} + W^{\mathrm{s}}_{\mathrm{RES}} + W^{\mathrm{s}}_{\mathrm{PRE}} + W^{\mathrm{s}}_{\mathrm{DP}} \end{aligned} \tag{4.6}$$

with the volume energy contributions δW_V

$$\begin{aligned} W_{\mathrm{MAG}} &= \frac{1}{\mu_0} \int \|\boldsymbol{B}_1\|^2 \mathrm{dV} & W_{\mathrm{JXB}} &= -\frac{1}{\mu_0} \int (\boldsymbol{\nabla} \times \boldsymbol{B}_0) \times \boldsymbol{B}_1 \cdot \boldsymbol{\xi}^* \mathrm{dV} \\ W_{\mathrm{RCD}} &= \frac{1}{\mu_0^2 \lambda^*} \int \eta \|\boldsymbol{\nabla} \times \boldsymbol{B}_1\|^2 \mathrm{dV} & W_{\mathrm{SND}} &= \Gamma \int p_0 |\boldsymbol{\nabla} \cdot \boldsymbol{\xi}|^2 \mathrm{dV} \\ W_{\mathrm{DP,C}} &= \int (\boldsymbol{\xi} \cdot \boldsymbol{\nabla} p_0)(\boldsymbol{\nabla} \cdot \boldsymbol{\xi}^*) \mathrm{dV} \end{aligned} \tag{4.7}$$

and boundary contributions δW_B

$$\begin{aligned} W^{\mathrm{s}}_{\mathrm{MAG}} &= \frac{1}{\mu_0} \oint (\boldsymbol{B}_1 \cdot \boldsymbol{B}_0)(\boldsymbol{\xi}^* \cdot \boldsymbol{n}) \mathrm{dS} & W^{\mathrm{s}}_{\mathrm{RES}} &= \frac{1}{\mu_0^2 \lambda^*} \oint \eta (\boldsymbol{\nabla} \times \boldsymbol{B}_1^*) \cdot (\boldsymbol{B}_1 \times \boldsymbol{n}) \mathrm{dS} \\ W^{\mathrm{s}}_{\mathrm{PRE}} &= -\Gamma \oint p_0 (\boldsymbol{\nabla} \cdot \boldsymbol{\xi})(\boldsymbol{\xi}^* \cdot \boldsymbol{n}) \mathrm{dS} & W^{\mathrm{s}}_{\mathrm{DP}} &= -\oint (\boldsymbol{\nabla} p_0 \cdot \boldsymbol{\xi})(\boldsymbol{\xi}^* \cdot \boldsymbol{n}) \mathrm{dS} \end{aligned} \tag{4.8}$$

Two resistive energy contributions appear in equation 4.5, the resistive current diffusion W_{RCD}, and a surface term $W^{\mathrm{s}}_{\mathrm{RES}}$, which is a correction to $W^{\mathrm{s}}_{\mathrm{MAG}}$. Combining $W^{\mathrm{s}}_{\mathrm{MAG}}$ and $W^{\mathrm{s}}_{\mathrm{RES}}$, we get:

$$W^{\mathrm{s}}_{\mathrm{EXB}} = W^{\mathrm{s}}_{\mathrm{MAG}} + W^{\mathrm{s}}_{\mathrm{RES}} = \frac{1}{\mu_0 \lambda^*} \oint \boldsymbol{E}_1^* \times \boldsymbol{B}_1 \cdot \boldsymbol{n} \mathrm{dS} \tag{4.9}$$

which describes a flow of electromagnetic energy through the plasma surface, the Poynting flux. The ideal volume contributions in equation 4.5 are related to the magnetic energy W_{MAG}, the Lorentz force W_{JXB}, adiabatic compression W_{SND} and compression against the pressure gradient $W_{\mathrm{DP,C}}$. The surface contributions always relate to a jump of a quantity at the plasma boundary. In the following, we bring the terms W_{MAG}, W_{JXB} and $W_{\mathrm{DP,C}}$ into their intuitive form, which separates current from pressure gradient drive, analogously to Ref. [49]. Splitting the equilibrium

current-density into a parallel $\boldsymbol{j}_{0,\parallel}$ and perpendicular $\boldsymbol{j}_{0,\perp}$ component with respect to the magnetic field $\boldsymbol{B}_0$ results in:

$$\begin{aligned} -W_{\mathrm{JXB}} = &\int \frac{j_{0,\parallel}}{\|\boldsymbol{B}_0\|}(\boldsymbol{\xi}^* \times \boldsymbol{B}_0)\cdot\boldsymbol{B}_1 \mathrm{dV} + \int \frac{1}{\boldsymbol{B}_0^2}(\boldsymbol{B}_1\cdot\boldsymbol{B}_0)(\boldsymbol{\nabla} p_0\cdot\boldsymbol{\xi}^*)\mathrm{dV} \\ &- \int \frac{1}{\boldsymbol{B}_0^2}(\boldsymbol{B}_1\cdot\boldsymbol{\nabla} p_0)(\boldsymbol{B}_0\cdot\boldsymbol{\xi}^*)\mathrm{dV} \end{aligned} \tag{4.10}$$

with $j_{0,\parallel} = (\boldsymbol{j}_0\cdot\boldsymbol{B}_0)/\|\boldsymbol{B}_0\|$. Analogously, we split the divergence $\boldsymbol{\nabla}\cdot\boldsymbol{\xi}$ in $W_{\mathrm{DP,C}}$ into $\boldsymbol{\nabla}\cdot\boldsymbol{\xi}_\parallel$ and $\boldsymbol{\nabla}\cdot\boldsymbol{\xi}_\perp$. After some vector algebra and integration by parts, we get:

$$\boldsymbol{B}_0^2\boldsymbol{\nabla}\cdot\boldsymbol{\xi}_\perp = \mu_0\,\boldsymbol{\xi}_\perp\cdot\boldsymbol{\nabla} p_0 - 2\boldsymbol{B}_0^2(\boldsymbol{\xi}_\perp\cdot\boldsymbol{\kappa}) - \boldsymbol{B}_0\cdot\boldsymbol{B}_1 - \boldsymbol{B}_0\cdot\boldsymbol{B}_R \tag{4.11}$$

$$-\int(\boldsymbol{\xi}\cdot\boldsymbol{\nabla} p_0)(\boldsymbol{\nabla}\cdot\boldsymbol{\xi}_\parallel^*)\mathrm{dV} = \int \frac{1}{\boldsymbol{B}_0^2}(\boldsymbol{B}_0\cdot\boldsymbol{\xi}^*)(\boldsymbol{B}_1\cdot\boldsymbol{\nabla} p_0) + \frac{1}{\boldsymbol{B}_0^2}(\boldsymbol{B}_0\cdot\boldsymbol{\xi}^*)(\boldsymbol{B}_R\cdot\boldsymbol{\nabla} p_0)\mathrm{dV} \tag{4.12}$$

where we introduce the self-induced ohmic field $\boldsymbol{B}_R = \lambda^{-1}\boldsymbol{\nabla}\times(\eta\boldsymbol{j}_1)$ and the equilibrium curvature vector $\boldsymbol{\kappa} = (\boldsymbol{b}\cdot\boldsymbol{\nabla})\boldsymbol{b}$ with $\boldsymbol{b} = \boldsymbol{B}_0/\|\boldsymbol{B}_0\|$. Note that for constant resistivity, we get $\boldsymbol{B}_R = \frac{\eta}{\mu_0\lambda}\Delta\boldsymbol{B}_1$ which describes resistive diffusion. Equations 4.11 and 4.12 relate the (work done by) parallel and perpendicular divergence of the plasma displacement to the (work done by the) magnetic perturbation using equation 4.2. In contrast to ideal MHD, the perturbed field generated by the displacement is changed by its self-induced ohmic field $\boldsymbol{B}_R$, which is taken into account by the corrective resistive terms in equations 4.11 and 4.12. Finally, combining equations 4.10 to 4.12 yields:

$$\begin{aligned} W_{\mathrm{MAG}} + W_{\mathrm{JXB}} + W_{\mathrm{DP,C}} = &\int \frac{1}{\mu_0}\left\|\boldsymbol{B}_1 - \boldsymbol{B}_0\frac{\mu_0\,\boldsymbol{\xi}_\perp\cdot\boldsymbol{\nabla} p_0}{\boldsymbol{B}_0^2}\right\|^2 \\ &- \frac{j_{0,\parallel}}{\|\boldsymbol{B}_0\|}(\boldsymbol{\xi}_\perp^*\times\boldsymbol{B}_0)\cdot\boldsymbol{B}_1 - 2(\boldsymbol{\xi}_\perp^*\cdot\boldsymbol{\kappa})(\boldsymbol{\xi}_\perp\cdot\boldsymbol{\nabla} p_0) \\ &- \frac{1}{\boldsymbol{B}_0^2}\Big[(\boldsymbol{\xi}_\perp\cdot\boldsymbol{\nabla} p_0)(\boldsymbol{B}_0\cdot\boldsymbol{B}_R^*) + (\boldsymbol{\xi}_\parallel^*\cdot\boldsymbol{B}_0)(\boldsymbol{\nabla} p_0\cdot\boldsymbol{B}_R)\Big]\mathrm{dV} \end{aligned} \tag{4.13}$$

Then, using 4.11 and 4.13, the intuitive form of the energy functional for resistive MHD reads:

$$\begin{aligned} 2\delta W_V = &\underbrace{\int \frac{\|\boldsymbol{B}_{1,\perp}\|^2}{\mu_0}\mathrm{dV}}_{W_{\mathrm{SHA}}} + \underbrace{\int \frac{\boldsymbol{B}_0^2}{\mu_0}\left|\boldsymbol{\nabla}\cdot\boldsymbol{\xi}_\perp + 2(\boldsymbol{\xi}_\perp\cdot\boldsymbol{\kappa}) + \frac{1}{\boldsymbol{B}_0^2}\boldsymbol{B}_0\cdot\boldsymbol{B}_R\right|^2\mathrm{dV}}_{W_{\mathrm{CPA}}} \\ &\underbrace{+\Gamma\int p_0|\boldsymbol{\nabla}\cdot\boldsymbol{\xi}|^2\mathrm{dV}}_{W_{\mathrm{SND}}} \qquad \underbrace{+\frac{1}{\mu_0^2\lambda^*}\int\eta\|\boldsymbol{\nabla}\times\boldsymbol{B}_1\|^2\mathrm{dV}}_{W_{\mathrm{RCD}}} \\ &\underbrace{-\int \frac{j_{0,\parallel}}{\|\boldsymbol{B}_0\|}(\boldsymbol{\xi}_\perp^*\times\boldsymbol{B}_0)\cdot\boldsymbol{B}_{1,\perp}\mathrm{dV}}_{W_{\mathrm{CUR}}} \qquad \underbrace{-\int 2(\boldsymbol{\xi}_\perp\cdot\boldsymbol{\nabla} p_0)(\boldsymbol{\xi}_\perp^*\cdot\boldsymbol{\kappa})\mathrm{dV}}_{W_{\mathrm{DP0}}} \\ &\underbrace{-\int \frac{1}{\boldsymbol{B}_0^2}(\boldsymbol{\xi}_\parallel^*\times\boldsymbol{\nabla} p_0)\cdot(\boldsymbol{B}_0\times\boldsymbol{B}_R)\mathrm{dV}}_{W_{\mathrm{RD},\parallel}} \quad \underbrace{-\int \frac{1}{\boldsymbol{B}_0^2}(\boldsymbol{\xi}_\perp\cdot\boldsymbol{\nabla} p_0)(\boldsymbol{B}_0\cdot\boldsymbol{B}_R^*)\mathrm{dV}}_{W_{\mathrm{RD},\perp}} \end{aligned} \tag{4.14}$$

where the first four terms are always stabilizing and relate to perpendicular magnetic perturbations W_{SHA}, parallel magneto-compressional perturbations W_{CPA}, adiabatic compression W_{SND} and resistive current diffusion W_{RCD}, respectively. The next two terms describe the parallel current density W_{CUR} and field-line-curvature dependent pressure gradient W_{DP0} drives, respectively. The last two terms are resistive corrections to the pressure gradient drive. They account for the effect of resistive diffusion on the work done by the induced magnetic perturbation that is generated by parallel $W_{\mathrm{RD},\parallel}$ and perpendicular $W_{\mathrm{RD},\perp}$ compression of the plasma, respectively. Finally, the resistive correction to the relation between perpendicular compression and its induced magnetic perturbation also appears in the stabilizing energy of magneto-compressional perturbations W_{CPA}. In summary, taking finite resistivity into account, there are three new volume contributions to the energy functional (W_{RCD}, $W_{\mathrm{RD},\parallel}$, $W_{\mathrm{RD},\perp}$) as well as a correction to the stabilizing energy of magneto-compressional perturbations (W_{CPA}). Note that resistive diffusion can affect the perturbation over a longer time-scale if the mode grows or oscillates slower, which is described by the inverse proportionality of the resistive energy terms with the eigenvalue of the perturbation.

In the following, we extend the energy functional to the vacuum region, analogously to Ref. [38]. The linearized boundary condition for the pressure balance 2.7 is not dependent on resistivity and remains unchanged:

$$\boldsymbol{B}_0 \cdot \boldsymbol{B}_1 - \mu_0 \Gamma p_0 (\boldsymbol{\nabla} \cdot \boldsymbol{\xi}) = \frac{1}{2} \boldsymbol{\xi} \cdot (\boldsymbol{\nabla} \check{\boldsymbol{B}}_0^2 - \boldsymbol{\nabla} \boldsymbol{B}_0^2) + \check{\boldsymbol{B}}_0 \cdot \check{\boldsymbol{B}}_1 \tag{4.15}$$

An additional boundary condition is obtained by combining Ohm's law 2.3 with the boundary condition for the tangential electric field 2.8:

$$-\boldsymbol{n} \times \check{\boldsymbol{A}}_1 = \frac{\eta}{\lambda} \boldsymbol{n} \times \boldsymbol{j}_1 + \check{\boldsymbol{B}}_0 (\boldsymbol{n} \cdot \boldsymbol{\xi}) \quad \text{with} \quad \check{\boldsymbol{A}}_1 = -\frac{1}{\lambda} \check{\boldsymbol{E}}_1 \tag{4.16}$$

resulting in a resistive correction on the right hand side. Applying equation 4.15 to $W^{\mathrm{s}}_{\mathrm{MAG}}$ and $W^{\mathrm{s}}_{\mathrm{PRE}}$ results in:

$$W^{\mathrm{s}}_{\mathrm{MAG}} + W^{\mathrm{s}}_{\mathrm{PRE}} = \oint \frac{1}{2\mu_0} (\boldsymbol{\xi}^* \cdot \boldsymbol{n}) \boldsymbol{\xi} \cdot [\![\boldsymbol{\nabla} \boldsymbol{B}_0^2]\!] \mathrm{dS} + \oint \frac{1}{\mu_0} (\boldsymbol{\xi}^* \cdot \boldsymbol{n}) (\check{\boldsymbol{B}}_1 \cdot \check{\boldsymbol{B}}_0) \mathrm{dS} \tag{4.17}$$

Adding the latter surface integral in equation 4.17 to $W^{\mathrm{s}}_{\mathrm{RES}}$ and using equation 4.16 yields:

$$\oint \frac{1}{\mu_0} (\boldsymbol{\xi}^* \cdot \boldsymbol{n}) (\check{\boldsymbol{B}}_1 \cdot \check{\boldsymbol{B}}_0) \mathrm{dS} + \oint \frac{\eta}{\mu_0 \lambda^*} \boldsymbol{j}_1^* \cdot (\boldsymbol{B}_1 \times \boldsymbol{n}) \mathrm{dS} = \int \frac{\| \check{\boldsymbol{B}}_1 \|^2}{\mu_0} \mathrm{d}\check{\mathrm{V}} + \oint \frac{\eta}{\lambda^*} \boldsymbol{j}_1^* \cdot \boldsymbol{K}_1 \mathrm{dS} \tag{4.18}$$

where we introduced the perturbed surface current $\boldsymbol{K}_1 = \mu_0^{-1} \boldsymbol{n} \times [\![\boldsymbol{B}_1]\!]$. However, surface currents cannot be maintained in resistive plasmas, i.e. $\eta \neq 0$ implies $\boldsymbol{K}_1 = 0$. This means that all components of the magnetic field must be continuous in resistive plasmas. Finally, combining equations 4.17 and 4.18 with $W^{\mathrm{s}}_{\mathrm{DP}}$, we get:

$$\delta W_B = \delta W_S + \delta W_{\check{V}} \tag{4.19}$$

with

$$2\delta W_S = \oint |\boldsymbol{n} \cdot \boldsymbol{\xi}|^2 \boldsymbol{n} \cdot \left[\!\!\left[\boldsymbol{\nabla} (p_0 + \frac{\boldsymbol{B}_0^2}{2\mu_0}) \right]\!\!\right] \mathrm{dS} \ , \ 2\delta W_{\check{V}} = \int \frac{\| \check{\boldsymbol{B}}_1 \|^2}{\mu_0} \mathrm{d}\check{\mathrm{V}} \tag{4.20}$$

As a result, no additional surface or vacuum energy contributions have to be considered in the case of finite resistivity. Note that $\delta W_S = 0$ if there are no equilibrium

surface currents, which is a common constraint on equilibria and is consistent with the resistive boundary conditions. However, in principle, one could allow for finite surface currents in an ideal equilibrium and test this equilibrium for resistive instabilities. In the case of vanishing surface current, the surface terms in equation 4.5 are equivalent to the vacuum energy of the perturbation, i.e. $\delta W_B = \delta W_{\check{V}} > 0$. While the vacuum contribution $\delta W_{\check{V}}$ provides a simpler, more accessible understanding of the perturbation energy outside the plasma, the surface contributions δW_B encode the vacuum energy in a single surface, which can be computationally advantageous. If there is a resistive wall or resistive components in the vacuum region, additional terms in equation 4.19 are required to take the interaction of the perturbation with the wall into account. These additional terms can be easily obtained from the divergence theorem applied in equation 4.18.

Finally, we demonstrate how to obtain the physical energies and energy densities from the complex terms of the resistive energy functional derived above. As discussed in the beginning of this chapter, one must take the real part of the complex and complex-conjugate quantities in order to obtain the physical energies. This is shown as an example for the energy density related to resistive current diffusion w_{RCD}:

$$w_{\mathrm{RCD}} = \frac{1}{\mu_0^2 \lambda^*}\eta \|\boldsymbol{\nabla}\times\boldsymbol{B}_1\|^2 \;\rightarrow\; \mathcal{P}\{w_{\mathrm{RCD}}\} = \frac{\eta}{\mu_0^2}\,\mathrm{Re}\left(\lambda^{-1}\boldsymbol{\nabla}\times\boldsymbol{B}_1\right)\cdot\mathrm{Re}\left(\boldsymbol{\nabla}\times\boldsymbol{B}_1\right) \overset{\text{if } \lambda\in\mathbb{R}}{=} \frac{\eta}{\mu_0^2\lambda}\mathrm{Re}\left(\boldsymbol{\nabla}\times\boldsymbol{B}_1\right)^2 \tag{4.21}$$

where $\mathcal{P}\{\dots\}$ denotes the physical energy or energy density, the lower case w_{RCD} denotes the energy density or integrand of the energy term W_{RCD}. Note that one must express the absolute values in terms of complex and complex-conjugate quantities before extracting the physical energy. The multiplication of solutions of the linear MHD equations with an arbitrary complex number yields equivalent solutions to the linear MHD equations, which results in a useful relation between the complex and physical energy densities:

$$\frac{1}{2}\mathrm{Re}(w_{\square}) = \frac{1}{2\pi}\int_0^{2\pi} \mathcal{P}\{w_{\square}\}\Big|_{\boldsymbol{\chi}\rightarrow\boldsymbol{\chi}e^{i\varphi}}\,\mathrm{d}\varphi \tag{4.22}$$

where φ is the solution phase, i.e. the arbitrary complex phase of the eigenfunction $\boldsymbol{\chi}$. In equation 4.22, the lower case $w_{\square}$ denotes the energy density or integrand of the energy term $W_{\square}$ and $\square$ is a placeholder for any energy density, e.g. $\square = \mathrm{RCD}$. Thus, the real-part of the complex energy densities is equivalent to two-times the solution phase average of the physical energy densities. Furthermore, the energy functional is related to the kinetic energy $\delta E_{kin} = \int \frac{1}{2}\rho_0\|\boldsymbol{v}_1\|^2\mathrm{dV}$ by:

$$\delta E_{kin} + \delta E_{osc} + \delta W = 0 \tag{4.23}$$

where the energy stored in the oscillation frequency is $\delta E_{osc} = -\int \omega^2\|\boldsymbol{\xi}\|^2\mathrm{dV}$. For the physical energies, we have $\mathcal{P}\{\delta E_{kin}\} = \int \frac{1}{2}\rho_0\,\mathrm{Re}(\boldsymbol{v}_1)^2\mathrm{dV}$ and $\mathcal{P}\{\delta E_{osc}\} = \frac{1}{2}\delta E_{osc}$. The oscillation energy is negligible if $\gamma \gg \omega$.

4.1 Numerical validation

The physical and complex terms of the intuitive form of the energy functional for ideal and resistive plasma perturbations have been implemented as a diagnostic for eigenfunctions in the CASTOR3D code. We validate the energy functional by comparison of potential and kinetic energy and of the energy contributions of δW over

three different coordinate systems: NEMEC coordinates (NEM) [61], 2D straight field line coordinates (SFL) [37], and Boozer coordinates (BZR) [50]. The following validation is based on an $n = 8$ edge-localized mode of a simple low-β axisymmetric equilibrium surrounded by an infinite vacuum region. The equilibrium was calculated using the NEMEC equilibrium code [40, 42].

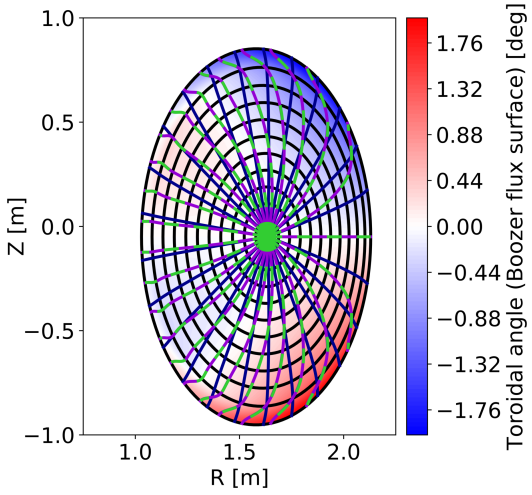

Figure 4.1: Toroidal cross-section with flux surfaces (black) and lines of constant poloidal coordinate for NEM (dark blue), SFL (purple) and BZR (green, dashed) coordinates; toroidal angle of the cross-section for BZR coordinates (background color, blue to red).

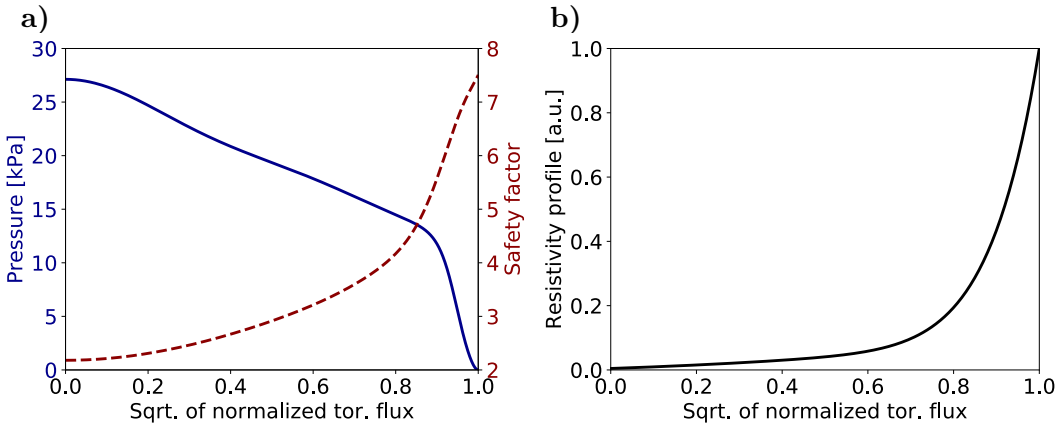

Figure 4.2: a) Equilibrium pressure profile (solid) and safety factor profile (dashed). b) Profile shape of the resistivity as defined in equation 4.24 normalized to $\eta(1) = 1$.

Figure 4.1 shows the flux surfaces and lines of constant poloidal coordinate u of the validation case for a toroidal cross-section, i.e. constant toroidal coordinate v, in the different coordinate systems. One can see that the lines of constant poloidal coordinates are equal for SFL and BZR coordinates. However, the toroidal cross-section in SFL coordinates is planar in cylindrical coordinates, while in BZR coordinates it is deformed and extends over multiple toroidal angles Φ. The equilibrium pressure and safety factor profiles (see [62]) of the validation case are displayed in figure 4.2a. For the resistivity, a polynomial profile that is small in the plasma-core and large at the edge is used:

$$\eta(\rho_{\text{tor}}) = \eta_0 \cdot (1 + 10\rho_{\text{tor}} + 10\rho_{\text{tor}}^2 + 100\rho_{\text{tor}}^8 + 100\rho_{\text{tor}}^{10}) \tag{4.24}$$

where ρ_{tor} is the square-root of the normalized toroidal flux. The shape of this resistivity profile is shown in figure 4.2b. In the following, all energies and energy densities are normalized w.r.t. $\int \tau_A^{-2} \rho \|\boldsymbol{\xi}\|^2 \mathrm{dV}$ where $\tau_A = \frac{\sqrt{\mu_0 \rho_{\text{ax}}} R_{\text{ax}}}{B_{\text{ax}}}$ is the Alfvén time, R_{ax} is the major radius and the subscript "ax" denotes equilibrium quantities

at the magnetic axis. For the physical energies and energy densities, the normalization factor naturally becomes $\int \tau_A^{-2} \rho \, \mathrm{Re}(\boldsymbol{\xi})^2 \mathrm{dV}$. This ensures comparability of the energy between eigenfunctions, since the amplitude of the perturbation is arbitrary in linear MHD.

Coordinate system		NEM	SFL	BZR	BZR
Pol. mode numbers		6 - 105	20 - 75	20 - 90	20 - 70
W_{SHA}	$[10^{-2}]$	5.93	5.93	5.93	5.92
W_{CPA}	$[10^{-6}]$	4.03	4.04	4.11	4.10
W_{SND}	$[10^{-3}]$	1.54	1.54	1.54	1.54
W_{DP0}	$[10^{-2}]$	-5.14	-5.15	-5.15	-5.14
W_{CUR}	$[10^{-2}]$	-4.03	-4.04	-4.03	-4.02
W_{RCD}	$[10^{-3}]$	5.08	5.04	5.13	**111**
$W_{\mathrm{RD},\perp}$	$[10^{-4}]$	-1.98	-1.98	-1.98	-6.77
$W_{\mathrm{RD},\parallel}$	$[10^{-6}]$	-5.49	-5.50	-5.51	-5.70
Vacuum energy $\delta W_{\tilde{V}}$	$[10^{-3}]$	9.84	9.83	9.83	9.76
Potential energy δW	$[10^{-2}]$	-1.61	-1.63	-1.62	8.88
Kinetic energy λ^2	$[10^{-2}]$	1.61	1.61	1.61	1.61
Deviation $(\delta W + \lambda^2)/(-\lambda^2)$	[%]	-0.06	0.91	0.37	**-651**

Table 4.1: Normalized potential energy contributions calculated in the different coordinate systems and numerical deviation of the potential and kinetic energies.

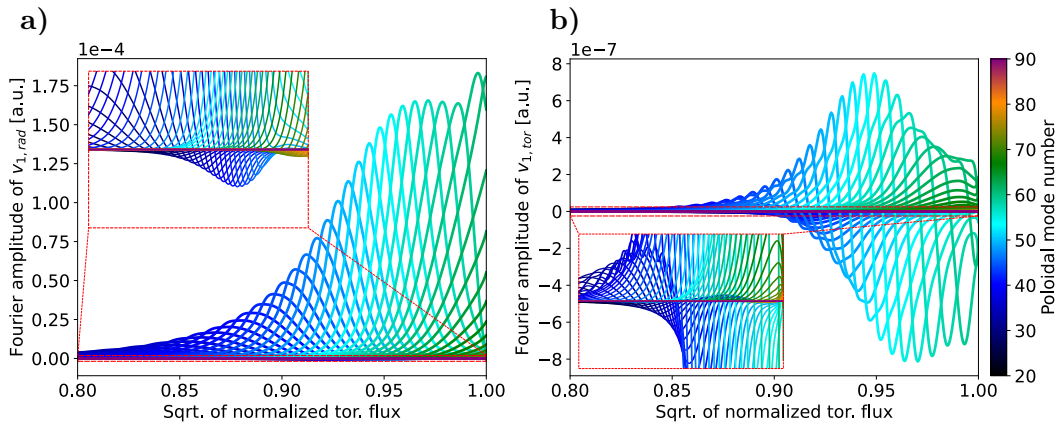

Figure 4.3: Fourier spectra ($m = 20 - 90$) of the radial (a) and toroidal (b) velocity perturbation $\boldsymbol{v}_1$ in BZR coordinates for the $n = 8$ eigenfunction and a resistivity of $\eta_0 = 10^{-8}$ Ωm.

Table 4.1 shows the potential energy contributions of the $n = 8$ eigenfunction for a resistivity of $\eta_0 = 10^{-8}$ Ωm. The Fourier spectra in BZR coordinates of the radial and toroidal velocity perturbation for this eigenfunction are displayed in figure 4.3. In order to resolve the eigenfunction, different sets of poloidal mode numbers are required for each coordinate system. From comparison of the last two columns of table 4.1, one can see that the kinetic energy, i.e. the eigenvalue, eventually converges much faster with respect to the number of poloidal modes than some of the energy terms, especially the resistive current diffusion term W_{RCD} which depends on $\boldsymbol{\nabla} \times \boldsymbol{B}_1$. This leads to the large difference of kinetic and potential energy for the BZR coordinates with the small set of poloidal mode numbers $m = 20 - 70$. While for BZR coordinates, the spectrum $m = 20 - 70$ is probably sufficient to solve the

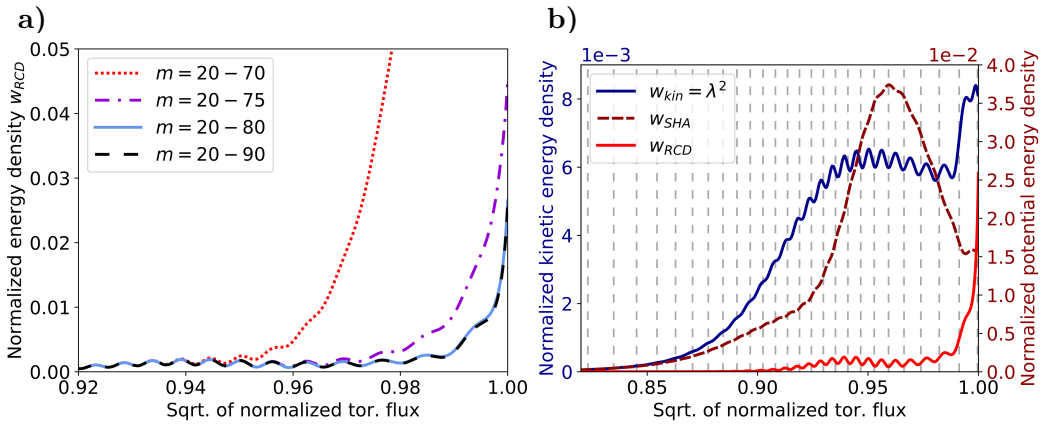

Figure 4.4: a) Normalized energy density w_{RCD} for poloidal mode numbers $m = 20 - 70$ (red), $m = 20 - 75$ (purple), $m = 20 - 80$ (blue) and $m = 20 - 90$ (black) in BZR coordinates. b) Normalized kinetic energy density (dark blue) and normalized potential energy densities w_{RCD} (red) and w_{SHA} (dark red) in BZR coordinates and resonant surfaces (light gray, dashed).

numerical eigenvalue problem for the growth rate of the mode, some derivatives of the eigenfunction can still be poorly resolved. Figure 4.4a shows the convergence of the radially resolved energy density w_{RCD} for different sets of poloidal mode numbers. The radial resolution of the eigenfunction must also be large enough to resolve the behavior of the potential energy densities at the resonant flux surfaces. The radially resolved energy densities can vary strongly near these resonant surfaces, as can be seen in figure 4.4b.

As one can see in table 4.1, the kinetic and potential energy as well as the different energy contributions match well for all coordinate systems provided that sufficient poloidal resolution has been chosen. The numerical equality of potential and kinetic energy validates that all energy contributions have been considered, while the numerical equality between the coordinate systems validates the implementation in general curvilinear 3D coordinates. Note that in order to get such a high accuracy of the energy functional over different coordinate systems requires not only a sufficient radial and poloidal resolution of the eigenfunction but also a highly resolved force equilibrium.

4.2 Influence of finite resistivity

In the following, we investigate the influence of increasing resistivity on the potential energy composition of the eigenfunction for the validation case. In order to estimate the effect of the resistive corrections with increasing resistivity, we define the following potential energy proportions:

$$\chi^{\mathrm{s}}_{\mathrm{RES}} = \frac{|W^{\mathrm{s}}_{\mathrm{RES}}|}{|W^{\mathrm{s}}_{\mathrm{MAG}}| + |W^{\mathrm{s}}_{\mathrm{RES}}|} \ , \quad \chi_{\mathrm{RCD}} = \frac{W_{\mathrm{RCD}}}{W_{\mathrm{RCD}} + W_{\mathrm{SHA}} + W_{\mathrm{CPA}} + W_{\mathrm{SND}}} \tag{4.25}$$

$$\chi_{\mathrm{RD}} = \frac{W_{\mathrm{RD},\perp} + W_{\mathrm{RD},\parallel}}{W_{\mathrm{RD},\perp} + W_{\mathrm{RD},\parallel} + W_{\mathrm{DP0}}} \tag{4.26}$$

with the proportion of the resistive correction relative to the surface or vacuum energy $\chi^{\mathrm{s}}_{\mathrm{RES}}$, to the stabilizing energy terms χ_{RCD} and to the pressure-gradient

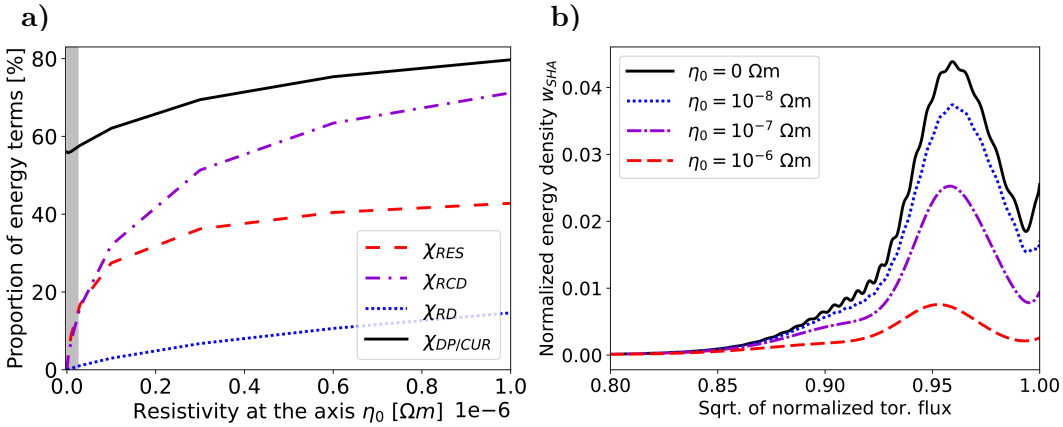

Figure 4.5: a) Proportions of the resistive corrections w.r.t. the energy terms $\chi^{\mathrm{s}}_{\mathrm{RES}}$ (red), χ_{RCD} (purple) and χ_{RD} (blue) as well as the ratio of pressure-gradient to current-density drive $\chi_{\mathrm{DP/CUR}}$ (black); the gray area indicates the range of realistic resistivity values. b) Magnetic energy density of the perpendicular perturbation w_{SHA} for resistivity values of $\eta_0 = 0\,\Omega\mathrm{m}$ (black), $\eta_0 = 10^{-8}\,\Omega\mathrm{m}$ (blue), $\eta_0 = 10^{-7}\,\Omega\mathrm{m}$ (purple) and $\eta_0 = 10^{-6}\,\Omega\mathrm{m}$ (red).

drive χ_{RD}. We also define the ratio of pressure-gradient drive to the destabilizing terms:

$$\chi_{\mathrm{DP/CUR}} = \frac{W_{\mathrm{RD},\perp} + W_{\mathrm{RD},\parallel} + W_{\mathrm{DP0}}}{W_{\mathrm{RD},\perp} + W_{\mathrm{RD},\parallel} + W_{\mathrm{DP0}} + W_{\mathrm{CUR}}} \tag{4.27}$$

The newly defined energy proportions are shown in figure 4.5a. One can see that the surface correction $W^{\mathrm{s}}_{\mathrm{RES}}$ (red) and the resistive current diffusion W_{RCD} (purple) become important even for small values of resistivity, while the relative correction to the pressure drive $W_{\mathrm{RD},\perp} + W_{\mathrm{RD},\parallel}$ (blue) only increases slowly with increasing resistivity. Note that the validation case is ideally unstable and the effect of the correction $W_{\mathrm{RD},\perp} + W_{\mathrm{RD},\parallel}$ might be larger for purely resistive modes. Moreover, the relative effect of the corrections on the growth rate is often larger compared to the effect of the corrections on the related energy terms because the growth rate is given by the sum of the energy terms which might be smaller than its summands. Finally, from the ratio of pressure to current drive $\chi_{\mathrm{DP/CUR}}$ (black curve in figure 4.5a) it can be seen that the eigenfunction becomes increasingly pressure-gradient driven for increasing resistivity.

Figure 4.5b shows the radially resolved perpendicular magnetic energy density w_{SHA} for different values of resistivity. The radial structure of the magnetic perturbation becomes less sensitive to resonant surfaces and the maximum of the magnetic perturbation shifts inwards with increasing resistivity. In addition, the poloidal localization of the potential energy contributions is affected by resistivity as can be seen in figure 4.6 which shows the energy density corresponding to the pressure-gradient drive. With increasing resistivity, the pressure drive of the eigenfunction becomes at first slightly less localized at the low-field side compared to the ideal mode, which can be seen from the relative increase of the energy density in the upper, lower and high-field side regions of the plasma. Further increasing the resistivity causes the energy density of the pressure drive to move to the upper and lower regions of the plasma, away from the midplane. Furthermore, it can be seen that the eigenfunction is weakly stabilized (magenta regions in figure 4.6) by the pressure-gradient on the high-field side and at some locations on the low-field-side. We note here that such trends can also be seen for resistive modes at realistic resistivity values.

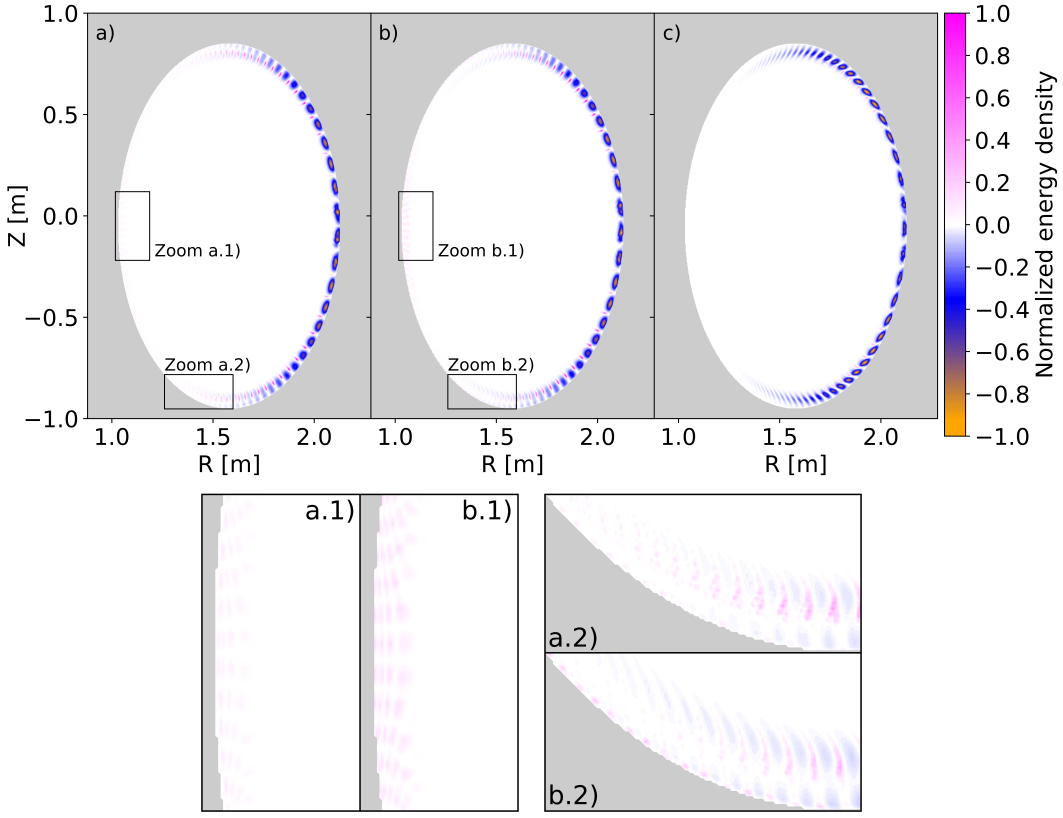

Figure 4.6: Energy density of the pressure-gradient drive including resistive corrections ($w_{\mathrm{DP0}} + w_{\mathrm{RD},\perp} + w_{\mathrm{RD},\parallel}$) for resistivity values of $\eta_0 = 0$ Ωm (a), $\eta_0 = 10^{-8}$ Ωm (b) and $\eta_0 = 10^{-6}$ Ωm (c). The color range is normalized with respect to the maximum and minimum energy densities for each plot separately and the color scale is linear in the intervals $[-1, 0]$ and $[0, 1]$. The minimum normalized energy densities are: $w_{\mathrm{DP}}^{\mathrm{min}} = -1.132$ (a), $w_{\mathrm{DP}}^{\mathrm{min}} = -1.029$ (b), $w_{\mathrm{DP}}^{\mathrm{min}} = -1.427$ (c); the maximum normalized energy densities are: $w_{\mathrm{DP}}^{\mathrm{max}} = 0.033$ (a), $w_{\mathrm{DP}}^{\mathrm{max}} = 0.027$ (b), $w_{\mathrm{DP}}^{\mathrm{max}} = 0.073$ (c).

In conclusion, the resistive corrections can significantly affect the energy contributions of the ideal energy functional for realistic values of the resistivity and trends in the localization of the energy density with increasing resistivity were presented, where, with increasing resistivity, the perturbation moves away from the midplane. The energy functional grants increased insight into the different energetic drives and stabilising phenomena of linear perturbations compared to trends in growth rates and perturbed quantities and, hence, contributes to the physical understanding of these perturbations. The newly implemented functional is used in chapter 5 to obtain a physical understanding of the localization and locking of ideal MHD instabilities in non-axisymmetric tokamak plasmas and has been applied to classify resistive modes in Ref. [34].

5 Helical localization and mode locking of ideal MHD instabilities in non-axisymmetric equilibria

Experimental observations show that the application of a MP field causes inter-ELM modes, i.e. MHD instabilities that grow in between two ELM bursts, and the ELM onset to appear in certain helical positions (at certain toroidal phase angles) instead of being randomly located along the toroidal direction [24]. The toroidal mode localization for infinite-n ballooning modes, which are located at a single flux surface, was studied analytically by [30]. The helical localization of intermediate to high toroidal mode number peeling-ballooning modes in non-axisymmetric tokamak plasmas in the limit of weak MP fields (perturbative stability analysis) was investigated by [31]. Further research investigated the impact of MPs on the MHD stability limit, but has not analyzed the localization of the instabilities [28, 29]. In this chapter, we focus on the helical localization of general ideal MHD instabilities at the edge in magnetically perturbed tokamak plasmas of arbitrary MP field strength using the CASTOR3D code. In addition, we study mode locking of MHD instabilities, which describes a state in which instabilities remain in their position even if the background plasma rotates at a finite velocity, in non-axisymmetric tokamak plasmas.

The phenomenon of helical mode localization is analyzed for a simplified MHD equilibrium (section 5.1). A systematical differentiation between two kinds of helical mode localization, strictly locked and localized (quasi-locked) modes, is introduced. Furthermore, the effect of toroidal plasma rotation on the strictly locked and quasi-locked modes is studied, providing a physical interpretation of strict locking and quasi-locking (section 5.2). Strictly locked modes are shown to rotate non-uniformly above a critical plasma rotation, while quasi-locked modes are shown to rotate uniformly at any plasma rotation. Finally, the helical mode localization is studied for an experimental case and successfully compared to Electron Cyclotron Emission (ECE) measurements [24] (section 5.3). We show that the equilibrium is unstable to low mode number instabilities which are located at the same helical position as observed in the experiment.

5.1 Mode localization and mode locking for a numerical test equilibrium

In order to study helical mode localization and mode locking of ELMs, we begin with the analysis of a simple equilibrium. The simple equilibrium should have smooth plasma profiles, an intrinsically small size of the linear eigenvalue problem, and it should be unstable to edge localized instabilities of any toroidal mode number in the axisymmetric case, i.e. without application of a magnetic perturbation to the equilibrium.

The work presented in this section was carried out before the memory optimization

of CASTOR3D, which has been discussed in section 3.3. For this reason, the number of poloidal harmonics required to describe global MHD instabilities is roughly proportional to the range of safety factor values Δq over the plasma radius. To minimize the memory requirements for our test case and allow large toroidal mode numbers to be investigated, we choose a small but relevant value for the edge value of the safety factor:

$$q(\psi_N) = 1.1 + 2.15\psi_N^2 \tag{5.1}$$

where ψ_N is the normalized poloidal flux. Next, we use the IPED2 framework to create a model plasma boundary (major radius $R_0 = 1.66$ m, minor radius $a_0 = 0.6$ m, elongation $\kappa = 1.8$, triangularity $\delta = 0.4$), pressure profile (normalized plasma beta $\beta_\mathrm{N} = 1.54$, pedestal top pressure $p_\mathrm{ped} = 17.5$ kPa), and an electron density profile (pedestal top electron density $n_\mathrm{e,ped} = 5 \cdot 10^{19}$ m^{-3}) [51]. The toroidal flux at the plasma boundary is set to $\Phi_\mathrm{bnd} = -3.64$ Wb.

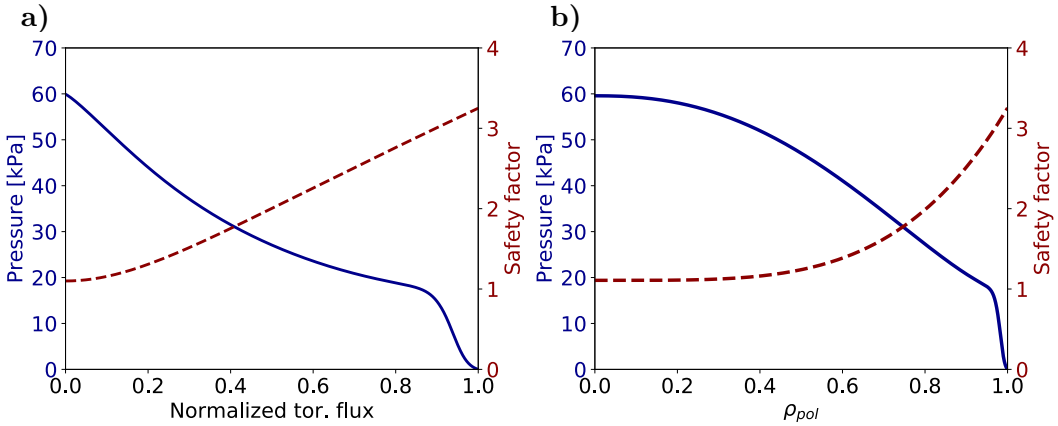

Figure 5.1: Pressure (dark blue) and safety factor (dark red) profiles for the numerical test case in toroidal flux coordinates (a) and as function of $\rho_\mathrm{pol} = \sqrt{\psi_N}$ (b)

.

The obtained set of plasma boundary, safety factor, pressure profile, and toroidal flux at the plasma boundary defines our numerical test equilibrium, which fulfills all properties described in the first paragraph of this section. Figure 5.1 shows the safety factor and pressure profile of the numerical test case. The profiles are shown in toroidal flux coordinates, which stretch the pedestal region and are numerically beneficial for the equilibrium convergence and stability analysis, as well as in $\rho_\mathrm{pol} = \sqrt{\psi_N}$ coordinates, usually used for tokamak profiles. The global plasma parameters of the resulting magnetic equilibrium are: plasma current $I_P = 1.75$ MA, toroidal magnetic field at the axis $B_T = 1.73$ T, total normalized plasma beta $\beta_\mathrm{N} = 1.47$ and pedestal beta poloidal $\beta_\mathrm{pol,ped} = 0.27$.

The growth rates of the axisymmetric equilibrium are listed in table 5.1. As desired, all instabilities have comparably large growth rates, which implies that the numerical test case is far above the stability boundary, i.e. far above marginal stability. The growth rate of every fourth mode number is damped because the edge safety factor multiplied by 4 is an integer, which causes the outermost resonant surface to be aligned with the boundary for $n/4 \in \mathbb{N}$. Finally, the energetic decomposition of the ideal MHD instabilities is calculated using the energy functional 4.14, which has been implemented in the CASTOR3D code as described in chapter 4 [49, 58]. There

Tor. mode number n^*		1	2	3	4	5	6	15
γ (2D)	[1/s]	188380	359829	345114	173776	409451	525212	500055
γ (3D, fast)	[1/s]	197189	360345	345670	174903	411084	526736	500585
γ (3D, slow)	[1/s]	180158	353589	345503	174898	411084	526736	500585
$\Delta\gamma_{\text{3D,fast-slow}}$	[1/s]	17031	6756	167	5	0	0	0
$\Delta\gamma_{\text{2D}\to\text{3D}}$	[1/s]	8809	516	556	1127	1633	1524	530

Table 5.1: Growth rates for the axisymmetric (2D) and magnetically perturbed, non-axisymmetric (3D) equilibrium for different (dominating) toroidal mode numbers n^*. Growth rates of the 3D equilibrium are given for both orthogonal (fast and slow growing) or degenerate eigenvalues. The differences in growth rates of the fast and slow growing instabilities $\Delta\gamma_{\text{3D,fast-slow}}$ as well as of the 2D and fast growing 3D instabilities $\Delta\gamma_{\text{2D}\to\text{3D}}$ are shown.

are three dominating energy contributions, δW_{SHA}, δW_{CUR} and δW_{DP}:

$$\delta W_{\text{SHA}} = \int_V \boldsymbol{B}_{1,\perp}^2 \mathrm{dV} \tag{5.2}$$

$$\delta W_{\text{CUR}} = -\int_V \frac{\boldsymbol{j}_0 \cdot \boldsymbol{B}_0}{\boldsymbol{B}_0^2} (\boldsymbol{\xi}_\perp^* \times \boldsymbol{B}_0) \cdot \boldsymbol{B}_{1,\perp} \mathrm{dV} \tag{5.3}$$

$$\delta W_{\text{DP}} = -2 \int_V (\boldsymbol{\xi}_\perp \cdot \boldsymbol{\nabla} p_0)(\boldsymbol{\xi}_\perp^* \cdot \boldsymbol{\kappa}_0) \mathrm{dV} \tag{5.4}$$

while the other (always stabilizing) terms, δW_{CPA} and δW_{SND}, are typically very small. Analyzing the different energy contributions reveals that all modes are strongly current-density driven, while the relative pressure-gradient drive $\chi_{\text{DP/CUR}} = \delta W_{\text{DP}}/(\delta W_{\text{CUR}} + \delta W_{\text{DP}})$ increases with increasing toroidal mode number from 2.3% for $n = 1$ to 14.0% for $n = 15$.

5.1.1 Construction of the non-axisymmetric model equilibrium

Next, we perturb the plasma boundary with a resonant non-axisymmetric corrugation of periodicity $N_P = 2$. For this purpose, we start from the prescribed boundary of the axisymmetric equilibrium ("2D" equilibrium) and calculate the Fourier representation of the last closed flux surface in 2D straight-field-line coordinates. Then we add the desired non-axisymmetric toroidal harmonics ($N > 0$) to the Fourier spectrum encoding the last closed flux surface and assemble the last closed flux surface in real space. Finally, a non-axisymmetric equilibrium ("3D" equilibrium) is calculated from the generated non-axisymmetric plasma boundary while keeping safety factor, pressure profile and toroidal flux from the axisymmetric equilibrium using the fixed-boundary equilibrium solver GVEC [43].

Figure 5.2 shows the corrugation of the 3D equilibrium. The simple corrugation of the equilibrium has similar amplitude on the high and low field side and the MP field is shielded by the resonant surfaces. The maximum absolute values $\max_{s,M} |f(s,N,M)|$ of the Fourier coefficients $f(s,N,M)$ which encode the R and Z coordinates of the flux surfaces are shown in figure 5.3 for each toroidal harmonic $N > 0$. The Fourier spectrum contains non-axisymmetric contributions from all the toroidal harmonics N which are a multiple of N_P. The contribution of the toroidal equilibrium harmonics decreases exponentially.

As discussed in section 2.3.3, if we perturb the plasma boundary with a corrugation or MP field of toroidal periodicity N_P, the instabilities of the corresponding

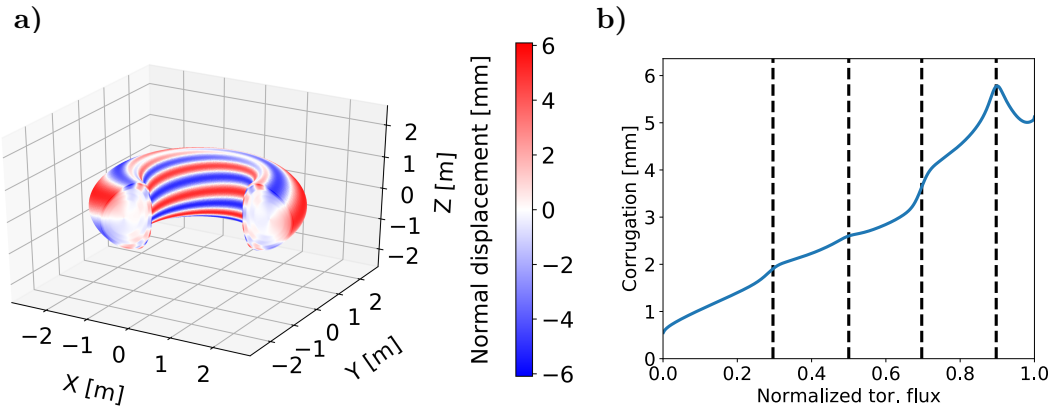

Figure 5.2: (a) Corrugation (normal displacement) of the 3D equilibrium for the numerical test case. (b) Maximum values of the corrugation on every flux surface as a function of the normalized toroidal flux s. The dashed lines mark the resonant flux surfaces with respect to the $N_P = 2$ MP field.

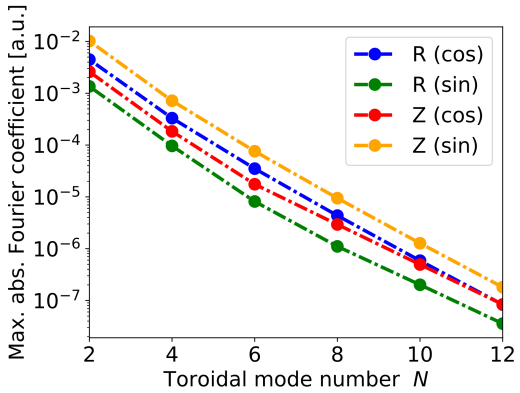

Figure 5.3: Maximum absolute values $\max_{s,M} |f(s, N, M)|$ of the Fourier coefficients $f(s, N, M)$ which encode the R and Z coordinates of the magnetically perturbed flux surfaces for each toroidal equilibrium harmonic N. Only multiples of N_P are contained in the equilibrium Fourier spectrum.

N_P-periodic equilibrium separate into $\lfloor (N_P + 1)/2 \rfloor$ toroidal mode families [47]. In the case of an $N_P = 2$ equilibrium, there are two different toroidal mode families $\mathcal{N}_1 = 1, 3, 5, 7, \ldots$ and $\mathcal{N}_2 = 0, 2, 4, 6, \ldots$. Without loss of generality, we restrict the analysis in this chapter to equilibria of periodicity $N_P = 2$. Furthermore, the Fourier decomposition of instabilities no longer contains only a single toroidal harmonic. There are multiple instabilities in each of the mode families, which can be labeled by their dominating toroidal harmonic n^*. In general, because of the 3D geometry, there are two non-degenerate or degenerate eigenvalues for each dominating toroidal harmonic n^*, which we will separate by their growth rate into "fast" and "slow" solutions. Since the non-axisymmetric tokamak configurations are in general not stellarator-symmetric, it is not possible to separate the eigenfunctions by their parity as it it usually done for stellarator plasmas (see [33, 47]).

5.1.2 Linear 3D stability analysis

In the following, the helical localization of the MHD instabilities is analyzed for the $n^* = 1, 2, 3, 4, 5, 6, 15$ instabilities. The Fourier spectrum of the radial velocity perturbation for the $n^* = 4$ fast growing mode as well as for one of the degenerate $n^* = 5$ instabilities is shown in figure 5.4a,b. While multiple toroidal harmonics ($n = 2, 4, 6$ or $n = 3, 5, 7$) are contained in the Fourier spectrum because of the coupling of toroidal harmonics, one can clearly see that there is a single strongly dominating toroidal harmonic, $n = 4$ or $n = 5$, for each of the instabilities which

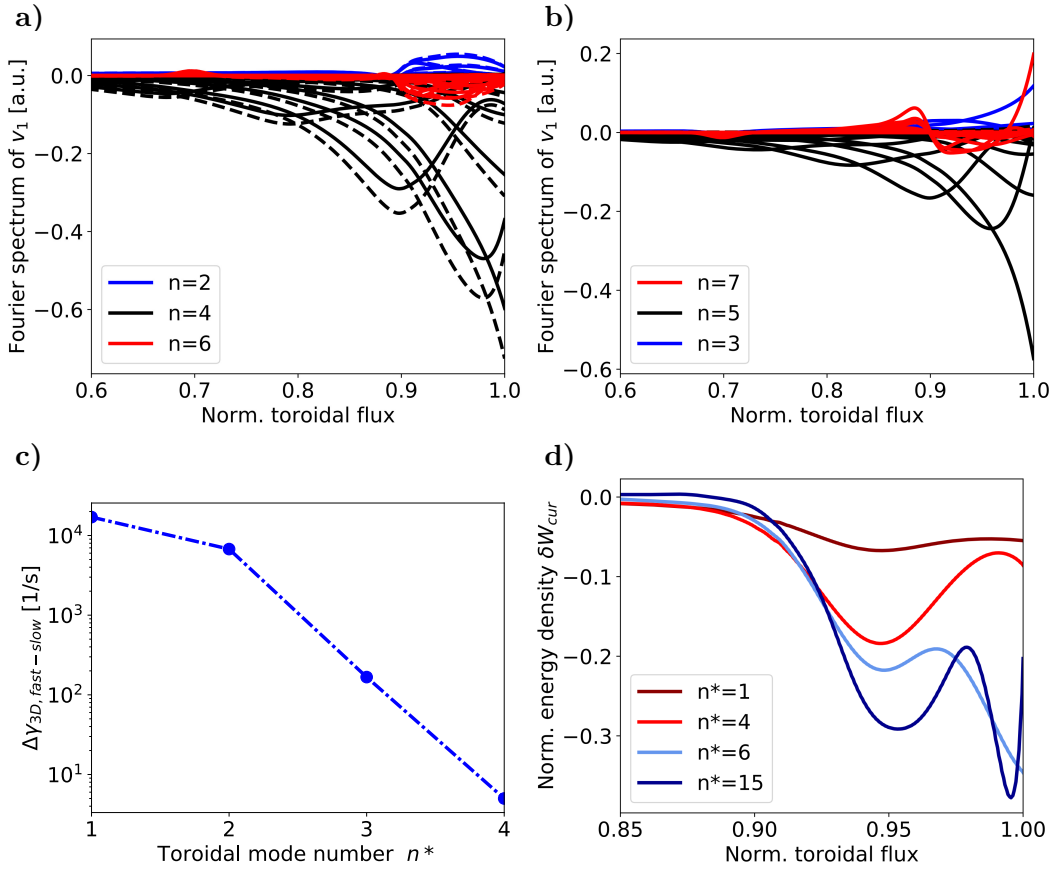

Figure 5.4: (a-b) Complex (solid) and complex-conjugate (dashed) Fourier coefficients of the radial velocity perturbation v_1 for the $n^* = 4$ fast growing mode (a) and the $n^* = 5$ mode, restricted for visibility to toroidal harmonics $n = 2, 4, 6$ and $n = 3, 5, 7$, respectively. (c) Non-degeneracy of the fast and slow eigenvalue solutions $\Delta\gamma_{\text{3D,fast-slow}}$ for the non-degenerate n^* modes. (d) Normalized energy density of the current-density drive δW_{cur} for different mode numbers n^* (fast growing).

determines n^*. Table 5.1 (page 39) contains the growth rates of the fast and slow growing $n^* = 1, 2, 3, 4, 5, 6, 15$ modes in comparison to their respective axisymmetric instability. One can clearly see that the instabilities become degenerate for $n^* > 4$, because the growth rate or eigenvalue is equal for the fast and slow growing instabilities, i.e. $\Delta\gamma_{\text{3D,fast-slow}} = 0$. The applied equilibrium corrugation has destabilized all instabilities of the plasma $\Delta\gamma_{\text{2D}\to\text{3D}} > 0$. Figure 5.4c reveals the exponential decrease of the energetic non-degeneracy with increasing mode number n^*, which is similar to the exponential decrease of the contributions from the equilibrium Fourier harmonics N (figure 5.3). The distinction into slow and fast growing is arbitrary for the degenerate instabilities, which is not important since they describe the same instability (equal growth rate and spatial mode structure). However, we keep this distinction for the degenerate instabilities in table 5.1 in order to indicate that there are still two solutions of the eigenvalue problem. Comparing the Fourier spectra of the instabilities which correspond to the non-degenerate and degenerate eigenvalues, one can see that the former have significant contributions from both complex and complex-conjugate Fourier coefficients (figure 5.4a), while the latter have only significant contributions from either the complex or complex-conjugate Fourier coefficients (figure 5.4b).

The energy density of the current-density drive δW_{CUR} for different mode num-

bers n^* is shown in figure 5.4d (see chapter 4) [58]. We will evaluate the helical localization of the eigenfunctions close to the most unstable flux surface. The most unstable flux surface is determined by the minimum of the potential energy density corresponding to the dominating drive, which is δW_{CUR} for current-density driven instabilities and δW_{DP} for pressure-gradient driven instabilities. If there is no clearly dominating drive, the helical localization has to be evaluated with respect to both energetic drives.

5.1.3 Toroidal mode locking

The eigenfunctions of an axisymmetric plasma $\boldsymbol{\chi}$ are proportional to a single toroidal harmonic $\boldsymbol{\chi} \sim e^{-in\Phi}$ because there is no coupling of the toroidal harmonics. Since in linear MHD the (complex) amplitude of the eigenfunctions is arbitrary, the multiplication of an eigenfunction by an arbitrary complex prefactor results in an equivalent eigenfunction corresponding to the same eigenvalue as the original eigenfunction. Thus, if $\boldsymbol{\chi}$ is an eigenfunction, $\boldsymbol{\chi}_\varphi = \boldsymbol{\chi} e^{i\varphi}$ are equivalent eigenfunctions for any solution phase $\varphi \in [0, 2\pi)$. In the case of a single toroidal harmonic, the solution phase is equivalent to a shift of the perturbation in the toroidal direction:

$$\boldsymbol{\chi}_\varphi(\Phi) \sim e^{-in\Phi} e^{i\varphi} = e^{-in(\Phi - \varphi/n)} \sim \boldsymbol{\chi}(\Phi - \varphi/n) \tag{5.5}$$

This implies that there is no preferred toroidal position of the eigenfunction for an axisymmetric plasma.

Since in a non-axisymmetric equilibrium different complex toroidal harmonics as well as complex-conjugates couple together, the eigenfunctions might be located at preferred toroidal/helical locations. Clearly, the transition between solution phase and a toroidal shift in equation 5.5 is no longer possible if there is more than one toroidal harmonic in the Fourier spectrum of the eigenfunction. For non-axisymmetric plasmas, eigenfunctions can lock to certain toroidal locations, creating "standing waves" with respect to φ by containing complex-conjugate Fourier harmonics in their spectrum, or they can localize toroidally without strictly locking via the superposition of different toroidal mode numbers, similar to the poloidal localization known from ballooning modes. We will distinguish *strictly locked* perturbations, which are perturbations for which the helical position is strictly constant for all values of φ, and *quasi-locked* perturbations, which are perturbations for which the helical position varies with φ but which are bound to an envelope of periodicity N_P. While the fine mode structure of the quasi-locked perturbations is not truly locked, their N_P envelope which determines the mode amplitude is locked at a fixed position. Thus, especially for instabilities with a high toroidal mode number, the structure of quasi-locked modes seems like a locked $n^* = N_P/2$ mode. This will be discussed in more detail in the next subsection.

In order to systematically analyze the helical/toroidal localization of instabilities we define quantities representing the spatial structure/location of the mode while being independent of the arbitrary amplitude and sign of the eigenfunction. Such quantities are for example given by the normalized square of the perturbed magnetic field eigenvectors $\mathrm{Re}(\boldsymbol{B}_1 e^{i\varphi}))^2$ or by the normalized physical energy densities of the ideal energy functional, normalized with respect to the square of the arbitrary amplitude of the eigenfunction. As the normalized squares of the eigenfunctions are strictly positive, they purely encode the spatial localization of the mode. These normalized squared quantities are strictly independent of the solution phase φ if the

mode is strictly locked or form an envelope for $\varphi \in [0, 2\pi)$ if the mode is quasi-locked. Note that the periodicity of the squared quantities is twice the periodicity of the corresponding mode, e.g. the energy densities and squared eigenvectors of an $n^* = 1$ mode have a periodicity of 2.

Since the instabilities in this section are current-density driven, we show the localization/ structure of the perturbations relative to the normalized non-axisymmetric part $\sigma_{1,N}$ of the parallel equilibrium current-density $\sigma = \boldsymbol{j}_0 \cdot \boldsymbol{B}_0 / \boldsymbol{B}_0^2$, which is defined as

$$\sigma_{1,N} = (\sigma - \sigma_{\mathrm{av}}) / \Delta\sigma_{\mathrm{av}} \tag{5.6}$$

where $\sigma_{\mathrm{av}}(u) = \langle \sigma \rangle_v$ is the average of $\sigma(u, v)$ over the toroidal coordinate v for every poloidal angle u and $\Delta\sigma_{\mathrm{av}} = \pm[\max\{\sigma_{\mathrm{av}}(u)\} - \min\{\sigma_{\mathrm{av}}(u)\}]$ is the variation of the axisymmetric parallel equilibrium current-density σ_{av} along the poloidal direction; the sign of $\Delta\sigma_{\mathrm{av}}$ is chosen such that $\sigma_{1,N} > 0$ stands for an augmented current-density.

The eigenfunctions with low dominating mode numbers $n^* = 1, 2, 3, 4$ are strictly locked. There are two orthogonal eigenfunctions (fast and slow growing) located at distinct toroidal/helical locations for each of these perturbations. Their corresponding eigenvalues are non-degenerate. The location of the perpendicular magnetic

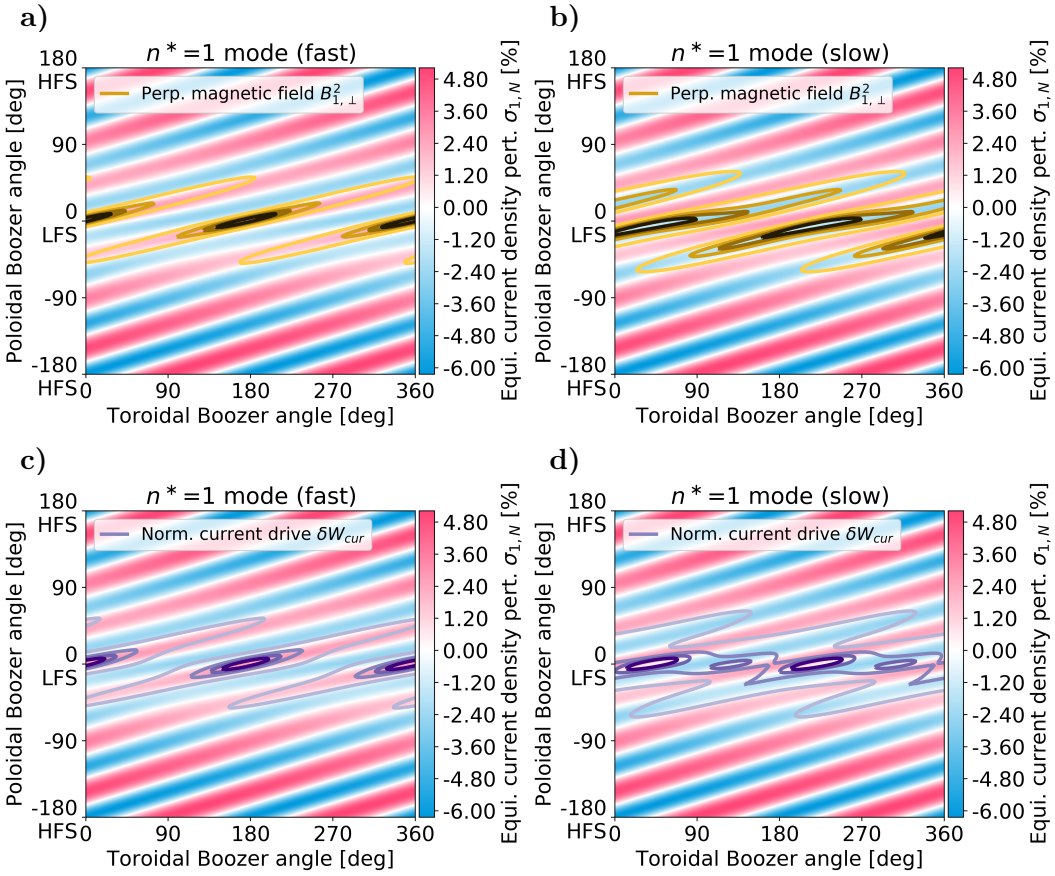

Figure 5.5: Background of (a-d): Normalized non-axisymmetric component of the parallel equilibrium current-density $\sigma_{1,N}$. Orange/brown lines in (a,b): Normalized perpendicular magnetic perturbation $\mathrm{Re}(\boldsymbol{B}_{1,\perp})^2$ of the $n^* = 1$ mode, darker color indicates a larger value of $\mathrm{Re}(\boldsymbol{B}_{1,\perp})^2$. Purple lines in (c,d): Normalized current-density drive $\delta W_{\mathrm{cur}} < 0$ of the $n^* = 1$ mode, darker color indicates more negative/destabilizing values of δW_{cur}. (a,c): Fast growing, (b,d) slow growing mode.

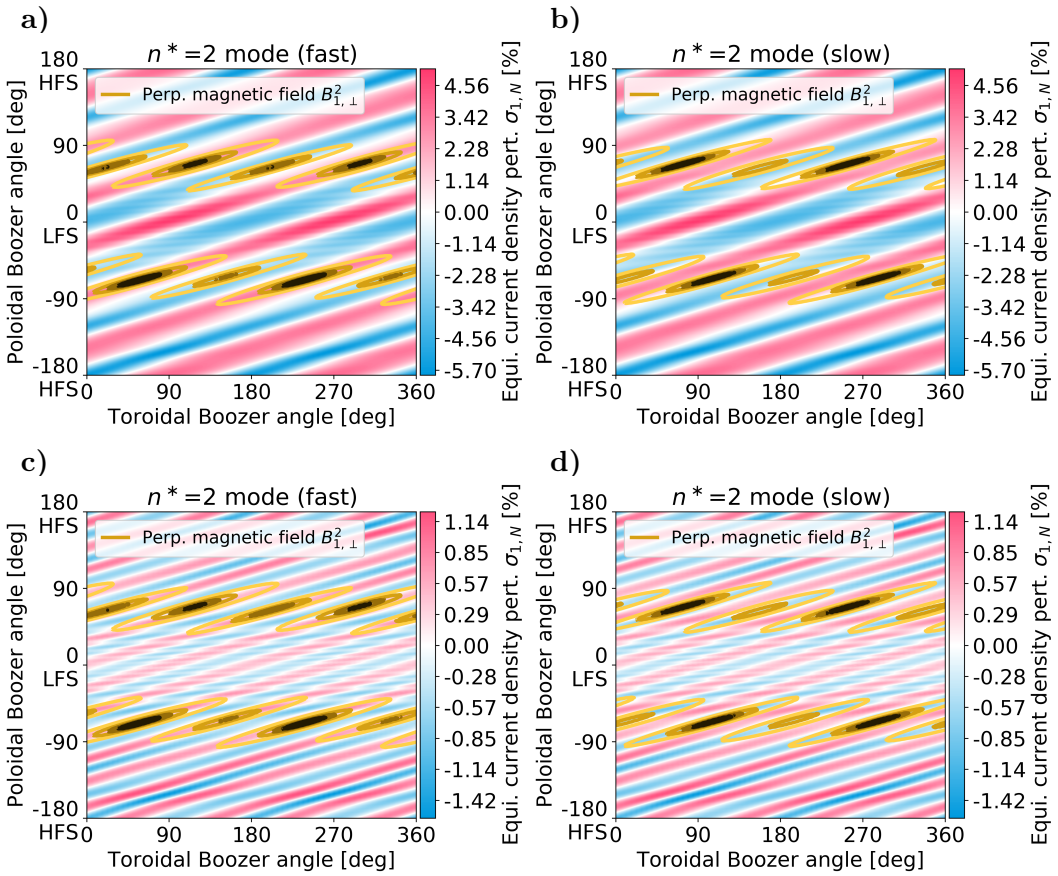

Figure 5.6: Background (a-d): Normalized non-axisymmetric component of the parallel equilibrium current-density $\sigma_{1,N}$, where in (c,d) the $N = 2$ component was subtracted. Orange/brown lines in (a-d): Normalized perpendicular magnetic perturbation $\mathrm{Re}(\boldsymbol{B}_{1,\perp})^2$ of the $n^* = 2$ mode, darker color indicates a larger value of $\mathrm{Re}(\boldsymbol{B}_{1,\perp})^2$. (a,c): Fast growing, (b,d) slow growing mode.

perturbation of the $n^* = 1$ fast and slow growing modes is shown in figure 5.5a,b. Although the two orthogonal $n^* = 1$ instabilities are located at different helical locations, they are positioned such that they maximize their current-density drive (figure 5.5c,d) which is optimized by locating where the non-axisymmetric part of the parallel equilibrium current-density $\sigma_{1,N}$ has its maximum. This alignment is natural since the instabilities are current-density driven. The faster growing $n^* = 1$ mode perfectly aligns with the regions where $\sigma_{1,N}$ is positive (figure 5.5c). The slower growing $n^* = 1$ mode, which is the second of the two orthogonal $n^* = 1$ solutions and shifted by $\Delta v \approx \pi/2$, is distorted such that it minimizes the localization in the region of negative $\sigma_{1,N}$ as much as possible (figure 5.5d). Clearly, the $n^* = 1$ mode which is located such that the parallel current-density drive is maximized is the faster growing dominating $n^* = 1$ instability. Since the mode energy is proportional to the square of the perturbation (see equations 5.3 and 5.4), the energy density of the $n^* = 1$ instability is correlated with the non-axisymmetric $N = 2$ equilibrium harmonic.

As one can see in figure 5.6a, the fast growing $n^* = 2$ mode is localized in the regions of augmented as well as in regions of weakened parallel equilibrium current-density. If there are maxima of the $n = 2$ harmonic of the instability at the regions of augmented parallel equilibrium current-density (magenta region in figure 5.6a), there are also maxima at the regions of weakened parallel equilibrium current-density

(cyan region in figure 5.6a), because the energy of the $n = 2$ harmonic has 4 maxima which can not be aligned with the two maxima of the dominating equilibrium harmonic $N = 2$. This means the $n^* = 2$ instability is not correlated with the $N = 2$ equilibrium harmonic and its location is not determined by the $N = 2$ equilibrium harmonic. However, the non-degeneracy and localization of the $n^* = 2$ perturbation is reasoned by the correlation with the $N = 4$ equilibrium harmonic. This can be seen in figure 5.6c,d, where we subtracted the $N = 2$ harmonic from $\sigma_{1,N}$ in order to reveal the $N = 4$ component of the parallel equilibrium current-density. The fast growing $n^* = 2$ mode is at a favorable position (region of augmented current-density) while the slow growing $n^* = 2$ mode is at a less optimal position (region of weakened current-density) with respect to the $N = 4$ harmonic (see figure 5.6c,d). Moreover, the localization in the regions of minimum parallel current-density is reduced by coupling to the $n = 0, 4$ harmonics, maximizing the growth rate of the $n^* = 2$ modes (figure 5.6a,b).

5.1.4 Quasi-locked modes

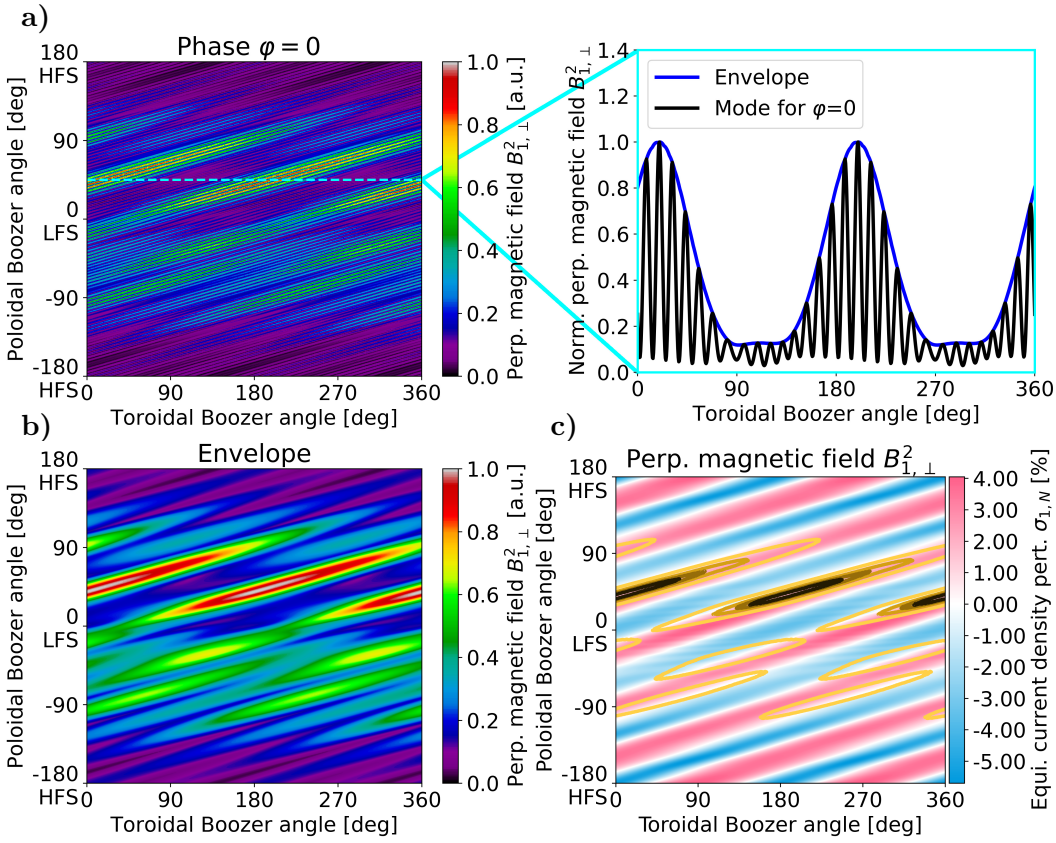

Figure 5.7: Normalized perpendicular magnetic perturbation $\mathrm{Re}(\boldsymbol{B}_{1,\perp}e^{i\varphi})^2$ of the $n^* = 15$ mode at $\varphi = 0$ (a) and its envelope $E = \max_\varphi\{\mathrm{Re}(\boldsymbol{B}_{1,\perp}e^{i\varphi})^2\}$ (b). Background of (c): Normalized non-axisymmetric component of the parallel equilibrium current-density $\sigma_{1,N}$. Orange/brown lines in (c): Normalized perpendicular magnetic perturbation $\mathrm{Re}(\boldsymbol{B}_{1,\perp})^2$ of the $n^* = 15$ mode, darker color indicates a larger value of $\mathrm{Re}(\boldsymbol{B}_1)^2$.

The location of the perpendicular magnetic perturbation of the $n^* = 15$ mode as well as the corresponding envelope are shown in figure 5.7a,b. One can see that the precise location of the eigenfunction is not fixed but bound to an envelope

$E = \max_\varphi\{\mathrm{Re}(\boldsymbol{B}_{1,\perp} e^{i\varphi})^2\}$ of periodicity N_P. In order to determine the envelope, it is necessary to evaluate the eigenfunction at a range of solution phase angles φ. As expected, close to the most unstable flux surface, the envelope of the $n^* = 15$ eigenfunction is aligned with the maximum equilibrium current-density perturbation (see figure 5.7c). Note that the eigenfunction is eventually not aligned with the maximum equilibrium current-density perturbation at flux surfaces which are far from the most unstable flux surface.

From the considerations in this section it follows that, in general, for every harmonic of the equilibrium spectrum N the location of the perturbation with mode number

$$n^* = N/2 \tag{5.7}$$

can be optimized with respect to this equilibrium harmonic N, resulting in non-degenerate perturbations. Since the contributions of the equilibrium harmonics decrease exponentially, the non-degeneracy, which encodes the strict locking of the instability, also decreases exponentially. Note that only instabilities which are a multiple of $N_P/2$ can be non-degenerate / strictly locked, belonging either to the $N_P/2$ or N_P mode family (see [47]). The energy of the degenerate instabilities is independent from the precise toroidal location of the eigenfunction but instead is determined by its envelope (with respect to the solution phase φ), which is aligned with the equilibrium perturbation of periodicity N_P. This can be seen for the $n^* > 4$ modes, which are quasi-locked. This interpretation is also in agreement with the results from linear MHD calculations for stellarators [33].

5.2 Strictly locked and quasi-locked instabilities in rotating plasmas

While both strictly locked and quasi-locked instabilities are helically localized, quasi-locked modes can still appear at slightly varying locations under the envelope. In order to further improve the understanding of the difference between strictly locked and quasi-locked modes, we investigate the behaviour of the instabilities for finite equilibrium rotation of the plasma Ω_0. Note that the equilibrium plasma rotation is only included for the stability analysis (i.e. in the linearized equation system) but not for the equilibrium calculation, which is justified for low Mach numbers $Ma \lessapprox 0.2$ [39]. The values of the plasma rotation applied in this section are lower than $\Omega_0 = 15000$ rad/s, which corresponds to a Mach number of $Ma = 0.036$ and is consistent with the limit in [39], with exception of the high rotation scenario $\Omega_0 = 100000$ rad/s, which corresponds to a Mach number of $Ma = 0.24$.

While the non-degenerate instabilities remain strictly locked in their position even for finite plasma rotation, the degenerate eigenfunctions immediately start rotating under their envelope. Figure 5.8a shows the growth rates and oscillation frequencies for the fast and slow $n^* = 3$ modes. If one exceeds a critical rotation $\Omega_0 > \Omega_{\mathrm{crit}}(n^*)$, also the formerly non-degenerate instabilities become degenerate and start to rotate. This behaviour was also previously investigated for stellarators [33]. The critical rotation for the $n^* = 3$ mode is $\Omega_{\mathrm{crit}}(3) = 28.8$ rad/s, which is a very small edge rotation threshold. Note that although the sign of the oscillation frequency is opposite for the two different eigenfunctions, they rotate in the same direction in real space. The critical rotation for the much stronger non-degenerate $n^* = 1$ mode is $\Omega_{\mathrm{crit}}(1) = 9765$ rad/s, which is in the order of typical edge rotation values of present machines. From the above consideration, it follows that quasi-locked instabilities have a critical rotation threshold of zero.

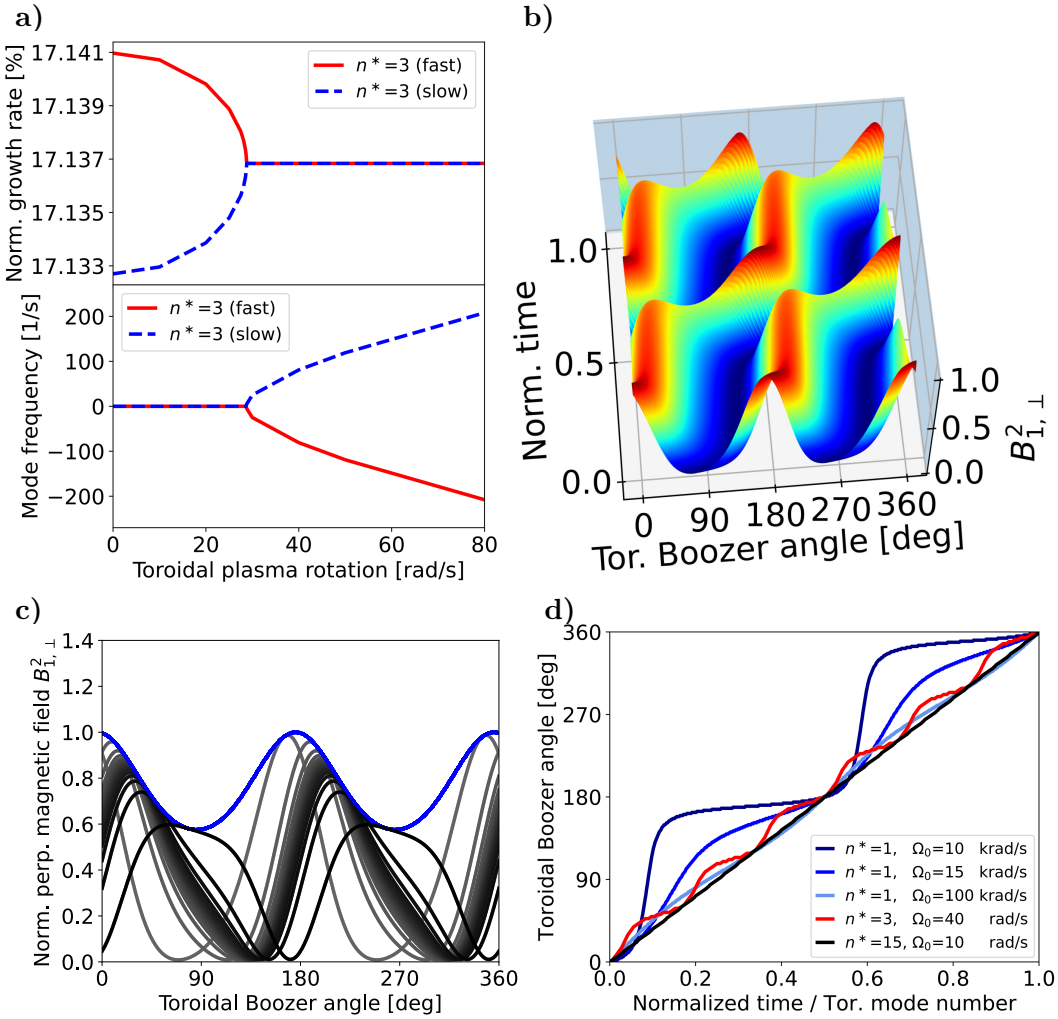

Figure 5.8: (a) Normalized growth rate and oscillation frequency for the fast (red, solid) and slow (blue, dashed) $n^* = 3$ modes in dependency of the plasma rotation Ω_0. (b-c) Movement of the normalized perpendicular magnetic perturbation $\mathrm{Re}(\boldsymbol{B}_{1,\perp} e^{i\omega t})^2$ of the $n^* = 1$ mode at the outboard midplane at $s = 0.949$ over a full oscillation period $\omega t \in [0, 2\pi]$. The time is normalized with respect to $\omega/(2\pi)$. (b) Time-evolution of the perturbation as a surface plot, which shows the movement of the instability. For improved visibility, the value of the Z axis is color-coded. (c) Time-evolution of the perturbation (gray to black) as a projection of equally distanced time steps, which shows the deformation of the mode during the oscillation cycle. The time is increasing from the light gray to the black curves. The amplitude of the normalized perpendicular magnetic perturbation is bound by an envelope (blue). (d) Relative toroidal position of the minimum of the normalized perpendicular magnetic perturbation (as shown in c) for different mode numbers n^* over a full rotation cycle of the mode around the torus $\omega t \in [0, 2\pi n^*]$. The plasma rotation was taken at values above the critical rotation threshold for each toroidal mode number. $n^* = 1$: $\Omega_0 = 10000$ rad/s (dark blue), $\Omega_0 = 15000$ rad/s (blue), $\Omega_0 = 100000$ rad/s (bright blue); $n^* = 3$: $\Omega_0 = 40$ rad/s (red); $n^* = 15$: $\Omega_0 = 10$ rad/s (black).

Clearly, the strictly locked modes are forced to rotate by the background velocity of the plasma. Since these instabilities naturally want to stay at a fixed location, they rotate irregularly/non-uniform, like being pushed through a bottleneck, which can be seen in figures 5.8b-d. From the time-evolution of the irregular rotation, one can see that the instability seems to jump form one preferred location/position of rest to the next (figure 5.8b). The instability is bound to an envelope. The mode slows down and nearly stops (region of high line density in figure 5.8c) before traversing the minimum of its envelope. While traversing the minimum, the mode is strongly deformed. The irregularity of the rotation decreases with both increasing plasma rotation and decreasing non-degeneracy of the instabilities in a flow-free plasma (figure 5.8d).

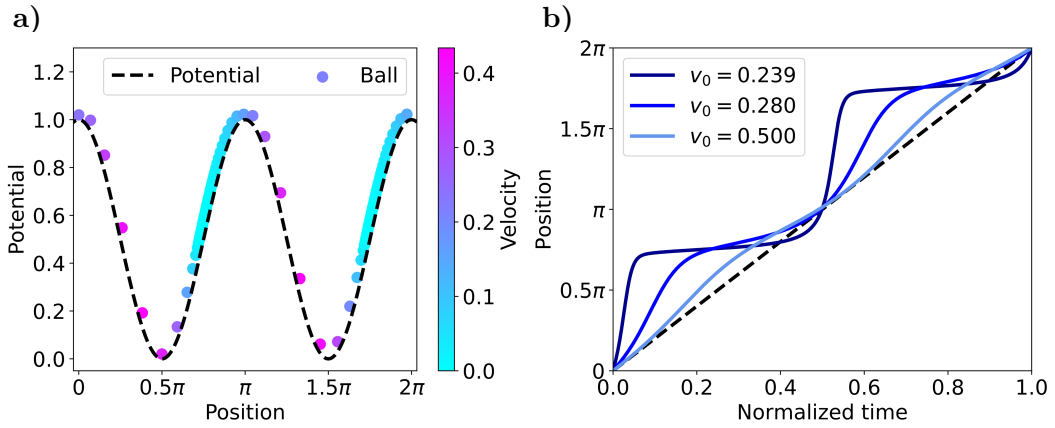

Figure 5.9: (a) Forced motion of a ball in a sinusoidal potential (dashed black line) at equally distanced time steps (circles) for $v_0 = 0.238$. The velocity of the ball is color-coded. (b) Position of the ball for different background velocities v_0. The time is normalized to two full hill crossings. The motion was calculated for $m = 1$, $\alpha = -0.85$ and $k = -0.2$.

This system shows similar behaviour to a ball in a sinusoidal potential which is exposed to an external drag force. A sketch of such a system is shown in figure 5.9a. Here we assume a ball which lies on a chain of hills made of a mesh and is forced to roll over the structure by a strong horizontal stream of air. The same behaviour would also be achieved for an electrically charged particle in an electrostatic sine potential which is forced to move through the potential by a background flow of neutrals. The equation of motion for such a system is given by:

$$m\ddot{x} = \underbrace{\alpha(\dot{x} - v_0)}_{\text{Drag}} + \underbrace{kh'(x)}_{\text{Restoring force}} = \alpha(\dot{x} - v_0) + k\sin(2x) \tag{5.8}$$

where m is the mass, v_0 the background velocity, α the drag force strength, k the potential force strength and $h(x) = \sin(x)^2$ the profile of the potential. The potential force strength is related to the degeneracy $k \sim \Delta\gamma_{\text{3D,fast-slow}}$, the background flow is related to the equilibrium velocity of the plasma $v_0 \sim \Omega_0$ and the potential is related to the envelope of the instability $h(x) \sim E$. Note that a similar equation of motion describes mode locking of tearing modes caused by external error fields [35, 64, 65]. Numerical integration of equation 5.8, shown in figure 5.9b, provides the motion of the ball within the defined system and is in good agreement with the rotation behaviour of the quasi-locked and locked modes (see figure 5.8d). The ball only passes the hilltop above a critical threshold for the background flow, which is $v_{\text{crit}} \approx 0.2354$ for the chosen set of parameters $m = 1$, $\alpha = -0.85$ and $k = -0.2$. Below this

threshold the drag has not enough strength to push the ball over the hilltop and a force equilibrium between the drag and potential force is reached. This mechanical system provides a physical understanding of the irregular rotation of strictly locked and quasi-locked MHD modes. The mode is dragged by the equilibrium plasma flow while a restoring force from a potential (represented by the envelope) tries to pull the instability back to its preferred localization. While there is an envelope also for the quasi-locked modes, their restoring force is small, since they are (numerically) degenerate ($k \approx 0$).

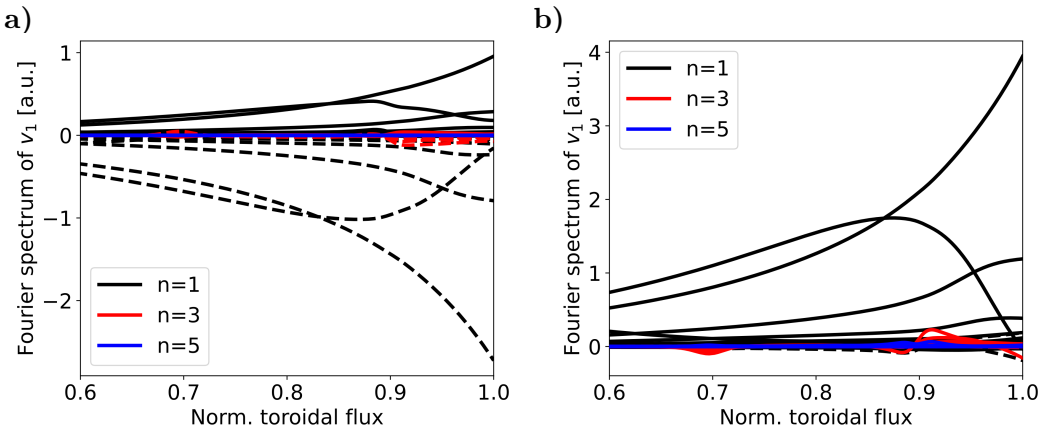

Figure 5.10: Complex (solid) and complex-conjugate (dashed) Fourier coefficients of the radial velocity perturbation v_1 for the $n^* = 1$ mode restricted for visibility to toroidal harmonics $n = 1, 3, 5$ at a plasma rotation of $\Omega_0 = 15000$ rad/s (a) and $\Omega_0 = 100000$ rad/s (b).

Finally, figure 5.10 shows the Fourier spectrum of the $n^* = 1$ instability for $\Omega_0 = 15000$ rad/s and $\Omega_0 = 100000$ rad/s. If the plasma rotation is large enough such that the forced rotation of the strictly locked $n^* = 1$ instability becomes nearly uniform, there are only significant contributions of either the complex or complex-conjugate Fourier coefficients to the spectrum of the eigenfunction. Thus, for $\Omega_0 \gg \Omega_{\text{crit}}$, the Fourier spectrum of the forced rotating modes becomes similar to the spectrum of the quasi-locked modes (see figure 5.4b). A similar suppression of complex or complex-conjugate Fourier coefficients was also recently found for instabilities in stellarator plasmas which were strongly affected by diamagnetic drift [34].

5.3 Application to an AUG experimental case

In the following, we compare the numerically predicted mode localization to experimental measurements. The experiment which we will use for comparison was performed at the ASDEX Upgrade tokamak and an experimental analysis was done in [24]. Here, the initially axisymmetric magnetic field of the tokamak was perturbed by magnetic perturbation coils, which create a non-axisymmetric vacuum field acting on the plasma equilibrium. The plasma reacts to this vacuum perturbation with a saturated kink-response forming a weakly non-axisymmetric equilibrium. In this experiment, an $N_P = 2$ vacuum perturbation field was rotated around the plasma toroidally at a frequency of 3 Hz while the MHD activity was measured by the Electron Cyclotron Emission (ECE) diagnostic at a toroidally fixed location on the outboard midplane as shown in figure 5.11. This method allows ECE data to be obtained at different toroidal phase angles Φ_{MP} of the vacuum field, which is

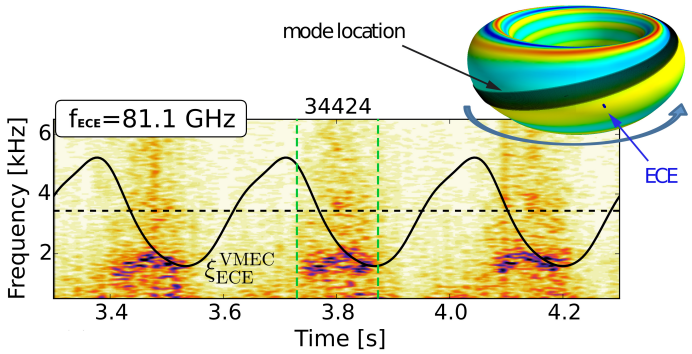

Figure 5.11: Spectrogram of the ECE intensity for experiment AUG #34424 for a single ECE channel f_{ECE} (adapted from [24]). The MP field and consequently the corrugation are rotated in counter-clockwise direction. The ECE signal time-trace corresponds to a scan of the toroidal coordinate in clockwise direction. Black curve: Corrugation of the plasma boundary at the ECE line-of-sight. Dashed black line: Level of zero corrugation. The dashed green lines enclose a time-frame of high MHD activity (dark region in the spectrogram).

equivalent to a scan in the toroidal direction.

Figure 5.11 shows the spectrogram of the ECE intensity for a ECE frequency f_{ECE} emitted from the plasma edge measured during the experiment as well as the equilibrium corrugation at the ECE position. One can see that there is MHD activity, caused by inter-ELM modes [24], in the ECE spectrogram (darker regions) only on every other zero of the corrugation. However, since the ECE measures at the same flux surface for every zero of the corrugation this means that the MHD activity or MHD instabilities must be toroidally/helically localized, i.e. they occur at preferred toroidal locations. This is further confirmed by magnetic measurements [24]. Moreover, ELM activity is also found to be at the same location as the inter-ELM modes [24].

For the numerical MHD stability analysis, the non-axisymmetric MHD equilibrium was calculated with the NEMEC [40, 42] and GVEC [43] codes for the applied MP coil currents and for the experimental equilibrium profiles and axisymmetric coil currents obtained by equilibrium reconstruction using the CLISTE code [41]. We use the free-bounadry equilibrium code NEMEC to obtain the perturbed plasma boundary from the coil currents, which is in good agreement with experimental lithium beam measurements (see [24]), and refine the NEMEC equilibrium using the GVEC code.

Figure 5.12a shows the resulting corrugation of the magnetically perturbed equilibrium. The Fourier spectrum of the equilibrium contains significant non-axisymmetric contributions of the toroidal harmonics $n = 2, 4$. Figure 5.12b shows a Poincaré plot of the equilibrium, revealing that there is ergodization of the magnetic field near the edge. For the stability analysis, we will crop the ergodized region of the equilibrium at the dashed line in figure 5.12b ($s = 0.98$) since this region is not well-described by closed flux surfaces or straight-field-line coordinates. The cropped region contains 0.92% of the toroidal plasma current and 0.02% of the thermodynamic energy $W_{\mathrm{pV}} = \int p\mathrm{d}V$. The thickness of the cropped region at the outboard midplane is 1.8 mm averaged over the toroidal direction.

While the axisymmetric equilibrium, i.e. without application of the MP coils, is stable with respect to ideal MHD, the non-axisymmetric equilibrium is unstable to

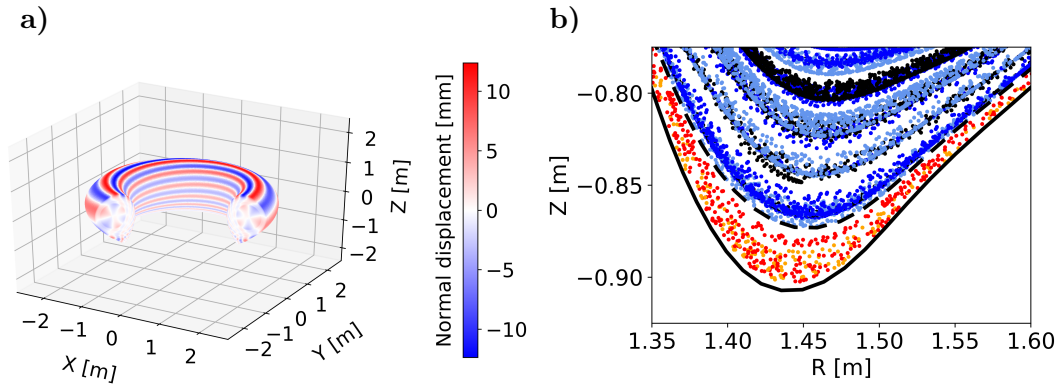

Figure 5.12: (a) Corrugation of the magnetically perturbed equilibrium for AUG #34424. (b) Poincaré plot of the equilibrium. Black and blue dots: closed field lines (10000 turns), Red and orange: open field lines (less than $\sim$ 1022 turns). The solid black line is the plasma boundary determined by the equilibrium code. The dashed black line indicates, where we cropped the equilibrium.

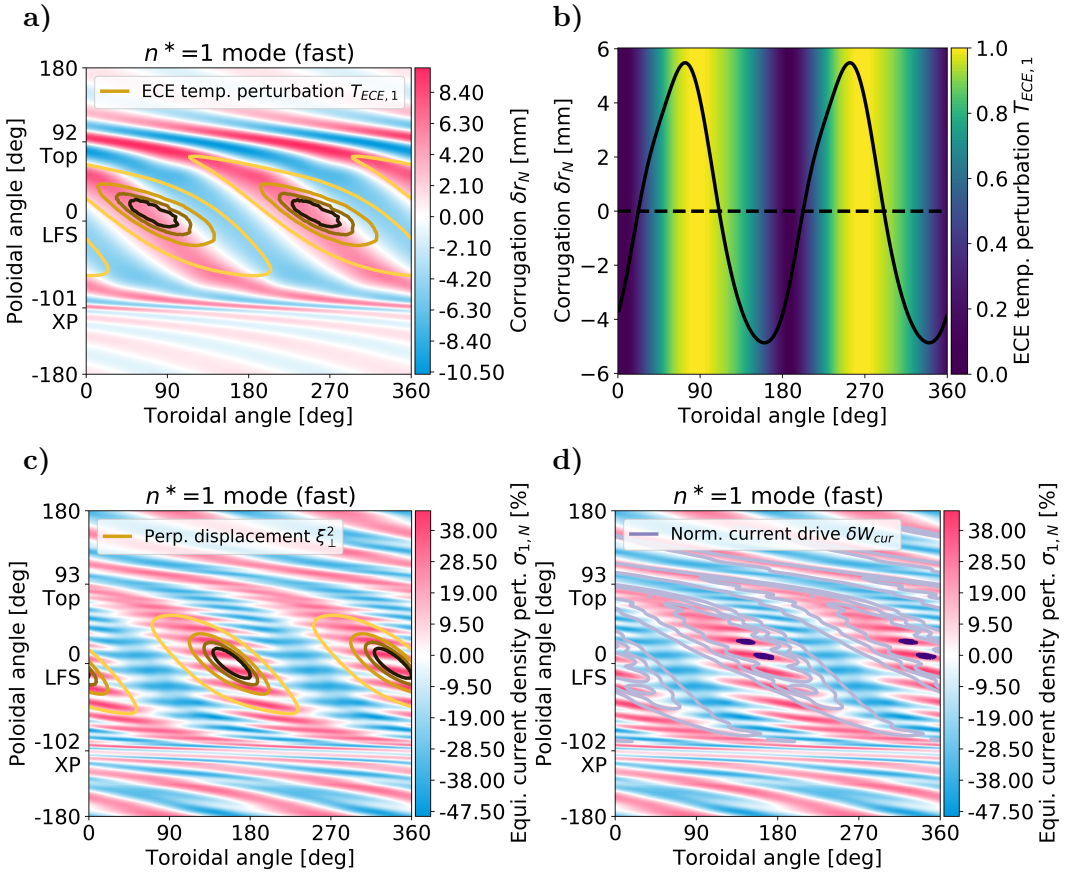

Figure 5.13: (a-b) Absolute value of the ECE temperature perturbation at $s = 0.9018$ (pressure gradient peak at the mid of the pedestal) relative to the equilibrium corrugation on the unraveled surface (a) and at the ECE position (b). (c) Normalized perpendicular displacement and (d) current-density drive relative to $\sigma_{1,N}$ at the most unstable flux surface $s = 0.9772$.

a strictly locked, ideal, purely current-density driven ($\delta W_{\mathrm{DP}} > 0$), $n^* = 1$ instability located at the plasma edge. Since the ECE measurement corresponds to a point of constant magnetic field strength along the ECE line-of-sight whereas perturbed

quantities in ideal MHD are defined at a constant point in space, we must couple the perturbed quantities to the perturbation of the magnetic field for comparability to the ECE data. To first order, the linear (electron) temperature perturbation at the ECE point of view becomes

$$T_{\mathrm{ECE},1} = T_1(B = \text{const.}) = T_1 - 2\frac{\boldsymbol{e}_R \cdot \boldsymbol{\nabla} T_0}{\boldsymbol{e}_R \cdot \boldsymbol{\nabla} B_0^2} \boldsymbol{B}_0 \cdot \boldsymbol{B}_1 \tag{5.9}$$

where $\boldsymbol{e}_R$ is the vector pointing in the direction of the ECE line-of-sight and all quantities on the right side of the equation are evaluated at $\boldsymbol{x}_0$ corresponding to the equilibrium ECE point of view. In equation 5.9, the thermodynamic temperature T may be replaced by any quantity. Replacing T by the magnetic field strength B, we get $B_{\mathrm{ECE},1} \equiv 0$ by construction. Note that the ECE diagnostic measures the ECE intensity or radiation temperature T_{rad}, which is not the same as the thermodynamic (electron) temperature at the ECE point of view T_{ECE} (see [66]). However, in order to compare the helical mode localization between the experiment and linear MHD, we assume that the localization of the MHD activity measured by the ECE diagnostic is strongly related to the linear MHD temperature perturbation at the ECE point of view T_{ECE}.

Figure 5.13a,b shows the linear ECE temperature perturbation $T_{\mathrm{ECE},1}$ of the calculated $n^* = 1$ instability relative to the equilibrium corrugation at $s = 0.9018$. The poloidal and toroidal angles are the geometric angles determined with respect to $\boldsymbol{R}_0 = (R_{\mathrm{geo}}, Z_{\mathrm{ECE}})$, where $R_{\mathrm{geo}} = 1.66$ m is the geometric radius of the device and $Z_{\mathrm{ECE}} = 3.5$ cm is the ECE height. The toroidal angle increases in the clock-wise direction in order to be comparable to the time-trace of the ECE spectrogram shown in figure 5.11. One can see that, similar to the measured ECE intensity, $T_{ECE,1}$ is large close to the zero-crossing of the corrugation which is right from the maximum corrugation and $T_{ECE,1}$ is small close to the zero-crossing of the corrugation which is left from the maximum corrugation. Figure 5.13c,d shows the perpendicular displacement and normalized current-density drive of the perturbation relative to $\sigma_{1,N}$. The perpendicular displacement is located at the regions of augmented equilibrium current-density, maximizing the potential energy of the instability. Note that the small misalignment between δW_{cur} and $\sigma_{1,N}$ (figure 5.13d) could be the consequence of the increasing influence of the stabilizing energy contributions close to the stability boundary.

5.4 Modified equilibrium

Finally, we varied the experimental equilibrium profiles in order to test if the localization of the instability with respect to the equilibrium corrugation is robust. We increased the current-density and pressure gradient in the edge by a factor of 2, while keeping the total toroidal current, plasma energy and shaping constant. However, because of the increased current-density and pressure gradient, we had to reduce the MP field strength by a factor of 3 in order to get a converged non-axisymmetric MHD equilibrium. The corrugation of the resulting non-axisymmetric equilibrium as well as a comparison of the pressure and safety factor profiles of the modified and unmodified case are shown in figure 5.14.

The modified equilibrium is unstable to edge localized instabilities of any toroidal mode number even without application of the MP coils, where we have calculated growth rates for $n = 1$ to $n = 23$. The growth rates and the relative pressure-gradient drive increase with increasing toroidal mode number. All investigated

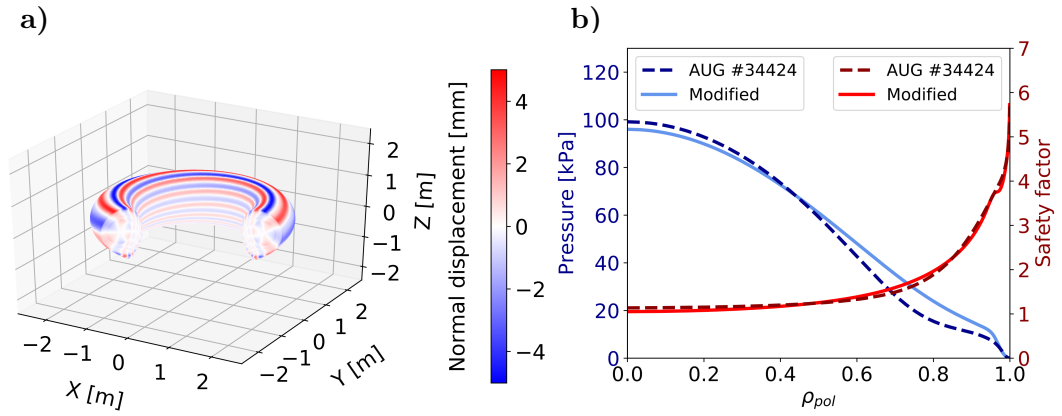

Figure 5.14: (a) Corrugation of the magnetically perturbed equilibrium for the modified AUG #34424 case. (b) Pressure (blue) and safety factor (red) profiles for experiment AUG #34424 (dashed) and the modified AUG #34424 case (solid) as function of ρ_{pol}.

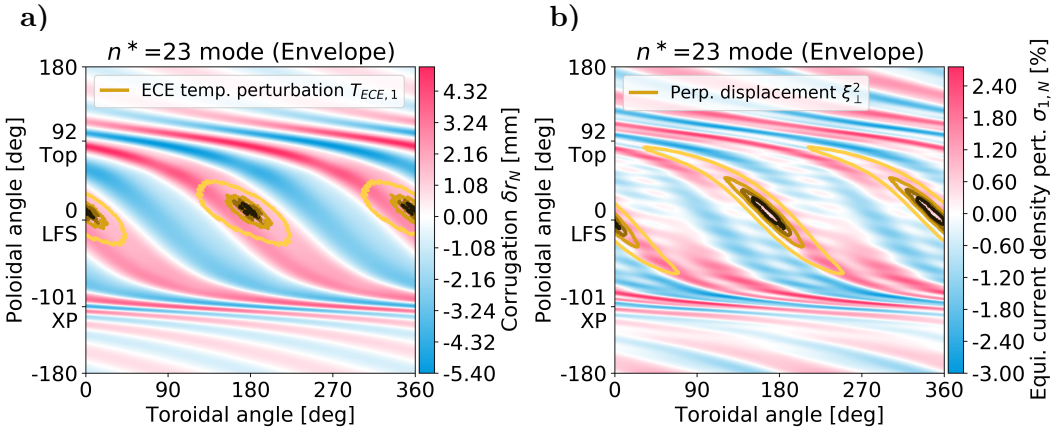

Figure 5.15: (a) Absolute value of the ECE temperature perturbation at $s = 0.885$ (pressure gradient peak at the mid of the pedestal) relative to the equilibrium corrugation for the $n^* = 23$ mode. (b) Normalized perpendicular displacement relative to $\sigma_{1,N}$ at the most unstable flux surface $s = 0.9060$ w.r.t. δW_{CUR} for the $n^* = 23$ mode.

toroidal mode numbers have significant contributions from the current-density drive ($\delta W_{\mathrm{CUR}}/(\delta W_{\mathrm{CUR}} + \delta W_{\mathrm{DP}}) = 92\%$ for $n^* = 1$ to 50% for $n^* = 23$). The $n^* = 1 - 4$ modes are strictly locked while the $n^* > 5$ instabilities are quasi-locked.

The ECE temperature for the $n^* = 23$ (most unstable) instability is shown in figure 5.15a. One can see that the linear ECE temperature of the $n^* = 23$ mode is not located at the same location relative to the equilibrium corrugation as the experimentally measured instabilities, which is reasoned by the modified pressure and current-density profiles. However, since the instability is still significantly current-density driven, it is still aligned with the regions of augmented equilibrium current-density (figure 5.15b). This is in agreement to the alignment of the current-density driven instabilities analyzed in the previous sections. In addition, the $n^* = 23$ instability is 50% pressure-gradient driven. For this reason, the instability is also aligned with the regions of increased "bad curvature" $\kappa_p = \boldsymbol{\kappa} \cdot \boldsymbol{\nabla} p_0$ at the most unstable flux surface with respect to δW_{DP}, which is shown in figure 5.16. The non-axisymmetric component of the "bad curvature", which is induced by the MP field, is defined

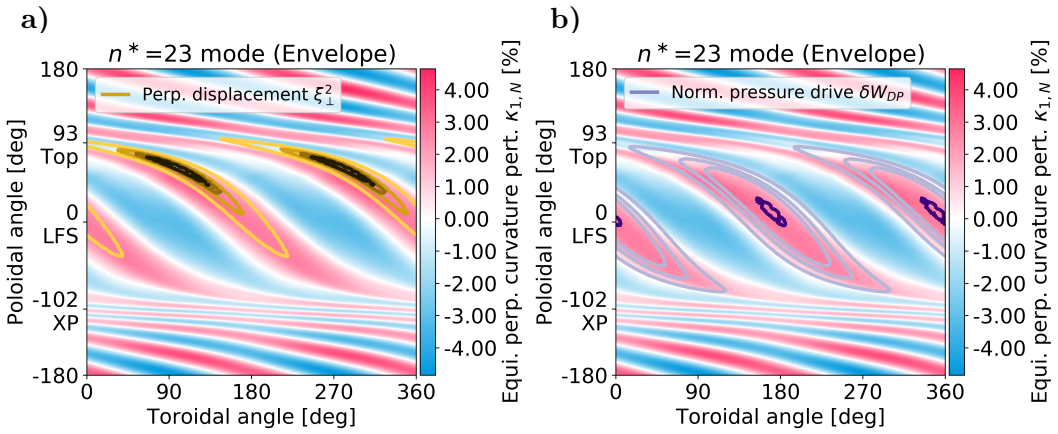

Figure 5.16: (a) Normalized perpendicular displacement and (b) pressure-gradient drive relative to the non-axisymmetric component of the bad curvature $\kappa_{1,N}$ at the most unstable flux surface $s = 0.9214$ w.r.t. δW_{DP} for the $n^* = 23$ mode.

similarly to the non-axisymmetric component of the parallel current-density 5.6:

$$\kappa_{1,N} = (\kappa_p - \kappa_{p,\mathrm{av}})/\Delta\kappa_{p,\mathrm{av}} \tag{5.10}$$

where $\kappa_{p,\mathrm{av}}(u) = \langle\kappa_p\rangle_v$ is the average of $\kappa(u,v)$ over the toroidal coordinate v for every poloidal angle u and $\Delta\kappa_{p,\mathrm{av}} = \pm[\max\{\kappa_{p,\mathrm{av}}(u)\} - \min\{\kappa_{p,\mathrm{av}}(u)\}]$ is the variation of the axisymmetric parallel equilibrium current-density $\kappa_{p,\mathrm{av}}$ along the poloidal direction; the sign of $\Delta\kappa_{p,\mathrm{av}}$ is chosen such that $\kappa_{1,N} > 0$ stands for increased "bad curvature". The flux surfaces shown in figures 5.15b and 5.16 are different since there are unique most unstable flux surfaces with respect to the current-density and pressure-gradient drive. The global localization of the instability is a balance between the favourable localization with respect to the pressure-gradient and current-density drives, maximizing their respective contributions.

In conclusion, the localization of the instability relative to the equilibrium corrugation varies with moderate variations of the equilibrium. For this reason, the equilibrium corrugation is generally not a robust metric to describe helical mode localization. Instead, the localization of the mode is determined by the energetic drives close to the most unstable flux surface. Since the application of MP fields results in a non-axisymmetric structure of the stability-relevant equilibrium quantities such as parallel current-density or bad curvature, instabilities might optimize their location with respect to the non-axisymmetric equilibrium in order to maximize their growth. Depending on their energetic decomposition, instabilities might preferably align with regions of augmented equilibrium current-density (current-density driven modes) or bad field-line curvature (pressure-gradient driven modes) or the position will be a complex compromise between these alignments such that the global energy is minimized. While this is a very general statement a detailed global MHD stability analysis is required in order to predict the precise localization of general finite-n instabilities for a specific MHD equilibrium.

6 Reduction of the MHD stability threshold by non-axisymmetric perturbation fields

In the following, we demonstrate for the first time that symmetry-breaking in tokamak plasmas reduces the window of stable edge operational space, leading to a lower achievable edge pressure gradient. Previous work described the impact of MP fields on the stability threshold for local ballooning modes, i.e. in the limit of infinite toroidal mode number n [29, 30]. There are also reports on the increase of growth rates for finite-n peeling-ballooning modes with both perturbative models (limit of small MP fields) [28, 31] and fully non-axisymmetric linear MHD [63]. However, until now, there is no analysis of the impact of symmetry-breaking on the achievable edge pressure in tokamak plasmas.

6.1 Stability analysis of model equilibria

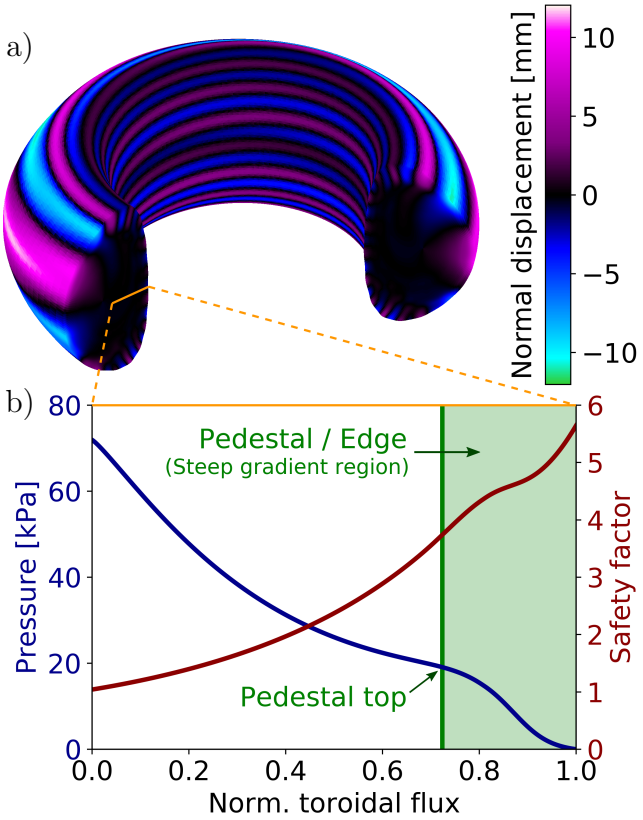

Figure 6.1: Flux-surface corrugation (normal displacement) of a magnetically perturbed tokamak plasma (a) as well as pressure and safety factor profiles (b) for a model equilibrium with $n_{\mathrm{e,ped}} = 4 \cdot 10^{19}$ m^{-3} and $p_{\mathrm{ped}} = 19.1$ kPa.

In this section, we analyze the impact of symmetry-breaking induced by MP fields on the full MHD stability boundary which contains low-n kink-peeling mode to high-n peeling-ballooning mode limited regimes of the operational space. For this purpose, we create a set of model equilibria using IPED2 [51]. For this study, global parameters are in the range of AUG discharges: elongation $\kappa = 1.8$, triangularity $\delta = 0.4$, toroidal magnetic field $B_T = 2.2$ T, toroidal plasma current $I_P = 1.0$ MA, resulting in edge safety factor values of $q_{95} \approx 5$, and normalized plasma beta $\beta_N = 1.8$ for a range of pedestal top densities $n_{\mathrm{e,ped}} = 2, 4, 6, 8$ [10^{19} m^{-3}]. The parameters were chosen such that, depending on the pedestal density, the stability boundary is limited by kink-peeling or ballooning modes. In order to study the impact of MP fields on the stability of the generated axisymmetric model equilibria,

we add a field-aligned corrugation with a periodicity of $N_P = 2$ and a maximum magnitude of 12 mm to the plasma boundary and calculate the fixed-boundary equilibrium for the corrugated plasma geometry using the GVEC equilibrium code [43]. The corrugation is selected such that its poloidal distribution and magnitude is similar to the corrugation induced by realistic MP coil configurations (see figure 6.7). This approach allows the impact of MP fields on MHD stability to be studied isolated from any MP-induced changes in transport. Model pressure and safety factor profiles as well as a corrugated plasma boundary are shown in figure 6.1.

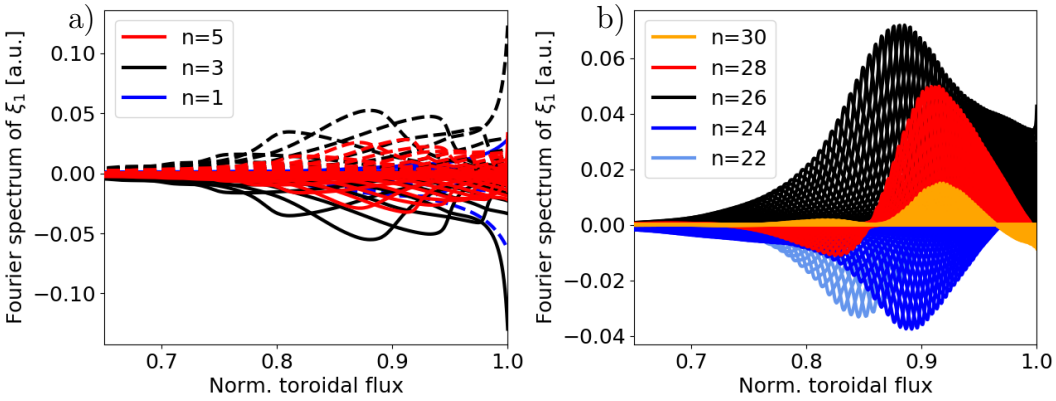

Figure 6.2: Complex (solid) and complex-conjugate (dashed) Fourier harmonics (m, n) of the radial flux-surface displacement ξ_1 of an $n^* = 3$ (a) and an $n^* = 26$ (b) peeling-ballooning instability. The harmonics are colored by their toroidal mode number n. For visibility, only three toroidal harmonics of the $n^* = 3$ instability are shown. Note that there is no contribution of complex-conjugate harmonics to the high-n instability (b) as described in chapter 5 [63].

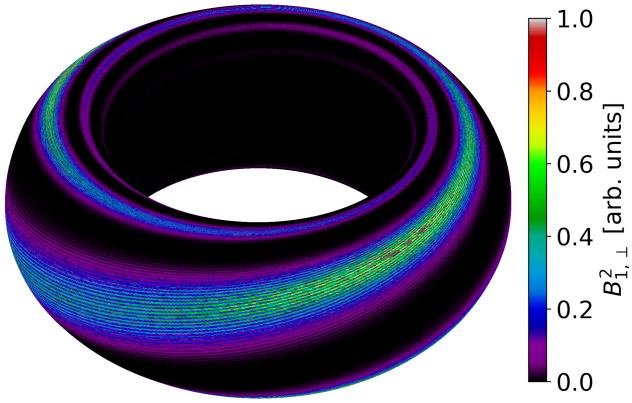

Figure 6.3: Square of the perpendicular magnetic field perturbation $\boldsymbol{B}^2_{1,\perp}$ for an $n^* = 50$ instability in toroidal geometry. In this context, perpendicular refers to the equilibrium magnetic field $\boldsymbol{B}_0$.

The MHD stability of the generated axisymmetric and corrugated equilibria is analyzed using the CASTOR3D code. The computational improvements of the CASTOR3D code, discussed in chapter 3, allow for the first time to study instabilities of high toroidal mode number $n \approx 20-60$ in non-axisymmetric tokamak plasmas with realistic safety factor profiles. Moreover, these improvements significantly reduce the computational cost for the study of intermediate- to high-n instabilities ($n > 5$) by $1-2$ orders of magnitude. The Fourier harmonics of a low-n^* and high-n^* instability in a non-axisymmetric tokamak plasma are shown in figure 6.2.

The different ballooning mode structures of the contributing toroidal harmonics, which are coupled together to a single peeling-ballooning mode. The high-n^* instabilities seem to couple over a wider range of toroidal harmonics compared to the low-n^* instabilities (see colored lines/crosses in figure 3.6 on page 25). As in the case of poloidal mode localisation, multiple toroidal harmonics increase the toroidal and, consequently, the helical localisation of the ballooning modes by superposition, which is shown for an $n^* = 50$ ballooning mode in figure 6.3. The helical localisation of edge localized modes relative to the equilibrium corrugation has been observed in experiments with MP field [24] and is well reproduced by CASTOR3D [63]. The increase of helical localisation with an increasing number of toroidal harmonics of ballooning modes in magnetically perturbed plasmas was also found with perturbative approaches [31]. The low-n^* instabilities, which correspond to non-degenerate eigenvalue pairs, couple to the complex-conjugate harmonics to form strictly locked external kink or peeling-ballooning modes as described in chapter 5 [63].

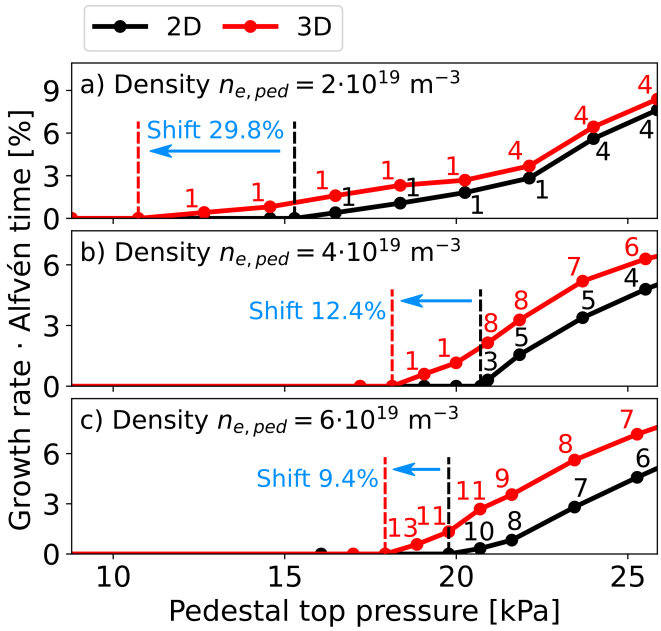

Figure 6.4: Growth rates of the most unstable instability over a range of axisymmetric (black) and corrugated (red) equilibria with different pedestal top pressure for pedestal top densities of $n_{\mathrm{e,ped}} = 2 \cdot 10^{19}$ m^{-3} (a) to $n_{\mathrm{e,ped}} = 6 \cdot 10^{19}$ m^{-3} (c). The numbers which annotate the data points refer to the (dominating) toroidal harmonic n^* of the most unstable instability.

Evaluating growth rates for a series of equilibria with varying pedestal top pressure reveals that the destabilization caused by the corrugated flux surface geometry results in a shift of the stability boundary, i.e. the critical pedestal top pressure. This is shown for low-n limited low density to high-n limited high density pressure scans in figures 6.4 and 6.5a. The shift observed for the low density case, where ELM suppression is observed, is in good agreement with experimental findings, which report a shift of $\sim$30% [21]. In all observed cases, the dominating toroidal mode number n^* of the most unstable instability of the corrugated equilibrium is close to the most unstable toroidal mode number of the axisymmetric equilibrium. At the highest observed density (figure 6.5a) the stability limit is determined by high-n instabilities with $n^* \gtrapprox 100$. Close to the stability threshold, the toroidal mode number of the most unstable instability strongly increases as can be seen in figure 6.5b. In order to resolve these high-n ballooning modes an extremely high radial resolution is required.

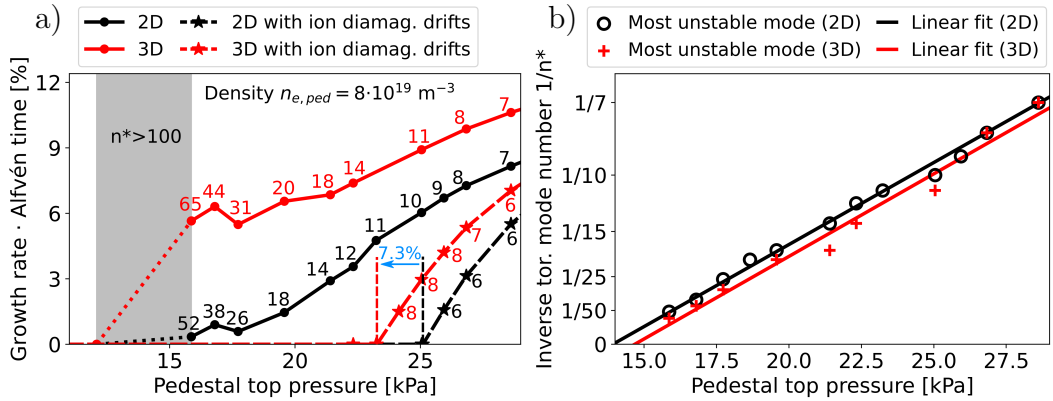

Figure 6.5: (a) Growth rates of the most unstable instability over a range of axisymmetric (black) and corrugated (red) equilibria with different pedestal top pressure for a pedestal top density of $n_{\mathrm{e,ped}} = 8 \cdot 10^{19}$ m^{-3}. The numbers which annotate the data points refer to the (dominating) toroidal harmonic n^* of the most unstable instability. The gray area marks a region where high-n ballooning modes with $n^* \gtrapprox 100$ are destabilized. (b) Inverse of the dominating toroidal mode number, $1/n^*$, of the fastest growing instability over a range of axisymmetric (black) and corrugated (red) equilibria with different pedestal top pressures.

However, since the structure of the modes becomes comparable to the gyro-radius for $n \to \infty$, these instabilities violate the MHD assumptions discussed in chapter 2. The high-n ballooning modes are known to be strongly stabilized by gyroviscosity, i.e. ion diamagnetic drift effects, [67, 68, 69]. For this reason, ion diamagnetic drift effects must be included in the stability calculations in order to accurately describe the stability in the high density case. Ion diamagnetic drift effects were recently implemented into the CASTOR3D code [34], allowing the analysis of these effects in non-axisymmetric tokamak plasmas for the first time. Similar to the axisymmetric case, the ion diamagnetic drift strongly stabilizes the high-n instabilities also for non-axisymmetric configurations. Consequently, the stability limit including ion diamagnetic drift effects is described by intermediate-n^* peeling-ballooning modes. The resulting shift of the stability boundary for the high density case due to symmetry breaking is about $\sim 7\%$. In summary, symmetry-breaking results in a shift of the stability threshold which is of the order of $\sim 10\%$ and both the absolute and relative destabilization become weaker at higher densities.

The mechanisms which cause the destabilizing effect of MP fields are generally complex, since the stability of a mode is determined by the fine balance of various strongly stabilizing and destabilizing effects. This becomes clear from the energy functional, where the growth rate of a perturbation is determined by the sum of the stabilizing and destabilizing energy terms, which are usually $1 - 2$ orders of magnitude larger than their sum. Consequently, small changes to the energetic drives can result in large changes of the growth rate. However, a simplified explanation might be obtained considering the results from chapter 5. The non-axisymmetric MP fields result in regions which are favourable or unfavourable for certain types of instability. In the case of magnetically perturbed tokamak plasmas, these perturbations are usually roughly aligned with the magnetic field lines. For this reason, instabilities, which are typically also aligned with the magnetic field lines, can optimize their toroidal position with respect to the toroidally favourable regions. This provides an intuitive, but strongly simplified, reasoning of the effect of MP fields on the growth rate of MHD instabilities. This reasoning can be applied to describe the effect of

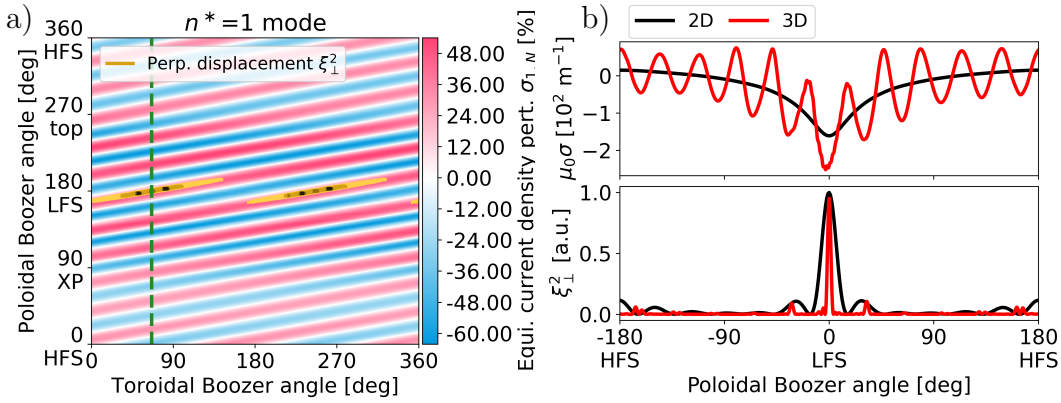

Figure 6.6: (a) Normalized perpendicular displacement relative to the non-axisymmetric component of the parallel current-density $\sigma_{1,N}$, as defined in equation 5.6, at the most unstable flux surface $s = 1.0$ w.r.t. δW_{CUR} for the $n^* = 1$ external kink mode. (b) Parallel equilibrium current-density factor $\sigma = (\boldsymbol{j}_0 \cdot \boldsymbol{B}_0)/\boldsymbol{B}_0^2$ and normalized perpendicular displacement $\boldsymbol{\xi}_\perp^2$ for an axisymmetric (black) and the corresponding corrugated (red) equilibrium at the toroidal angle for which the perpendicular displacement is largest indicated by the dashed green line in (a).

MP fields on the growth rate in the simple case of an $n^* = 1$ external kink mode. The purely current-driven $n^* = 1$ mode, shown in figure 6.6a, is helically localized in the regions of augmented parallel current-density (magenta area in figure 6.6a) in order to maximize its growth rate. The poloidal localization of the n instability is shown relative to the parallel equilibrium current-density factor $\sigma = (\boldsymbol{j}_0 \cdot \boldsymbol{B}_0)/\boldsymbol{B}_0^2$ in figure 6.6b. The symmetry-breaking results in regions of strongly amplified and weakened current-density compared to the axisymmetric case. Consequently, the current-driven external kink mode can maximize its current-density drive δW_{CUR} by localizing in the regions of augmented parallel current-density.

6.2 Stability analysis of AUG discharges

Furthermore, results of the non-axisymmetric MHD stability analysis of two experimental equilibria from the AUG pulses #40180 (ELM suppression) and #40181 (ELM mitigation) are presented. In both discharges, the same MP coil currents with a periodicity of $N_P = 2$ were applied. However, the ELM mitigation discharge was achieved by adding gas to raise the density above the empirically observed density threshold for ELM suppression [21]. As a consequence the edge pressure is also higher. The equilibria were reconstructed from magnetic measurements using the CLISTE code [41]. The non-axisymmetric free-boundary equilibria were calculated from the experimentally measured pressure and safety factor profiles and the coil currents using the NEMEC code [40, 42], followed by a refinement with the GVEC code [43]. Pressure and safety factor profiles as well as cross-sections of the corrugated plasma boundaries are shown in figure 6.7. The corrugation caused by the MP fields is 7 mm for the ELM suppression and 13 mm for the ELM mitigation case at the low-field side, which has been tested against local measurements of the distorted boundary. The larger corrugation of the ELM mitigation case is caused by the larger pressure gradient which leads to a stronger plasma response to the same externally applied MP field.

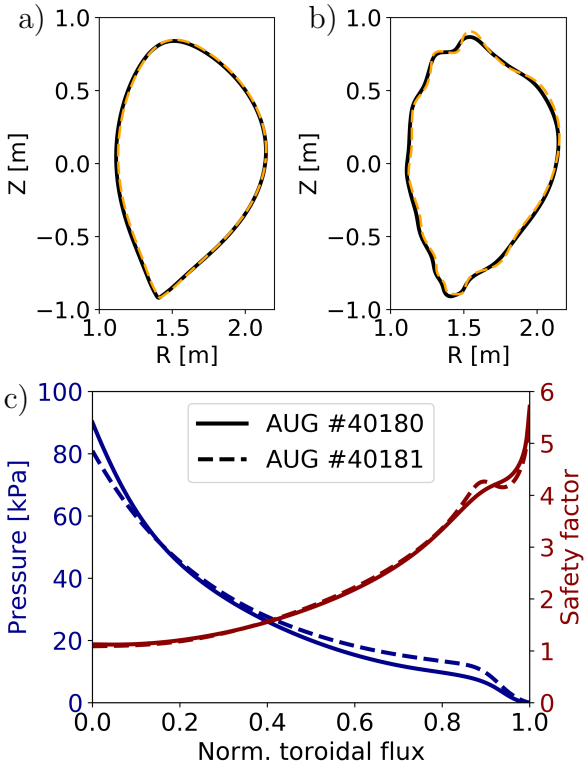

Figure 6.7: Toroidal cross-sections of the plasma boundary for the axisymmetric (a) and magnetically perturbed (b) equilibria of the experiments AUG#40180 (solid, black) and AUG#40181 (dashed, orange) as well as pressure and safety factor profiles (c). For visibility, the corrugation of (b) is amplified by a factor of 2.5.

For AUG#40181, we find a range of unstable modes, which is in agreement with the observed ELM activity. The most unstable MHD instabilities predicted by linear MHD are all in the intermediate toroidal mode number range $n^* = 15 \sim 17$. For the ELM suppression case AUG#40180, no MHD instabilities were found by linear MHD stability analysis, indicating that no ELM activity is expected.

In order to analyze the transition from ELM mitigation to ELM suppression, we create a range of equilibria with an increasing edge pressure from AUG#40180 to AUG#40181 by linear interpolation of the density profiles of the two discharges in similarity to the experimentally observed density pump-out. The results of the stability analysis of the pressure scan between AUG#40180 to AUG#40181 are shown in figure 6.8. In similarity to the results shown in figure 6.4, we observe a shift of the critical edge pressure by 9%. The ELM suppression discharge is below the stability threshold lowered by the MP coils, while the ELM mitigation case is strongly unstable even without symmetry-breaking. The impact on the growth rate by symmetry-breaking weakens at higher pressures and densities until it nearly vanishes for AUG#40181, which seems to imply that ELM mitigation is not connected to a MHD destabilization of the plasma. However, while pure ideal MHD is usually sufficient to roughly describe the experimentally observed critical pressure and its trends, a precise prediction of the ELM onset might require the inclusion of further physical effects [69]. One can clearly see that ion diamagnetic drift effects result in a strong stabilization of the axisymmetric equilibria, resulting in a good agreement with the empirical stability threshold from Ref. [21]. Consequently, AUG#40181 is just slightly above both the predicted and empirical stability threshold. The effect of ion diamagnetic drifts is weaker in the non-axisymmetric case, which implies that - considering drift effects - the ELM mitigation discharge is destabilized by symmetry-breaking. The remaining difference between the empirical and the predicted stability boundary might be caused by further effects which have been neglected in this stability analysis such as equilibrium flow. In conclusion, we have shown that linear MHD predicts a destabilization due to the application of MP fields

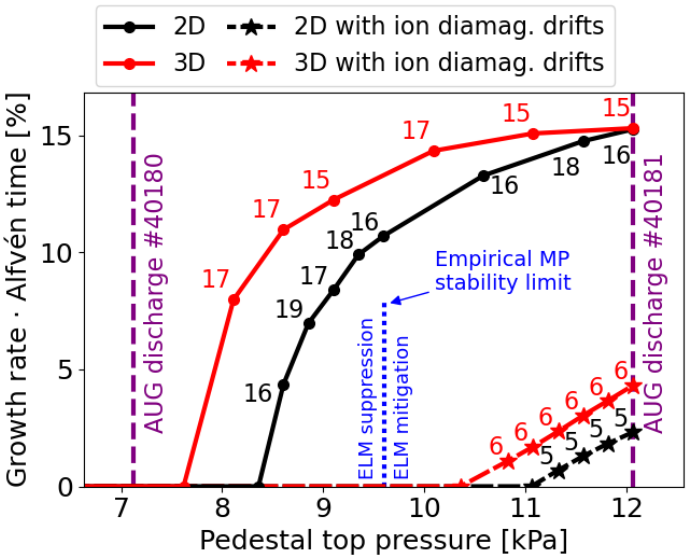

Figure 6.8: Growth rates for a range of equilibria between AUG discharges #40180 and #40181 with and without ion diamagnetic drift effects. The numbers annotating the data points refer to the (dominating) toroidal harmonic n^* of the most unstable instability. The dotted blue line indicates the empirical stability limit from Ref. [21], assuming equal ion and electron pressure.

in agreement with experimental observations. We have highlighted the importance of ion diamagnetic drift effects for the accurate description of the stability threshold and a simplified explanation for the generally highly complex destabilization mechanism was presented.

7 Summary and outlook

In this thesis, the CASTOR3D code, which solves the linearized extended MHD equations in general curvilinear coordinates, has been optimized for the analysis of edge localized instabilities in tokamaks. Then, the optimized CASTOR3D code was applied to study the effect of symmetry-breaking by MP fields on MHD stability. Several phenomena such as mode localization, mode locking and destabilization due to MP fields were investigated.

7.1 Optimization of the COTRANS and CASTOR3D codes

In order to accurately study MHD instabilities in the strongly shaped edge region of tokamak plasmas, high-resolution mappings from the coordinate system of the equilibrium code to straight field line coordinates, which are beneficial for stability analysis, are necessary. For this reason, the parallelization of the COTRANS code, which is the interface between equilibrium codes and CASTOR3D, has been optimized and Fourier transforms have been replaced by Fast Fourier Transform algorithms. As a result, the CPU time for the high-resolution mappings could be reduced by orders of magnitude, enabling the precise stability analysis of strongly shaped equilibria. The speedup is predominantly due to the implementation of the Fast Fourier Transform algorithms, reducing the computational complexity from $\mathcal{O}(N_M^2 N_N^2)$ to $\mathcal{O}(N_M N_N \log(N_M N_N))$, where N_M and N_N are the numbers of poloidal and toroidal grid points used to map the equilibrium.

Furthermore, eigenfunctions which have sets of individual Fourier harmonics on each flux surface were implemented into the matrix of the CASTOR3D code. This allows the set of Fourier harmonics to include only locally relevant harmonics which approximately fulfill the resonance condition 2.35. As a result, the memory requirement of the CASTOR3D code for intermediate to high-n edge localized modes ($n \gtrapprox 5$) in tokamaks could be approximately reduced from $\mathcal{O}((n\Delta q)^2)$ to $\mathcal{O}(1)$. These improvements allow for the resource efficient study of edge localized instabilities and enable the stability analysis of high-n edge localized instabilities ($n \gtrapprox 20$) in realistic non-axisymmetric tokamak plasma, where $\Delta q \approx 4$ or higher, with CASTOR3D. In addition, new radial grids based on the localization of the resonant flux surfaces were implemented. These grids naturally resolve the radial structure of the eigenfunctions and are especially beneficial to resolve the high-n ballooning modes.

7.2 Energy decomposition for resistive and ideal plasma perturbations

In chapter 4, an energetic decomposition for resistive plasma instabilities was derived based on the intuitive form of the energy functional of ideal MHD by Greene and Johnson [49]. The energy functional yields a decomposition of the energy of a perturbation into energy terms related to different stabilizing and destabilizing phenomena. This energy decomposition contributes to the physical interpretation and understanding of instabilities as demonstrated in chapters 5 and 6 as well as Ref. [34]. The resistive energy functional contains three additional energy terms (W_{RCD}, $W_{\mathrm{RD},\parallel}$, $W_{\mathrm{RD},\perp}$) as well as a correction to the stabilizing magneto-compressional energy term (W_{CPA}) related to resistive diffusion. The energy densities can be expressed in their physical form, encoding the energy density of the instability at a certain phase, or in their complex form, encoding the phase average of the energy density.

The physical and complex terms of the intuitive form of the energy functional for ideal and resistive plasma perturbations have been implemented in the CASTOR3D code in general curvilinear coordinates. The energy functional has been verified on a numerical test case, showing excellent numerical equality of potential and kinetic energy for three different coordinate systems. In order to obtain energy decomposition where the potential and kinetic energy terms are equal, both a well-converged equilibrium and a well-resolved eigenfunction are required. This is especially the case for resistive instabilities, since the current diffusion energy term W_{RCD} is strongly dependent on a well-resolved eigenfunction. The analysis of the test case reveals that, for realistic values of the resistivity, the resistive corrections can significantly affect the energetic decomposition compared to the ideal energy functional. Furthermore, studying trends in the localization of the energy density, it was shown that the perturbation shifts away from the midplane as resistivity increases. In conclusion, the newly implemented energetic decomposition provides increased insight into mechanisms which drive or stabilize ideal/resistive modes compared to the analysis of trends in growth rates and perturbed quantities.

7.3 Helical mode localization and mode locking

In chapter 5, it has been discussed how the phenomena of helical localization and locking of instabilities in magnetically perturbed tokamak plasmas are related to the arbitrary complex phase or phase angle of linear solutions. In general, the arbitrary phase angle of a solution of the linear MHD equations encodes all possible structures and localizations of the instability. In the case of axisymmetry, this freedom is reflected in the arbitrary toroidal position of the modes. Hence, in order to analyze the localization or locking of modes, it is necessary to evaluate the position of the instability for all values of the arbitrary solution phase. We have shown that the localization or locking of instabilities can be separated into two types: strictly locked and quasi-locked instabilities. Both types of localization can be identified by various characteristics summarized in table 7.1.

	Quasi-locked	**Strictly locked**
$\Omega_0 = 0$	Mode amplitude determined by an envelope; position of fine mode structure not fixed	Only one possible mode location; the mode structure is fixed
$\Omega_0 > 0$	Mode rotates for any Ω_0 under its envelope	Rotation only above critical threshold $\Omega_0 > \Omega_{\mathrm{crit}}$
$\Omega_0 > 0$	Nearly uniform rotation for any $\Omega_0 > 0$	Locked/non-rotating ($\Omega_0 < \Omega_{\mathrm{crit}}$) Forced non-uniform rotation ($\Omega_0 > \Omega_{\mathrm{crit}}$)
$\Omega_0 \geq 0$	Two degenerate (*) eigenvalues for each n^*	Two non-degenerate eigenvalues for each n^* ($\Omega_0 < \Omega_{\mathrm{crit}}$)

Table 7.1: Summary of the major differences between quasi-locked and strictly locked linear MHD instabilities in rotating ($\Omega_0 > 0$) and non-rotating/flow-free ($\Omega_0 = 0$) non-axisymmetric plasmas. (*) We define two (complex) eigenvalues $\lambda_1 = \gamma_1 + i\omega_1$ and $\lambda_2 = \gamma_2 + i\omega_2$ as degenerate if $\gamma_1 = \gamma_2$ and $|\omega_1| = |\omega_2|$. From Ref. [63].

Strictly locked modes, for which there is no change in the position for any value of the solution phase, correspond to pairs of non-degenerate eigenvalues. It has been demonstrated that the pair of non-degenerate solutions describes a fast growing instability, which is located in an energetically favourable position, and a slow growing instability, which is in an energetically unfavourable position. Strictly locked

instabilities are built of coupled toroidal harmonics of opposite sign (left- and right-traveling waves), i.e. $n \leftrightarrow -n$, and thus can only be found in the mode families of N_P and $N_P/2$ where N_P is the toroidal periodicity of the system. Furthermore, we demonstrated that strictly locked instabilities with a dominating toroidal harmonics $n^* = N/2$ naturally localize at a favourable position with respect to the equilibrium harmonic N.

Instabilities which cannot strictly lock to the equilibrium are quasi-locked. These instabilities correspond to the degenerate eigenvalues and involve no coupling of toroidal Fourier harmonics of opposite sign n and $-n$. It has been shown that, while the precise localization of the quasi-locked modes depends on the solution phase, the envelope of the location over all the possible phase angles is helically localized in an energetically favourable region in order to maximize the growth rate of the instability.

We demonstrated that, in rotating plasmas, strictly locked modes only rotate if the plasma rotation exceeds a critical threshold. If the threshold is exceeded, the rotation of the strictly locked modes is forced and strongly non-uniform. Further increasing the plasma rotation, eventually results in an increasingly uniform rotation of the instability. Quasi-locked modes start rotating beneath their envelope in a nearly uniform motion at any finite value of the plasma rotation. The behaviour of the instabilities at finite plasma rotation yields an intuitive understanding of strictly and quasi-locked instabilities.

It has been shown that current-density driven instabilities preferably align with regions of augmented parallel equilibrium current-density whereas pressure-gradient driven instabilities preferably align with regions of increased "bad curvature". While these two equilibrium properties describe the alignment of strongly current-density driven or pressure-gradient driven instabilities, in general the stability of an MHD mode is determined by a delicate balance between the current-density drive, the pressure-gradient drive and the stabilizing energy terms (see [49, 58]). For this reason, the position of an MHD instability is generally a complex compromise between the favourable alignments w.r.t equilibrium current-density and "bad curvature". In order to determine the precise localization of a general finite-n MHD instability, a detailed numerical stability analysis of the corresponding MHD equilibrium is required.

Finally, the helical localization predicted by linear MHD has been compared to experimental measurements of the helical localization obtained from the Electron Cyclotron Emission (ECE) diagnostic. As a result, the numerically determined MHD instabilities are located at the same helical position as observed in the experiment, which verifies that the localization of the observed instabilities is well-described by linear ideal MHD.

7.4 Destabilization by symmetry-breaking

In chapter 6, it has been shown for the first time that linear MHD predicts a decrease of the critical pedestal top pressure caused by symmetry-breaking due to the application of MP fields. The predicted destabilization is in good agreement with experimental observations. It was found that symmetry-breaking has the strongest impact on the operational space, when the plasma is prone to edge instabilities with lower toroidal mode number. The application of MP fields roughly preserves the range of toroidal harmonics corresponding to the most unstable instabilities. For

the first time, coupled high-n ballooning modes were described by linear MHD in realistic non-axisymmetric tokamak geometry. Similar to the axisymmetric case, these high-n instabilities were shown to be strongly stabilized by ion diamagnetic drift effects. Finally, a simplified explanation of the destabilization was provided by the localization of the MHD instabilities in energetically favourable regions of the non-axisymmetric tokamak plasma.

Results on the stability analysis of two experimental discharges, a mitigated and a suppressed ELM scenario, indicate that linear MHD is able to describe the effects of MPs on pedestal stability if ion diamagnetic drift effects are considered. The ELM mitigation equilibrium was found to be unstable to a range of low- to intermediate-n^* instabilities, while the ELM suppression case was found to be MHD stable.

7.5 Future work

While in this work, the fundamental mechanisms of mode localization, mode locking and destabilization due to the application of MP fields were discussed, future analysis might focus on the impact of the MP field strength or MP field configurations on these phenomena. Moreover, the influence of further physical effects such as equilibrium plasma flow and resistivity on the predicted shift of the critical pressure caused by the application of MP fields might be studied.

Future research might focus on the predictive stability analysis of MP ELM suppression scenarios for future fusion devices such as ITER, DEMO or SPARC. Furthermore, the impact of ion diamagnetic drifts, which are naturally included in the extended MHD equations of CASTOR3D, or other non-ideal effects on MHD instabilities in future (high-field) tokamaks might be studied. In this context, the CASTOR3D code might also be coupled to predictive stability frameworks, which include transport models that predict the kinetic profiles.

In addition, future work could focus on the integration of synthetic diagnostics, i.e. simulated measurements, such as magnetic probes or ECE into the CASTOR3D code in order to increase the accuracy of comparisons with experimental measurements. Synthetic diagnostics mimic the process of experimental measurements based on the simulated results. In the case of magnetic measurements, this would for example require to calculate the magnetic field in the vacuum region and the resulting induced currents in the measurement coil structures considering mirror currents in the conducting structures near the measurement coils.

A Derivation of mode coupling in the strong formulation

The criterion for mode coupling 2.25 was derived from the weak form. In the weak form, the coupling of Fourier harmonics is represented by non-vanishing cross-terms in the linear MHD matrix elements. However, mode coupling can already be deduced from the linear MHD equations in their original form 2.20. For $\rho_0 > 0$ and $\lambda \neq 0$, the linear MHD equations can be written in the form:

$$\boldsymbol{\chi} = \mathcal{F}\boldsymbol{\chi} \quad \text{with} \quad \mathcal{F} = \lambda^{-1}\mathcal{S}^{-1}\mathcal{R} \tag{A.1}$$

where $\mathcal{F}$ is a linear differential operator that depends only on equilibrium quantities. Expressing the eigenfunction and force operator in a Fourier representation yields:

$$\begin{aligned}
\boldsymbol{\chi}_{\widetilde{m},\widetilde{n}} &= \int_0^1\int_0^1 e^{-2\pi i(\widetilde{m}u+\widetilde{n}v)}\boldsymbol{\chi}\ \mathrm{du}\ \mathrm{dv} = \int_0^1\int_0^1 e^{-2\pi i(\widetilde{m}u+\widetilde{n}v)}\mathcal{F}\boldsymbol{\chi}\ \mathrm{du}\ \mathrm{dv} \\
&= \sum_{m,n}\int_0^1\int_0^1 e^{-2\pi i(\widetilde{m}u+\widetilde{n}v)}\mathcal{F}(\boldsymbol{\chi}_{m,n}e^{2\pi i(mu+nv)})\ \mathrm{du}\ \mathrm{dv} \\
&= \sum_{m,n}\int_0^1\int_0^1 e^{-2\pi i(\widetilde{m}u+\widetilde{n}v)}e^{2\pi i(mu+nv)}\mathcal{F}^{m,n}(\boldsymbol{\chi}_{m,n})\ \mathrm{du}\ \mathrm{dv} \\
&= \sum_{m,n,M,N}\widehat{\mathcal{F}}^{m,n}_{M,N}\boldsymbol{\chi}_{m,n}\int_0^1\int_0^1 e^{-2\pi i(\widetilde{m}u+\widetilde{n}v)}e^{2\pi i(Mu+Nv)}e^{2\pi i(mu+nv)}\ \mathrm{du}\ \mathrm{dv}
\end{aligned} \tag{A.2}$$

where $\widehat{\mathcal{F}}^{m,n}_{M,N}$ and $\boldsymbol{\chi}_{m,n}$ are the Fourier coefficients of the force operator and eigenfunction respectively. Since the Fourier coefficients $\widehat{\mathcal{F}}^{m,n}_{M,N}$ contain radial derivatives, they are still differential operators. However, the toroidal and poloidal dependence of $\mathcal{F}^{m,n}$, which originates in the equilibrium quantities and geometry, is encoded by the Fourier decomposition. Moreover, toroidal and poloidal derivatives acting on the eigenfunction are represented in $\mathcal{F}^{m,n}$ by multiplication with n or m respectively, which results in the mode number dependence of $\mathcal{F}^{m,n}$. The derived equation results in the same coupling constraint as obtained from the weak form 2.25. In the case of axisymmetry, $\widehat{\mathcal{F}}^{m,n}_{M,N}$ is zero for all $N \neq 0$. Then, the integral would vanish for all $n \neq \widetilde{n}$. Hence, the value of $\boldsymbol{\chi}_{\widetilde{m},\widetilde{n}}$ is independent of all $\boldsymbol{\chi}_{m,n}$ with $n \neq \widetilde{n}$, which implies that the toroidal harmonics are uncoupled. If $\widehat{\mathcal{F}}^{m,n}_{M,N}$ is finite for $(M,N) = (M_0,N_0)$, then $\boldsymbol{\chi}_{\widetilde{m},\widetilde{n}}$ is coupled to the values of $\boldsymbol{\chi}_{M_0+\widetilde{m},N_0+\widetilde{n}}$.

Acronyms

AUG	ASDEX Upgrade: Tokamak located in Garching, Germany
BZR	Boozer coordinates: Coordinates in which the magnetic field lines appear straight
CAS3D	Ideal linear MHD code for (non-)axisymmetric plasmas
CASTOR3D	Extended linear MHD code for (non-)axisymmetric plasmas
CLISTE	Interpretative equilibrium solver for tokamak plasmas
COTRANS	Interface between equilibrium codes and CASTOR3D
DEMO	Demonstration power plant foreseen as a successor of ITER
ECE	Electron Cyclotron Emission spectroscopy
ELM	Edge Localized Mode
FFT	Fast Fourier Transform
GVEC	MHD equilibrium code for (non-)axisymmetric plasmas
H-mode	High confinement mode
IPED2	Predictive pedestal stability framework
ITER	Future fusion experiment under construction in Cadarache, France
LCFS	Last Closed Flux Surface
L-mode	Low confinement mode
MCF	Magnetic confinement fusion
MHD	Magnetohydrodynamics: Fluid description of the plasma
MP	Magnetic perturbation
NEM	Coordinates used by the NEMEC equilibrium code
NEMEC	MHD equilibrium code for (non-)axisymmetric plasmas
SFL	2D straight field line coordinates: Coordinates in which the magnetic field lines appear straight
SPARC	Future fusion experiment under construction in Devens, Massachusetts, United States
STARWALL	Code for the calculation of the vacuum magnetic field response

References

[1] Energy Information Agency (EIA), "International Energy Outlook 2021 (IEO2021)," 2021. https://www.eia.gov/outlooks/ieo (accessed: 10.10.2023).

[2] IPCC, *Climate Change 2023: Synthesis Report. Contribution of Working Groups I, II and III to the Sixth Assessment Report of the Intergovernmental Panel on Climate Change [Core Writing Team, H. Lee and J. Romero (eds.)].* Geneva, Switzerland: IPCC, 2023.

[3] Energy Institute, *2023 Statistical Review of World Energy (72nd edition).* London, UK: Energy Institute, 2023. https://www.energyinst.org/statistical-review (accessed: 10.10.2023).

[4] A. C. Phillips, *The physics of stars*, ch. 4 - Thermonuclear fusion in stars. Chichester: John Wiley & Sons, 1994.

[5] J. Wesson, *Tokamaks - Third Edition.* Oxford: Clarendon Press, 2004.

[6] S. Atzeni and J. Meyer-Ter-Vehn, *The Physics of Inertial Fusion: Beam Plasma Interaction, Hydrodynamics, Hot Dense Matter*, ch. 1 - Nuclear fusion reactions. Oxford: Clarendon Press, 2004.

[7] J. P. Freidberg, *Plasma Physics and Fusion Energy*, ch. 4 - Power balance in a fusion reactor. Cambridge: Cambridge University Press, 2008.

[8] S. E. Wurzel and S. C. Hsu, "Progress toward fusion energy breakeven and gain as measured against the Lawson criterion," *Physics of Plasmas*, vol. 29, no. 6, p. 062103, 2022.

[9] J. P. Freidberg, *Ideal Magnetohydrodynamics.* New York and London: Plenum Press, 1987.

[10] S. I. Braginskii, "Transport processes in a plasma," *Reviews of plasma physics*, vol. 1, p. 205, 1965.

[11] H. Zohm, "Plasma performance, burn and sustainment," in *Magnetic Fusion Energy* (G. H. Neilson, ed.), Woodhead Publishing, 2016.

[12] F. Wagner, G. Becker, K. Behringer, D. Campbell, A. Eberhagen, W. Engelhardt, G. Fussmann, O. Gehre, J. Gernhardt, G. v. Gierke, G. Haas, M. Huang, F. Karger, M. Keilhacker, O. Klüber, M. Kornherr, K. Lackner, G. Lisitano, G. G. Lister, H. M. Mayer, D. Meisel, E. R. Müller, H. Murmann, H. Niedermeyer, W. Poschenrieder, H. Rapp, H. Röhr, F. Schneider, G. Siller, E. Speth, A. Stäbler, K. H. Steuer, G. Venus, O. Vollmer, and Z. Yü, "Regime of improved confinement and high beta in neutral-beam-heated divertor discharges of the ASDEX tokamak," *Physical Review Letters*, vol. 49, pp. 1408–1412, 1982.

[13] ASDEX Team, "The H-mode of ASDEX," *Nuclear Fusion*, vol. 29, no. 11, p. 1959, 1989.

[14] H. Zohm, "Edge localized modes (ELMs)," *Plasma Physics and Controlled Fusion*, vol. 38, no. 2, p. 105, 1996.

[15] A. Loarte, G. Saibene, R. Sartori, D. Campbell, M. Becoulet, L. Horton, T. Eich, A. Herrmann, G. Matthews, N. Asakura, A. Chankin, A. Leonard,

G. Porter, G. Federici, G. Janeschitz, M. Shimada, and M. Sugihara, "Characteristics of type I ELM energy and particle losses in existing devices and their extrapolation to ITER," *Plasma Physics and Controlled Fusion*, vol. 45, no. 9, p. 1549, 2003.

[16] P. B. Snyder, H. R. Wilson, J. R. Ferron, L. L. Lao, A. W. Leonard, T. H. Osborne, A. D. Turnbull, D. Mossessian, M. Murakami, and X. Q. Xu, "Edge localized modes and the pedestal: A model based on coupled peeling-ballooning modes," *Physics of Plasmas*, vol. 9, no. 5, pp. 2037–2043, 2002.

[17] H. R. Wilson, S. C. Cowley, A. Kirk, and P. B. Snyder, "Magneto-hydrodynamic stability of the H-mode transport barrier as a model for edge localized modes: an overview," *Plasma Physics and Controlled Fusion*, vol. 48, no. 5A, p. A71, 2006.

[18] Y. Liang, H. R. Koslowski, P. R. Thomas, E. Nardon, B. Alper, P. Andrew, Y. Andrew, G. Arnoux, Y. Baranov, M. Bécoulet, M. Beurskens, T. Biewer, M. Bigi, K. Crombe, E. De La Luna, P. de Vries, W. Fundamenski, S. Gerasimov, C. Giroud, M. P. Gryaznevich, N. Hawkes, S. Hotchin, D. Howell, S. Jachmich, V. Kiptily, L. Moreira, V. Parail, S. D. Pinches, E. Rachlew, and O. Zimmermann, "Active control of type-I edge-localized modes with $n = 1$ perturbation fields in the JET tokamak," *Physical Review Letters*, vol. 98, p. 265004, 2007.

[19] W. Suttrop, T. Eich, J. C. Fuchs, S. Günter, A. Janzer, A. Herrmann, A. Kallenbach, P. T. Lang, T. Lunt, M. Maraschek, R. M. McDermott, A. Mlynek, T. Pütterich, M. Rott, T. Vierle, E. Wolfrum, Q. Yu, I. Zammuto, and H. Zohm, "First observation of edge localized modes mitigation with resonant and nonresonant magnetic perturbations in ASDEX Upgrade," *Physical Review Letters*, vol. 106, p. 225004, 2011.

[20] T. E. Evans, R. A. Moyer, P. R. Thomas, J. G. Watkins, T. H. Osborne, J. A. Boedo, E. J. Doyle, M. E. Fenstermacher, K. H. Finken, R. J. Groebner, M. Groth, J. H. Harris, R. J. La Haye, C. J. Lasnier, S. Masuzaki, N. Ohyabu, D. G. Pretty, T. L. Rhodes, H. Reimerdes, D. L. Rudakov, M. J. Schaffer, G. Wang, and L. Zeng, "Suppression of large edge-localized modes in high-confinement DIII-D plasmas with a stochastic magnetic boundary," *Physical Review Letters*, vol. 92, p. 235003, 2004.

[21] W. Suttrop, A. Kirk, V. Bobkov, M. Cavedon, M. Dunne, R. M. McDermott, H. Meyer, R. Nazikian, C. Paz-Soldan, D. A. Ryan, E. Viezzer, M. Willensdorfer, the ASDEX Upgrade Team, and the MST1 Team, "Experimental conditions to suppress edge localised modes by magnetic perturbations in the ASDEX Upgrade tokamak," *Nuclear Fusion*, vol. 58, no. 9, p. 096031, 2018.

[22] T. Eich, B. Sieglin, A. J. Thornton, M. Faitsch, A. Kirk, A. Herrmann, and W. Suttrop, "ELM divertor peak energy fluence scaling to ITER with data from JET, MAST and ASDEX upgrade," *Nuclear Materials and Energy*, vol. 12, pp. 84–90, 2017. Proceedings of the 22nd International Conference on Plasma Surface Interactions 2016, 22nd PSI.

[23] I. T. Chapman, W. A. Cooper, A. Kirk, C. J. Ham, J. R. Harrison, A. Patel, S. D. Pinches, R. Scannell, A. J. Thornton, and the MAST Team, "Three-dimensional corrugation of the plasma edge when magnetic perturbations are

applied for edge-localized mode control in MAST," *Plasma Physics and Controlled Fusion*, vol. 54, no. 10, p. 105013, 2012.

[24] M. Willensdorfer, T. B. Cote, M. Griener, D. A. Ryan, E. Strumberger, W. Suttrop, N. Wang, M. Cavedon, S. S. Denk, M. Dunne, R. Fischer, J. Galdon-Quiroga, C. J. Ham, C. C. Hegna, M. Hoelzl, A. Kirk, M. Maraschek, F. Mink, N. Leuthold, F. Orain, E. P. Seliunin, H. Zohm, the ASDEX Upgrade Team, and the MST1 Team, "Dynamics of ideal modes and subsequent ELM crashes in 3D tokamak geometry from external magnetic perturbations," *Plasma Physics and Controlled Fusion*, vol. 61, no. 1, p. 014019, 2019.

[25] T. E. Evans, M. E. Fenstermacher, R. A. Moyer, T. H. Osborne, J. G. Watkins, P. Gohil, I. Joseph, M. J. Schaffer, L. R. Baylor, M. Bécoulet, J. A. Boedo, K. H. Burrell, J. S. deGrassie, K. H. Finken, T. Jernigan, M. W. Jakubowski, C. J. Lasnier, M. Lehnen, A. W. Leonard, J. Lonnroth, E. Nardon, V. Parail, O. Schmitz, B. Unterberg, and W. P. West, "RMP ELM suppression in DIII-D plasmas with ITER similar shapes and collisionalities," *Nuclear Fusion*, vol. 48, no. 2, p. 024002, 2008.

[26] A. Kirk, Y. Liu, E. Nardon, P. Tamain, P. Cahyna, I. Chapman, P. Denner, H. Meyer, S. Mordijck, D. Temple, and the MAST team, "Magnetic perturbation experiments on MAST L- and H-mode plasmas using internal coils," *Plasma Physics and Controlled Fusion*, vol. 53, no. 6, p. 065011, 2011.

[27] M. Kim, J. Lee, W. H. Ko, S.-H. Hahn, Y. In, Y. M. Jeon, W. Suttrop, S. K. Kim, G. Y. Park, J.-W. Juhn, and J. H. Lee, "Pedestal electron collisionality and toroidal rotation during ELM-crash suppression phase under $n = 1$ RMP in KSTAR," *Physics of Plasmas*, vol. 27, no. 11, p. 112501, 2020.

[28] C. C. Hegna, "Effects of a weakly 3-D equilibrium on ideal magnetohydrodynamic instabilities," *Physics of Plasmas*, vol. 21, no. 7, p. 072502, 2014.

[29] C. J. Ham, I. T. Chapman, J. Simpson, and Y. Suzuki, "Tokamak equilibria and edge stability when non-axisymmetric fields are applied," *Plasma Physics and Controlled Fusion*, vol. 57, no. 5, p. 054006, 2015.

[30] T. B. Cote, C. C. Hegna, M. Willensdorfer, E. Strumberger, W. Suttrop, H. Zohm, and the ASDEX Upgrade team, "Helically localized ballooning instabilities in three-dimensional tokamak pedestals," *Nuclear Fusion*, vol. 59, no. 1, p. 016015, 2019.

[31] M. S. Anastopoulos Tzanis, C. J. Ham, P. B. Snyder, and H. R. Wilson, "Peeling-ballooning stability of tokamak plasmas with applied 3D magnetic fields," *Nuclear Fusion*, vol. 60, no. 10, p. 106003, 2020.

[32] E. Strumberger and S. Günter, "CASTOR3D: linear stability studies for 2D and 3D tokamak equilibria," *Nuclear Fusion*, vol. 57, no. 1, p. 016032, 2017.

[33] E. Strumberger and S. Günter, "Linear stability studies for a quasi-axisymmetric stellarator configuration including effects of parallel viscosity, plasma flow, and resistive walls," *Nuclear Fusion*, vol. 59, no. 10, p. 106008, 2019.

[34] E. Strumberger, S. Günter, K. Lackner, and J. Puchmayr, "CASTOR3D: linear magnetohydrodynamics and diamagnetic drift effects," *Journal of Plasma Physics*, vol. 89, no. 3, p. 905890309, 2023.

[35] H. Zohm, *Magnetohydrodynamic Stability of Tokamaks*. Weinheim: WILEY-VCH Verlag GmbH & Co. KGaA, 2014.

[36] D. D. Schnack, D. C. Barnes, D. P. Brennan, C. C. Hegna, E. Held, C. C. Kim, S. E. Kruger, A. Y. Pankin, and C. R. Sovinec, "Computational modeling of fully ionized magnetized plasmas using the fluid approximation," *Physics of Plasmas*, vol. 13, no. 5, p. 058103, 2006.

[37] W. Kerner, J. P. Goedbloed, G. T. A. Huysmans, S. Poedts, and E. Schwarz, "CASTOR: Normal-mode analysis of resistive MHD plasmas," *Journal of Computational Physics*, vol. 142, no. 2, pp. 271–303, 1998.

[38] I. B. Bernstein, E. A. Frieman, M. D. Kruskal, and R. M. Kulsrud, "An energy principle for hydromagnetic stability problems," *Proceedings of the Royal Society of London. Series A. Mathematical and Physical Sciences*, vol. 244, no. 1236, pp. 17–40, 1958.

[39] E. Strumberger, S. Günter, P. Merkel, S. Riondato, E. Schwarz, C. Tichmann, and H. P. Zehrfeld, "Numerical MHD stability studies: toroidal rotation, viscosity, resistive walls and current holes," *Nuclear Fusion*, vol. 45, no. 9, p. 1156, 2005.

[40] S. P. Hirshman and J. C. Whitson, "Steepest-descent moment method for three-dimensional magnetohydrodynamic equilibria," *The Physics of Fluids*, vol. 26, no. 12, pp. 3553–3568, 1983.

[41] P. J. McCarthy, P. Martin, and W. Schneider, "The CLISTE interpretive equilibrium code," *IPP Report Nr. 5/85*, 1999.

[42] S. P. Hirshman, W. I. van RIJ, and P. Merkel, "Three-dimensional free boundary calculations using a spectral Green's function method," *Computer Physics Communications*, vol. 43, no. 1, pp. 143–155, 1986.

[43] F. Hindenlang, O. Maj, E. Strumberger, M. Rampp, and E. Sonnendrücker, "GVEC: A newly developed 3D ideal MHD Galerkin Variational Equilibrium Code," 2019. Simons Collaboration on Hidden Symmetries and Fusion Energy.

[44] J. C. Fuchs, M. Dunne, R. Fischer, L. Giannone, A. Herrmann, B. Kurzan, P. de Marné, P. J. McCarthy, E. Strumberger, W. Suttrop, W. Schneider, E. Wolfrum, and the ASDEX Upgrade Team, "Equilibrium reconstruction in the presence of 3D external magnetic perturbations on ASDEX Upgrade," in *39th European Physical Society Conference on Plasma Physics and 16th International Congress on Plasma Physics. Contributed Papers.*, 2012.

[45] P. Merkel and E. Strumberger, "Linear MHD stability studies with the STARWALL code," 2015. http://arxiv.org/abs/1508.04911.

[46] G. T. A. Huysmans, J. P. Goedbloed, and W. Kerner, "Free boundary resistive modes in tokamaks," *Physics of Fluids B: Plasma Physics*, vol. 5, no. 5, pp. 1545–1558, 1993.

[47] C. Nührenberg, "Global ideal magnetohydrodynamic stability analysis for the configurational space of Wendelstein 7-X," *Physics of Plasmas*, vol. 3, no. 6, pp. 2401–2410, 1996.

[48] C. Schwab, "Ideal magnetohydrodynamics: Global mode analysis of three-dimensional plasma configurations," *Physics of Fluids B: Plasma Physics*, vol. 5, no. 9, pp. 3195–3206, 1993.

[49] J. M. Greene and J. L. Johnson, "Interchange instabilities in ideal hydromagnetic theory," *Plasma Physics*, vol. 10, no. 8, pp. 729–745, 1968.

[50] A. H. Boozer, "Establishment of magnetic coordinates for a given magnetic field," *The Physics of Fluids*, vol. 25, no. 3, pp. 520–521, 1982.

[51] J. Puchmayr, "Optimization of pedestal stability on ASDEX Upgrade," *IPP Report Nr. 2020-11*, 2020.

[52] W. A. Cooper, J. P. Graves, A. Pochelon, O. Sauter, and L. Villard, "Tokamak magnetohydrodynamic equilibrium states with axisymmetric boundary and a 3D helical core," *Physical Review Letters*, vol. 105, p. 035003, 2010.

[53] A. D. Turnbull, N. M. Ferraro, V. A. Izzo, E. A. Lazarus, J.-K. Park, W. A. Cooper, S. P. Hirshman, L. L. Lao, M. J. Lanctot, S. Lazerson, Y. Q. Liu, A. Reiman, and F. Turco, "Comparisons of linear and nonlinear plasma response models for non-axisymmetric perturbations," *Physics of Plasmas*, vol. 20, no. 5, p. 056114, 2013.

[54] E. Strumberger, S. Günter, and C. Tichmann, "MHD instabilities in 3D tokamaks," *Nuclear Fusion*, vol. 54, no. 6, p. 064019, 2014.

[55] R. Ramasamy, M. Hoelzl, S. Henneberg, E. Strumberger, K. Lackner, and S. Günter, "How well can VMEC predict the initial saturation of external kink modes in near circular tokamaks and $l = 2$ stellarators?," *Physics of Plasmas*, vol. 30, no. 6, p. 062506, 2023.

[56] A. Redl, C. Angioni, E. Belli, O. Sauter, the ASDEX Upgrade Team, and the EUROfusion MST1 Team, "A new set of analytical formulae for the computation of the bootstrap current and the neoclassical conductivity in tokamaks," *Physics of Plasmas*, vol. 28, no. 2, 2021. 022502.

[57] B. Vanovac, J. Puchmayr, R. Bielajew, M. Willensdorfer, E. Wolfrum, M. Cavedon, E. Strumberger, M. G. Dunne, W. Suttrop, and the ASDEX Upgrade Team, "Impact of toroidal rotation on the resistive ballooning modes in ASDEX Upgrade tokamak," *Plasma Physics and Controlled Fusion*, vol. 65, no. 9, p. 095011, 2023.

[58] J. Puchmayr, M. Dunne, and E. Strumberger, "An intuitive form of the energy functional for resistive plasma perturbations," *Journal of Plasma Physics*, vol. 88, no. 5, p. 905880512, 2022. doi: 10.1017/S0022377822000915.

[59] H. Tasso, "Energy principle for resistive perturbations in tokamaks," *Plasma Physics*, vol. 19, no. 2, p. 177, 1977.

[60] H. Tasso and J. T. Virtamo, "Energy principle for 3-d resistive instabilities in shaped-cross-section tokamaks," *Plasma Physics*, vol. 22, no. 10-11, p. 1003, 1980.

[61] S. P. Hirshman and H. K. Meier, "Optimized Fourier representations for three-dimensional magnetic surfaces," *The Physics of Fluids*, vol. 28, no. 5, pp. 1387–1391, 1985.

[62] J. Puchmayr, M. Dunne, and E. Strumberger, "Dataset from: An intuitive form of the energy functional for resistive plasma perturbations," 2022. Zenodo. doi: 10.5281/zenodo.6901460.

[63] J. Puchmayr, M. Dunne, E. Strumberger, M. Willensdorfer, H. Zohm, F. Hindenlang, and the ASDEX Upgrade Team, "Helical mode localization and mode locking of ideal MHD instabilities in magnetically perturbed tokamak plasmas," *Nuclear Fusion*, vol. 63, no. 8, p. 086008, 2023. doi: 10.1088/1741-4326/acdd12.

[64] H. Zohm, A. Kallenbach, H. Bruhns, G. Fussmann, and O. Klüber, "Plasma angular-momentum loss by MHD mode locking," *Europhysics Letters*, vol. 11, no. 8, p. 745, 1990.

[65] S. Fietz, A. Bergmann, I. Classen, M. Maraschek, M. Garcia-Muñoz, W. Suttrop, H. Zohm, and the ASDEX Upgrade Team, "Influence of externally applied magnetic perturbations on neoclassical tearing modes at ASDEX Upgrade," *Nuclear Fusion*, vol. 55, no. 1, p. 013018, 2015.

[66] S. S. Denk, R. Fischer, H. M. Smith, P. Helander, O. Maj, E. Poli, J. Stober, U. Stroth, W. Suttrop, E. Westerhof, M. Willensdorfer, and the ASDEX Upgrade Team, "Analysis of electron cyclotron emission with extended electron cyclotron forward modeling," *Plasma Physics and Controlled Fusion*, vol. 60, no. 10, p. 105010, 2018.

[67] W. M. Tang, R. L. Dewar, and J. Manickam, "Influence of diamagnetic drifts on critical beta in tokamaks," *Nuclear Fusion*, vol. 22, no. 8, p. 1079, 1982.

[68] R. J. Hastie, P. J. Catto, and J. J. Ramos, "Effect of strong radial variation of the ion diamagnetic frequency on internal ballooning modes," *Physics of Plasmas*, vol. 7, no. 11, pp. 4561–4566, 2000.

[69] P. B. Snyder, R. J. Groebner, J. W. Hughes, T. H. Osborne, M. Beurskens, A. W. Leonard, H. R. Wilson, and X. Q. Xu, "A first-principles predictive model of the pedestal height and width: development, testing and ITER optimization with the EPED model," *Nuclear Fusion*, vol. 51, no. 10, p. 103016, 2011.

Acknowledgements

In the final pages of this thesis, I want to express my gratitude to everyone who contributed to this work.

Firstly, I would like to express my special thanks to my academic supervisor **Hartmut Zohm** for his contagious enthusiasm and the fruitful discussion about many interesting MHD topics, which motivated new ways of thinking about my research and significantly improved my understanding of MHD and plasma physics. Thank you for always taking time for me and for your great support throughout all my time at IPP.

I am also thankful to my supervisors **Erika Strumberger** and **Mike Dunne** for consistently taking time for discussions and for their unwavering support and mentorship. Thank you, Erika, for the opportunity to glean insights from your extensive knowledge on linear MHD and for the numerous valuable discussions on my findings. I am particularly thankful for the well-organized structure and thorough documentation of your code CASTOR3D, which is the base of this work. In addition, my gratitude goes to Mike for his excellent CLISTE equilibrium reconstructions, which are the base for the interpretative stability analysis and comparisons to experimental measurements. I am also very thankful for his attempts to improve the quality of my English.

Furthermore, I would like to express my gratitude to my scientific council **Elisabeth Wolfrum** for her support and thoughtful advice. I am also grateful to **Rachael McDermott**, my division head over the last months, for creating an exceptionally supportive environment that facilitated the completion of my thesis. Moreover, I want to thank **Wolfgang Suttrop** and **Matthias Willensdorfer** for the discussions on experimental findings in 3D physics and their comparison to numerical predictions. Additionally, I am grateful to Matthias for his guidance in concise academic writing. I also want to express my gratitude to **Branka Vanovac** for the opportunity to contribute to her work on the frequency of MHD instabilities.

I am very thankful to **Florian Hindenlang** for developing and providing the GVEC code. This contribution significantly enhanced the quality of the non-axisymmetric MHD equilibria studied in this work. I express my sincere gratitude to **Markus Rampp**, **Klaus Reuter**, **Thomas Hayward Schneider** and the MPCDF and TOK cluster support teams for their support in optimizing and monitoring the CASTOR3D workflow on the HPC clusters. I am especially thankful to Markus Rampp for our discussions on potential optimizations of the CASTOR3D framework. Furthermore, I am very grateful to **Carolin Nührenberg** for generously dedicating time during my visit to Greifswald to discuss my implementations to the CASTOR3D code.

I want to express my special gratitude to **Tyler Cote**, **Chris Hegna** and **Howard Wilson** for our regular meetings and discussions on linear MHD and 3D physics. Your valuable comments on my findings significantly influenced the direction of my work. I am particularly grateful to Tyler for initiating this scientific exchange.

I want to express my sincere gratitude to all those who work at IPP for the positive atmosphere. In particular, I am very thankful to all members of the **lunch and coffee groups**, Magdalena Bauer, Michael Bergmann, Tabea Gleiter, Vanessa Harnisch, Manuel Herschel, Klara Höfler, Sebastian Hörmann, Joey Kalis, Felix Klossek, David Kulla, Michaela Mayer, Raphael Schramm, Christian Schuster, Daniel Wendler and Benedikt Zimmermann, for the lively discussions, the enthusiasm for composing poems and for attending the spring roll celebrations. Thank you all a lot for the great time! I am especially grateful to **Magdalena Bauer**, **Tabea Gleiter** and **Daniel Wendler**. Thank you for your invaluable support over the last three years!

Finally, my deepest thanks go to my family, especially to my parents **Stefan** and **Sabine** and my brother **Dominic**. Thank you for always being there for me!